# THERMAL CONDUCTION IN MICROELECTRONIC CIRCUITS

by

Kenneth E. Goodson

B.S. Mechanical Engineering, B.S. Music, 1989
M.S. Mechanical Engineering, 1991
Massachusetts Institute of Technology

Submitted to the Department of Mechanical Engineering
in partial fulfillment of the requirements for the degree of

**Doctor of Philosophy in Mechanical Engineering**

at the

**MASSACHUSETTS INSTITUTE OF TECHNOLOGY**

February, 1993

© Kenneth E. Goodson, 1993. All rights reserved.

The author hereby grants to M.I.T. permission to reproduce and to
distribute publicly copies of this thesis document in whole or in part.

Signature of Author ______________________________
Department of Mechanical Engineering
January, 1993

Certified by ______________________________
Professor Markus I. Flik
Thesis Supervisor
Department of Mechanical Engineering

Accepted by ______________________________
Professor Ain A. Sonin
Chairman, Graduate Committee
Department of Mechanical Engineering

MASSACHUSETTS INSTITUTE OF TECHNOLOGY

MAR 24 1993

ARCHIVES

LIBRARIES

# THERMAL CONDUCTION IN MICROELECTRONIC CIRCUITS

by

Kenneth E. Goodson

Submitted to the Department of Mechanical Engineering
on January 28, 1993 in partial fulfillment of the requirements for the
degree of Doctor of Philosophy in Mechanical Engineering

## ABSTRACT

Dimensions smaller than 100 Å are the hallmark of highly-integrated electronic circuits containing devices such as field- and quantum-effect transistors. The performance and reliability of these circuits are influenced by thermal conduction processes with such small lengthscales. But many of these processes are not understood because (a) the thermal conductivities of thin layers in circuits are unknown, and (b) analytical and experimental tools which investigate chip-level thermal conduction processes are often not suitable for device-level processes.

This work addresses (a) for amorphous silicon-dioxide layers, showing that the thermal conductivity depends on the processing technique. Measurements yield the thermal conductivities of layers fabricated using low-pressure chemical-vapor deposition (LPCVD) and oxygen-ion implantation (SIMOX). A model accounting for porosity predicts the increase in the conductivity of the LPCVD layers due to annealing. An analysis of phonon-boundary scattering predicts the strongly-reduced conductivities of silicon-dioxide layers in cryogenic circuits.

A local temperature measurement technique and a closed-form solution to the heat-conduction equation address (b) for promising silicon-on-insulator (SOI) circuits. The predictions agree well with the data, and indicate that the reliability of transistor-interconnect contacts can be improved by optimizing the transistor dimensions. The model

predicts that phonon-boundary scattering in the source and drain of the transistor will reduce the packing limit of these devices if they are used at low temperatures, e.g., in hybrid superconductor-semiconductor circuits.

This work makes progress towards enabling device-level thermal design to become an integral part of the design of reliable high-performance circuits. An example of device-level thermal design is the choice of transistor dimensions which increase the median time to failure (MTF) of transistor-interconnect contacts.

Thesis Supervisor: Markus I. Flik
Title: Assistant Professor of Mechanical Engineering

*In memory of my grandfather,*

*Lon Raymond Goodson (1905 - 1992),*

*who solved engineering problems*

*with moral strength and a love for the day's work.*

# ACKNOWLEDGMENTS

I owe very much to my thesis adviser, Professor Markus Flik, whose influence on me far exceeded technical guidance. He encouraged me to seek and overcome apparent limitations and trust my own thinking. As one of his first students, I marvel at how quickly his enthusiastic vision molded us into a research team. I appreciate the help and friendship of my colleagues in this team, Christopher Bang, Dr. Byungin Choi, Norman Christopherson, Jeffrey Hebb, Christopher Malone, MacMurray Whale, and Dr. Zhuomin Zhang.

A collaboration with Professor Dimitri Antoniadis and Lisa Su of the Department of Electrical Engineering and Computer Science was essential for this work, in particular for the experiments, and I thank them both for their patience and feedback. I am indebted to Professor Borivoje Mikic, who has given me guidance for many years. His technical comments improved this work, especially the thermal model of SOI transistors in Chapter 6. I benefited from discussions with Professors Mildred Dresselhaus, Elias Gyftopoulos, Linn Hobbs, and Carl Thompson, and Dr. Harold Kahn. A fellowship from the Office of Naval Research paid for my graduate studies.

I will always be grateful to Laura Dahl for her unwavering affection and understanding during the past five years. She shared every setback that came with this Ph.D., and restored my perspective after intense periods of work. In my mind the degree truly belongs to us both. My family helped me as always, especially my parents. Warm fatherly advice and a continuous flow of letters from my mother kept me in touch.

I enjoy a rewarding friendship with John Wlassich, which started with our work towards the qualifying exams and grew through hiking adventures in the White Mountains. My sincere thanks go to John Oliver, Laura Dahl, and Professors Marcus Thompson and Lowell Lindgren, who encouraged me to grow and perform as a musician while at M.I.T.

## TABLE OF CONTENTS

TITLE PAGE ........................................ 1

ABSTRACT ........................................ 2

DEDICATION ........................................ 4

ACKNOWLEDGMENTS ........................................ 5

TABLE OF CONTENTS ........................................ 6

NOMENCLATURE ........................................ 10

LIST OF FIGURES ........................................ 17

LIST OF TABLES ........................................ 21

1. INTRODUCTION

1.1 Trend of Dimensions in Electronic Circuits ........................ 22

1.2 Small-Lengthscale Thermal Conduction Processes ........................ 24

1.3 Objectives ........................ 28

2. THERMAL-CONDUCTION REGIMES IN MICROELECTRONIC STRUCTURES

2.1 Introduction ........................ 29

2.2 Mechanistic Lengthscales ........................ 31

2.3 Material Properties ........................ 35

2.3.1 Metals ........................ 35

2.3.2 Dielectrics and Semiconductors ........................ 37

2.4 Regime Maps ........................ 38

2.5 Concluding Remarks ........................ 43

3. SOLID-LAYER THERMAL-CONDUCTIVITY MEASUREMENT TECHNIQUES

3.1 Introduction .................... 46

3.2 Conductivity along Layers .................... 50

3.2.1 Steady-State Techniques .................... 50

3.2.2 Transient Techniques .................... 58

3.3 Conductivity normal to Layers .................... 62

3.3.1 Steady-State Techniques .................... 62

3.3.2 Transient Techniques .................... 70

3.4 Summary and Recommendations .................... 73

4. TECHNIQUES FOR ANALYZING MICROSCALE CONDUCTION PROCESSES IN DIELECTRICS AND SEMICONDUCTORS

4.1 Introduction .................... 77

4.2 The Peierls-Boltzmann Equation .................... 77

4.2.1 Energy Conservation .................... 78

4.2.2 Relaxation-Time Approximation .................... 79

4.2.3 Local Equilibrium Distribution Function .................... 81

4.3 Solutions to the Peierls-Boltzmann Equation .................... 82

4.3.1 Second Sound .................... 84

4.3.2 The Fourier Equation, the Hyperbolic Heat Equation, and the Nonlocal Theory of Conduction .................... 84

4.3.3 Technique of Majumdar (1991) .................... 88

4.4 Summary and Recommendations .................... 89

5. PREDICTION AND MEASUREMENT OF THE THERMAL CONDUCTIVITY OF AMORPHOUS DIELECTRIC LAYERS

5.1 Introduction .................... 91

5.2 Phonon-Boundary Scattering .................... 94

5.2.1 Effective Conductivity Considering Boundary Scattering .................... 97

5.2.2 Bulk Phonon Mean Free Paths .................................... 100

5.3 Influence of the Annealing Temperature of LPCVD Layers ............ 107

5.3.1 Resistances-in-Series Model ...................................... 108

5.3.2 Model accounting for Porosity .................................... 109

5.4 Experimental Technique ................................................ 112

5.4.1 Apparatus ........................................................... 112

5.4.2 Substrate Thermal-Conduction Analysis .......................... 115

5.4.3 Uncertainty Analysis ............................................... 117

5.5 Results and Discussion ................................................ 118

5.5.1 Phonon-Boundary Scattering and $k_{n,eff}$ of SIMOX Layers ..... 118

5.5.2 Effect of Annealing Temperature on $k_{n,eff}$ of LPCVD Layers .. 124

5.6 Concluding Remarks ..................................................... 129

6. PREDICTION AND MEASUREMENT OF TEMPERATURE FIELDS IN SILICON-ON-INSULATOR ELECTRONIC CIRCUITS

6.1 Introduction ............................................................. 132

6.2 Thermal Analysis ........................................................ 134

6.2.1 Multi-Fin Model ..................................................... 134

6.2.2 Application to the Experimental Test Structure ................. 141

6.2.3 Influence of Heat-Carrier Boundary Scattering ................... 146

6.3 Channel-Temperature Measurement Technique ........................ 150

6.3.1 Apparatus and Procedure .......................................... 150

6.3.2 Temperature Distribution in the Gate ............................. 151

6.3.3 Experimental Uncertainty .......................................... 155

6.4 Results and Discussion ................................................ 155

6.4.1 Comparison of Measurements and Analysis ..................... 155

6.4.2 Influence of Heat-Carrier Boundary Scattering ................... 164

6.5 Concluding Remarks ..................................................... 169

7. CONCLUSIONS AND RECOMMENDATIONS

7.1 Circuit-Material Thermal Properties ........................................ 173

7.2 Device-Level Temperature Fields ........................................ 174

7.3 Sub-Micrometer Thermal Design of Circuits ............................ 175

REFERENCES ........................................................................ 176

## NOMENCLATURE

| | |
|---|---|
| $A$ | = area, $m^2$ |
| $a$ | = dimension of scattering site, m |
| $B$ | = boundary-scattering parameter, Eqs. (5-3) and (5-4) |
| $b$ | = characteristic length of test structure, m |
| $C$ | = specific heat at constant volume per unit volume, J $m^{-3}$ $K^{-1}$ |
| $C_s(x,T)$ | = Debye specific heat function, defined by Eq. (4-18), J $m^{-3}$ $K^{-1}$ |
| $c_p$ | = specific heat at constant pressure per unit mass, J $kg^{-1}$ $K^{-1}$ |
| $D$ | = packing limit, transistors $cm^{-2}$ |
| $d$ | = layer thickness, m |
| $d_e$ | = total thickness of thermally-grown and CVD silicon dioxide, m |
| $d_{go}$ | = thickness of silicon-dioxide layer between gate and channel, m |
| $d_{lo}$ | = thickness of silicon dioxide between fin and substrate, m |
| $d_o$ | = thickness of implanted silicon-dioxide layer, m |
| $d_{sub}$ | = substrate thickness, m |
| $d_T$ | = thickness of thermocouple bridge, m |
| $E$ | = energy deposited by laser, J |
| $E''$ | = energy deposited per unit area, J $m^{-2}$ |
| $E_e$ | = electromigration activation energy, J |
| $E_0$ | = fitting parameter for $\Lambda_{SR}$, J |
| $F_G(Y)$ | = shape function for temperature distribution in gate |
| $G$ | = thermal conductance, W $K^{-1}$ |
| $g$ | = acceleration due to gravity, m $s^{-2}$ |
| $h$ | = heat transfer coefficient, W $m^{-2}$ $K^{-1}$ |
| $h_P$ | = Planck's constant divided by $2\pi = 1.05 \times 10^{-34}$ J s |
| $I$ | = current, A |

$I_D$ = drain current, A

$I_G$ = current along gate in $Y$ direction in test structure, A

$i$ = integer in summations, Eqs. (3-11), (5-16), and (5-17)

$J$ = electrical current density, A m$^{-2}$

$\vec{J}_E$ = net energy flux vector, W m$^{-2}$

$K_e$ = electromigration constant, s A$^2$ m$^{-4}$

$K_0$ = modified Bessel function of the first kind of order zero

$k$ = thermal conductivity, W m$^{-1}$ K$^{-1}$

$k_{a,eff}$ = effective thermal conductivity along layer, defined by Eq. (3-1), W m$^{-1}$ K$^{-1}$

$k_{app}$ = apparent thermal conductivity measured by thermal comparator, W m$^{-1}$ K$^{-1}$

$k_B$ = Boltzmann constant = 1.38 x 10 $^{-23}$ J K$^{-1}$

$k_{bulk}$ = thermal conductivity measured in bulk samples, W m$^{-1}$ K$^{-1}$

$k_c$ = channel thermal conductivity, W m$^{-1}$ K$^{-1}$

$k_{n,eff}$ = effective thermal conductivity for conduction normal to layer, defined by Eq. (3-2), W m$^{-1}$ K$^{-1}$

$k_o$ = thermal conductivity of silicon dioxide, W m$^{-1}$ K$^{-1}$

$k_{sub}$ = substrate thermal conductivity, W m$^{-1}$ K$^{-1}$

$k_T$ = thermal conductivity of thermocouple bridge, W m$^{-1}$ K$^{-1}$

$L$ = length, m

$L_c$ = channel length in $X$ direction, m

$L_d$ = separation between gate and metal interconnect, m

$L_m$ = half-length of interconnect between devices in $X$ direction, m

$L_0$ = Lorenz number = 2.45 x 10$^{-8}$ W Ω K$^{-2}$

$l$ = half-width of laser line, m

MTF = median time to failure, s

$m$ = $(h / k\ d)^{1/2}$ = inverse thermal healing length of fin, m$^{-1}$

$N$ = phonon distribution function

$N_a$ = atomic number density, $m^{-3}$

$N_D$ = number density of scattering sites, $m^{-3}$

$N_{DE}$ = departure of phonon distribution function from equilibrium = $N - N_0$

$N_P$ = pore number density, $m^{-3}$

$N_0$ = equilibrium phonon distribution function

$N_{0d}$ = phonon distribution function approached due to momentum-conserving scattering

$\hat{n}$ = unit vector in direction of $\vec{q}$

$P$ = transistor power, W

$P_{ave}$ = time-averaged transistor power, W

$Q$ = heat flow, W

$q$ = argument of relative uncertainty function, $U(q)$

$\vec{q}$ = phonon wavevector, $m^{-1}$

$q_a'$ = heat-flow amplitude per unit length, W $m^{-1}$

$q''$ = heat flux, W $m^{-2}$

$q_a''$ = amplitude of periodic heat flux, W $m^{-2}$

$q_x''$ = heat flux in $x$ direction, along layer, W $m^{-2}$

$q_y''$ = heat flux in $y$ direction, normal to layer, W $m^{-2}$

$R_{app}$ = apparent thermal resistance, $m^2$ K $W^{-1}$

$R_c$ = channel-to-substrate thermal resistance, K $W^{-1}$

$R_G$ = electrical resistance of gate in $Y$ direction, $\Omega$

$R_G(T)$ = gate electrical-resistance calibration function, $\Omega$

$R_{sub}$ = substrate thermal resistance, $m^2$ K $W^{-1}$

$R_T$ = thermal resistance, $m^2$ K $W^{-1}$

$r$ = distance from heating source, m

$\vec{r}$ = position vector, m

$r_c$ = heat-flow radius, m

| | |
|---|---|
| $S$ | = parameter, Eqs. (6-14) and (6-15) |
| $S_D$ | = fitting parameter for $\Lambda_D$, m rad$^4$ s$^{-4}$ |
| $S_{SR}$ | = fitting parameter for $\Lambda_{SR}$ |
| $T$ | = temperature, K |
| $\Delta T$ | = temperature difference, K |
| $T^*$ | = $k_B\, T\, /\, E_0$ = dimensionless temperature |
| $T_a$ | = amplitude of periodic temperature, K |
| $T_B$ | = average substrate temperature below bridge A, K |
| $T_c$ | = average channel temperature, K |
| $T_G(Y)$ | = gate temperature distribution, K |
| $\Delta T'_G$ | = average temperature rise in gate, K |
| $T_i$ | = initial film temperature due to pulse heating, K |
| $T_r$ | = reference temperature, K |
| $T_0$ | = substrate or chuck temperature, K |
| $t$ | = time, s |
| $\Delta t$ | = characteristic timescale of transport process, s |
| $t_c$ | = clock period, s |
| $t_L$ | = duration of laser pulse, s |
| $U(q)$ | = relative uncertainty in parameter $q$ |
| $U_T$ | = ratio of temperature changes |
| $u$ | = energy per unit volume, J m$^{-3}$ |
| $\dot{u}_g$ | = rate of energy generation per unit volume, W m$^{-3}$ |
| $V$ | = voltage difference along bridge, V |
| $V_{DS}$ | = drain-source voltage difference, V |
| $V_G$ | = voltage difference along gate, V |
| $V_{GS}$ | = gate-source voltage difference, V |
| $V_0$ | = volume used to calculate the available phonon wavevectors, m$^3$ |

$v$ = carrier velocity, m s$^{-1}$

$\vec{v}$ = phonon velocity vector, m s$^{-1}$

$v_a$ = air velocity, m s$^{-1}$

$\vec{v}_d$ = phonon drift velocity, m s$^{-1}$

$v_s$ = average speed of sound, m s$^{-1}$

$W$ = half width of substrate, m

$W_0$ = separation between transistors in $Y$ direction, m

$w$ = width, m

$w_d$ = channel width in $Y$ direction, m

$w_e$ = separation between channel and gate contact in $Y$ direction, m

$w_m$ = width of metal interconnect in $Y$ direction, m

$X$ = coordinate in plane of substrate, m

$x$ = coordinate in plane of substrate, m

$\Delta x$ = characteristic lengthscale of transport process, m

$x_s$ = separation between bridges, m

$x_\omega$ = dimensionless phonon frequency = $h_P\omega / (k_B T)$

$Y$ = coordinate in plane of substrate, m

$y$ = coordinate normal to substrate, m

$Z$ = coordinate normal to plane of substrate, m

$Z_1, Z_2, Z_3, Z_4$ = constants, Eqs. (6-10) - (6-13), K

$\Delta z$ = uncertainty in phonon position, m

$\alpha$ = thermal diffusivity, m$^2$ s$^{-1}$

$\alpha_o$ = thermal diffusivity of implanted silicon-dioxide layer, m$^2$ s$^{-1}$

$\alpha_d$ = thermal diffusivity of source and drain of SOI FET, m$^2$ s$^{-1}$

$\alpha_{0,1}$ = phonon transmission coefficients from layer

$\beta$ = coefficient of thermal expansion, K$^{-1}$

$\Gamma$ = gamma function

$\gamma$ = Sommerfeld parameter, J $m^{-3}$ $K^{-2}$

$\delta$ = parameter, Eqs. (6-14) and (6-15)

$\varepsilon$ = emissivity

$\theta$ = Debye temperature, K

$\Lambda$ = mean free path, m

$\Lambda_e$ = electron mean free path, m

$\Lambda_{e,i}$ = electron mean free path limited by scattering on imperfections, m

$\Lambda_{e,s}$ = electron mean free path limited by scattering on phonons, m

$\Lambda_G$ = phonon mean free path limited by geometrical scattering, m

$\Lambda_s$ = phonon mean free path, m

$\Lambda_{s,b}$ = $B\, d$ = phonon mean free path limited by boundary scattering, m

$\Lambda_{s,i}$ = phonon mean free path limited by scattering on imperfections, m

$\Lambda_{s,e}$ = phonon mean free path limited by scattering on electrons, m

$\Lambda_{s,s}$ = phonon mean free path limited by scattering on phonons, m

$\Lambda_\omega$ = frequency-dependent phonon mean free path, m

$\Lambda_{\omega,bulk}$ = bulk frequency-dependent phonon mean free path, m

$\Lambda_{\omega,D}$ = frequency-dependent phonon mean free path limited by Rayleigh scattering, m

$\Lambda_{\omega,SR}$ = frequency-dependent phonon mean free path limited by scattering on structural relaxation, m

$\Lambda_0$ = frequency-independent phonon mean free path of Kittel (1949), m

$\lambda_i$ = parameter, Eqs. (5-16) and (5-17), $m^{-1}$

$\lambda_s$ = $2\pi\, v_s / \omega$ = phonon wavelength, m

$\lambda_{s,dom}$ = dominant phonon wavelength, m

$\lambda_T$ = inverse thermal diffusion length = $(\omega/\alpha)^{1/2}$, $m^{-1}$

$\mu$ = viscosity, kg $m^{-1}$ $s^{-1}$

$\rho$ = mass density, kg $m^{-3}$

| | |
|---|---|
| $\delta\rho$ | = deviation in mass density, kg $m^{-3}$ |
| $\rho_e$ | = electrical resistivity, $\Omega$ m |
| $\sigma$ | = Stefan-Boltzmann constant = 5.67 x $10^{-8}$ W $m^{-2}$ $K^{-4}$ |
| $\tau$ | = relaxation time, s |
| $\tau_d$ | = relaxation time for scattering on defects, s |
| $\tau_N$ | = relaxation time for momentum-conserving scattering, s |
| $\tau_R$ | = relaxation time for resistive scattering, s |
| $\tau_s$ | = relaxation time for scattering on phonons, s |
| $\tau_0$ | = fitting parameter for $\Lambda_{SR}$, s |
| $\Psi$ | = parameter accounting for two-dimensional conduction |
| $\omega$ | = phonon angular frequency, rad $s^{-1}$ |
| $\omega^*$ | = $\omega\,\tau_0$ = dimensionless phonon frequency |
| $\Delta\omega$ | = uncertainty in phonon frequency, rad $s^{-1}$ |
| $\omega_D$ | = Debye angular frequency, rad $s^{-1}$ |
| $d\Omega$ | = differential solid angle, sr |

## Subscripts

| | |
|---|---|
| A | = property or parameter of bridge A |
| C | = property or parameter of bridge C |
| D | = property or parameter of bridge D |
| *d* | = property or parameter of the source and drain |
| *e* | = electron property |
| *g* | = property or parameter of the gate |
| *m* | = property or parameter of the metal interconnects |
| *s* | = phonon property |

## LIST OF FIGURES


| Figure | Caption | Page |
| --- | --- | --- |
| 1-1 | Schematic of an n-type insulated-gate field-effect transistor (FET). These devices are also called metal-oxide-semiconductor (MOS) field-effect transistors, because the gate can be made from metal. For a discussion of the operation of this device, see, e.g., Tsividis (1987). | 23 |
| 1-2 | Cross section of a silicon-on-insulator (SOI) FET. The source and drain are heavily-doped n-type single-crystal silicon, the gate is heavily-doped n-type polycrystalline silicon, and the channel is lightly-doped p-type single-crystal silicon. | 26 |
| 2-1 | Thermal conduction in a thin layer. | 32 |
| 2-2 | Regime map for thermal conduction normal to copper layers. | 39 |
| 2-3 | Regime map for thermal conduction normal to silicon layers. | 40 |
| 2-4 | Regime map for thermal conduction normal to diamond layers. | 42 |
| 2-5 | Regime map for thermal conduction along epitaxial layers of the high-$T_c$ superconductor $YBa_2Cu_3O_7$. | 44 |
| 3-1 | Schematic of the layer geometry. | 48 |
| 3-2 | Test structure used to measure thermal conductivity along a bridge by Pompe and Schmidt (1975). | 52 |
| 3-3 | Self-heated bridge test structure used by Boiko et al. (1973). | 56 |
| 3-4 | Novel test structure of Graebner et al. (1992c) for measuring $k_{a,eff}$ of diamond layers. The substrate is etched from beneath the rectangular layer section shown. | 57 |

3-5 Side view of the experimental set-up of Hatta (1985) for measuring the thermal diffusivity along layers heated by a sheet of laser light. The mask was moved to change the distance $x$ while the thermocouple junction remained fixed. 60

3-6 Top view of the test structure of Goldsmid et al. (1983) for measuring $k_{n,eff}$. 63

3-7 Cross section of the test structure of Cahill et al. (1989) for measuring $k_{n,eff}$. 65

3-8 Schematic of the thermal comparator used by Lambropoulos et al. (1989). 69

4-1 Phonon energy-entropy diagram depicting Eq. (4-11). Note that this recipe for determining $T(\vec{r}, t)$ is only exact under the conditions discussed preceding Eq. (4-11). 83

5-1 Previous data for the effective thermal conductivity for conduction normal to silicon dioxide layers, $k_{n,eff}$. The acronyms in the legend indicate the fabrication techniques, whose full names are given in Table 5-1. The layers of Schafft et al. (1989) contained 4 mass percent of Phosphorus atoms. The bulk conductivity $k_{bulk}$ was measured by Sugawara (1969). 92

5-2 Two-dimensional analogs of crystalline and amorphous $Al_2O_3$ (after Zachariasen, 1932). 95

5-3 The phonon mean free path in bulk amorphous silicon dioxide, $\Lambda_{\omega,bulk}$, showing the three regimes of its frequency dependence. 105

5-4 Fraction of the conductivity due to phonons with angular frequencies less than $\omega$. 106

5-5 Cross section of test structure used here to measure $k_{n,eff}$. 113

5-6 Predictions of the thermal conductivity ratio $k_{n,eff} / k_{bulk}$ considering phonon-boundary scattering, compared with data for PECVD silicon-dioxide layers. 119

| | | |
|---|---|---|
| 5-7 | Separation by implantation with oxygen (SIMOX) fabrication process (e.g., Celler and White, 1992). | 122 |
| 5-8 | Comparison of boundary-scattering (microscale) analysis with data for SIMOX silicon-dioxide layers. | 123 |
| 5-9 | Data of the present work for $k_{n,eff}$ of LPCVD silicon dioxide layers with varying annealing temperatures. The unannealed layers are denoted by $T_p = 673$ K. | 125 |
| 5-10 | Thermal resistance data for conduction normal to the LPCVD layers. The lines are linear regressions of the data for each value of $T_p$, from which Eq. (5-10) yields $k_{int}$ and $R_B$. | 128 |
| 5-11 | Thermal conductivity internal to the LPCVD layers, $k_{int}$. Each data point is the inverse of the slope of a line in Fig. 5-10. | 130 |
| 6-1 | Physical model of a SOI FET. | 138 |
| 6-2 | Top views of: a) FET device. b) Test structure. | 144 |
| 6-3 | Mean free paths of heat carriers in SOI circuits. | 148 |
| 6-4 | Shape functions for the gate-resistor temperature distribution. Shape LB, given by Eqs. (6-19) and (6-20), yields a lower bound for $T_c$. Shape UB yields an upper bound for $T_c$. | 154 |
| 6-5 | Channel-temperature data for SOI FETs with varying device thicknesses, compared with data for a bulk (non SOI) FET. | 156 |
| 6-6 | The channel-to-substrate thermal resistance, $R_c$, as a function of the device thickness. | 158 |
| 6-7 | The channel-to-substrate thermal resistance as a function of the implanted silicon-dioxide layer thickness. | 159 |
| 6-8 | The channel-to-substrate thermal resistance as a function of the channel-interconnect separation. | 161 |
| 6-9 | Predicted dependence of the median time to failure (MTF) of FET-interconnect contacts on the channel-interconnect separation. | 163 |

| | | |
|---|---|---|
| 6-10 | Microscale and macroscale predictions of the channel-to-substrate thermal conductance. | 165 |
| 6-11 | Dependence of the channel temperature and the FET-interconnect contact temperature on the separation between FETs in the *X* direction. | 167 |
| 6-12 | Microscale and macroscale predictions of the FET separation required to achieve a targeted channel-to-substrate thermal conductance. | 168 |
| 7-1 | Research goals leading to the sub-micrometer thermal design of electronic circuits. | 172 |

## LIST OF TABLES


| Table | Caption | Page |
|---|---|---|
| 1-1 | Common dimensions of SOI FETs. The device width $w_d$ is in the direction normal to the $X$-$Z$ plane in Fig. 1-2. | 27 |
| 3-1 | Summary of techniques measuring the effective thermal conductivity along layers. | 74 |
| 3-2 | Summary of techniques measuring the effective thermal conductivity normal to layers. | 75 |
| 4-1 | Summary of the validity of techniques for analyzing microscale phonon conduction processes. | 90 |
| 5-1 | Summary of the data in Fig. 5-1. The relative uncertainty in the measurement of $k_{n,eff}$ is $U(k_{n,eff})$. The measurement techniques are reviewed on the indicated pages in Section 3.3.1. | 93 |
| 5-2 | Values of $k_{int}$ and $R_B$ extracted from the data for each value of the highest processing temperature, $T_p$. | 127 |
| 6-1 | Thermal conductivities of SOI circuit materials. These values were measured in bulk samples, although many of the components in the FETs are thin layers. The basis for the use of these values is given in Section 6.2.2. | 134 |
| 6-2 | Test-structure dimensions. The dimensions given in ranges varied among the test structures. | 143 |
| 6-3 | Thermal conductivities used to determine the effect of boundary scattering. These were recommended by Touloukian et al. (1970a; 1970b) | 149 |
| 6-4 | Effect of boundary scattering on the FET packing limit. | 169 |

# 1. INTRODUCTION

Modern fabrication techniques make electronic structures with features smaller than 100 Å. These structures are the basis of field- and quantum-effect transistors and make possible microprocessors in computers. The performance and reliability of these devices depend on the temperature fields within the electronic microstructures, and are influenced by thermal conduction processes with small lengthscales, e.g., less than a micrometer. But in many cases the thermal conductivities of the layers in these structures are not known. The available analytical and experimental tools which determine temperature fields are often inappropriate due to the small dimensions of the structures. These problems are becoming more important as the dimensions in electronic circuits decrease.

## 1.1 Trend of Dimensions in Electronic Circuits

The basic element of most digital electronic circuits is the field-effect transistor (FET), shown in Fig. 1-1. An important lateral dimension of this device is the channel length $L_c$, which at present is near 0.7 μm. The lateral dimensions of FETs have decreased steadily since 1960, by about an order of magnitude every 15 years (e.g., Sze, 1988). Reducing the lateral dimensions of FETs, in particular the channel length, helps to decrease their switching time. This facilitates higher clock frequencies and faster computing. Reducing the lateral dimensions of FETs also decreases the substrate area occupied by each transistor, yielding chips which have more transistors and more functions. Guidelines for

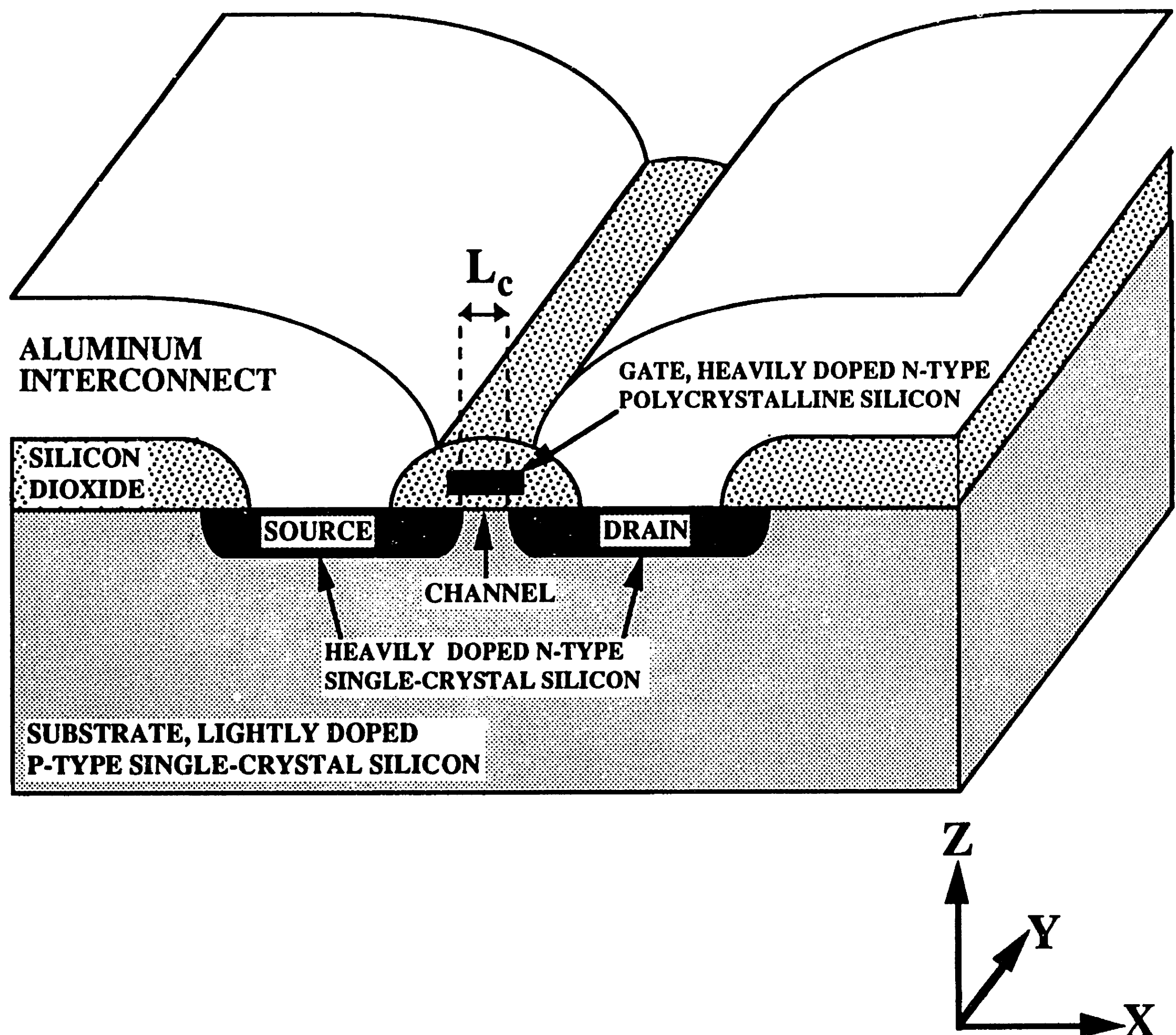


Fig. 1-1 Schematic of an n-type insulated-gate field-effect transistor (FET). These devices are also called metal-oxide-semiconductor (MOS) field-effect transistors, because the gate can be made from metal. For a discussion of the operation of this device see, e.g., Tsividis (1987).

reducing FET dimensions and the problems this can yield in electrical behavior were discussed by Antoniadis (1987), Tsividis (1987), and Yang (1988).

The trend of FET packing densities has increased the power dissipated in electronic chips, providing strong motivation for the research community to address heat transfer problems in electronic systems (e.g., Aung, 1991; Bar-Cohen and Kraus, 1988, 1990). Much of this work aimed to improve the *reliability* of these systems, both by designing them to withstand the stresses caused by thermal expansion, and by helping to prevent high operating temperatures as the power dissipated per unit substrate area increased. High operating temperatures increase the rate of atomic diffusion within the circuit, which can result in its failure or non-optimal performance. An important example of this is electromigration, the flow of atoms along a metal interconnect due to a bias current, which causes interconnects and FET-interconnect contacts to fail (e.g., Murarka, 1988). The atomic flux due to electromigration is proportional to the electric field. The electrical *performance* of circuits can also benefit from lower operating temperatures, e.g., for transistors with moderately small channel lengths the time required to switch increases with increasing temperature (e.g., Tsividis, 1987). This results from the higher energy density of the lattice in the channel region, which more strongly scatters the electrons and reduces their electrical mobility, the ratio of the electron drift velocity to the electric field.

## 1.2 Small-Lengthscale Thermal Conduction Processes

In addition to motivating the research discussed in Section 1.1, the trend of FET dimensions is having an impact on the lengthscales of heat-transfer processes which are important in electronic systems. As the dimensions of transistors decrease, a greater fraction of the transistor-to-coolant temperature drop can take place within a few micrometers of the transistor hotspots. The resulting *small-lengthscale* thermal-conduction problems do not necessarily yield to techniques that are successful in the rest of the electronic system, e.g., infrared thermography and the use of bulk values of the thermal

conductivity in the Fourier equation. But small-lengthscale thermal conduction processes can influence the temperatures of the FET channel and the FET-interconnect contacts, which affect the circuit performance and reliability, and should be considered during circuit design. These processes also govern the temperature gradients at the substrate surface, which are important because they facilitate interconnect failure due to electromigration (e.g., Schwarzenberger, 1988).

Small-lengthscale thermal conduction processes are especially important in novel silicon-on-insulator (SOI) circuits. Transistors in conventional "bulk" circuits are fabricated at the surface of a bulk wafer, and are in direct electrical and thermal contact with the substrate, as shown in Fig. 1-1. In contrast, SOI transistors are electrically insulated from the substrate by a silicon-dioxide layer. Figure 1-2 is a cross section of a SOI FET, whose common dimensions are given in Table 1-1. The silicon-dioxide layer between the device and the substrate is fabricated by implanting oxygen ions into single-crystal silicon. The implanted layer electrically isolates neighboring devices, preventing latchup and current leakage to the substrate, and reduces the contribution of the substrate to the device electrical capacitance, facilitating faster circuits (Colinge, 1991). But the implanted layer possesses a low thermal conductivity and inhibits conduction cooling of the devices. The implanted layer dominates the small-lengthscale thermal conduction processes in SOI circuits.

Small-lengthscale thermal conduction processes are often not understood due to two problems: (a) The thermal conductivities of layers in circuits, such as the implanted silicon-dioxide layer in Fig. 1-2, are not known. The use of values of the thermal conductivity measured in bulk samples can yield significant error because the microstructure and purity of a layer, which influence thermal conduction, often depend on its thickness and fabrication technique. The small dimensions of the layer can also make interfacial effects important, such as thermal boundary resistances. An important interfacial effect is the boundary scattering of the carriers of thermal energy, electrons in metals and

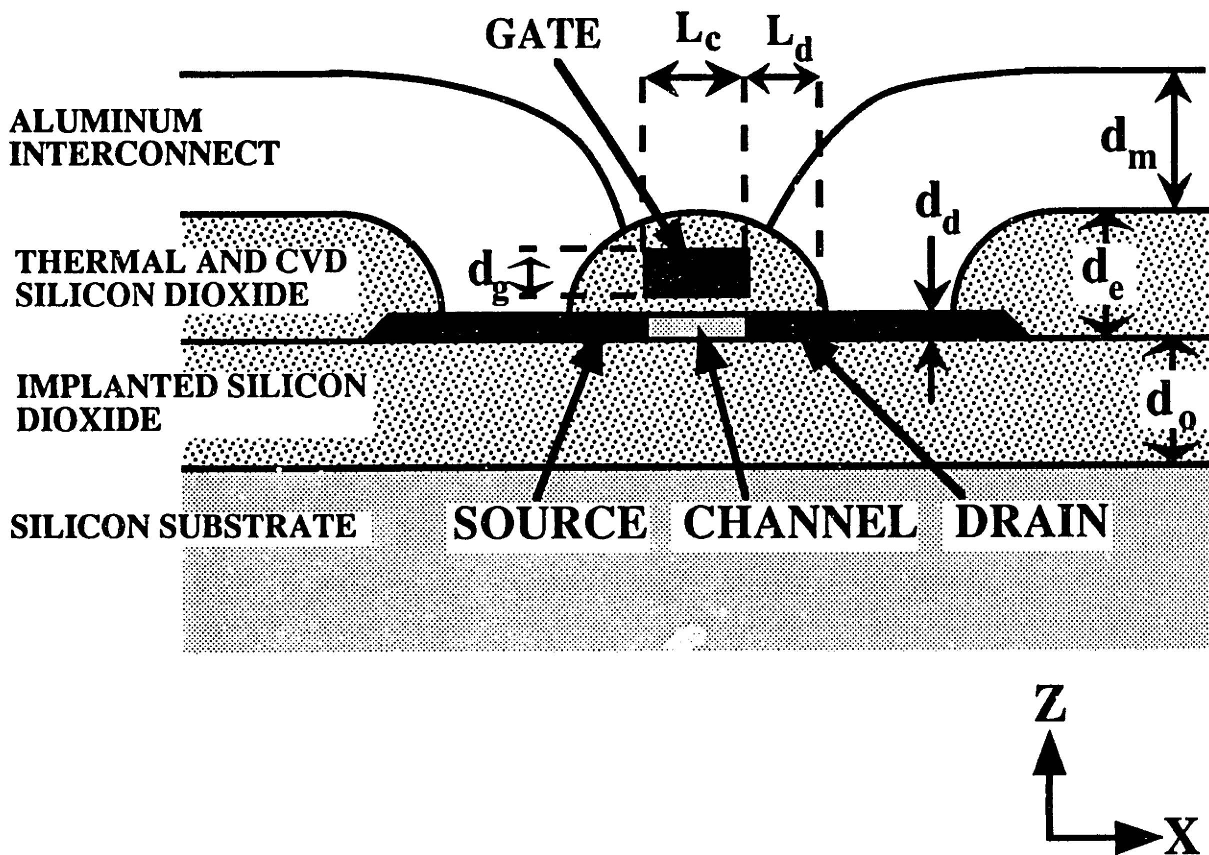


Fig. 1-2 Cross section of a silicon-on-insulator (SOI) FET. The source and drain are heavily-doped n-type single-crystal silicon, the gate is heavily-doped n-type polycrystalline silicon, and the channel is lightly-doped p-type single-crystal silicon.

Table 1-1 Common dimensions of SOI FETs. The device width $w_d$ is in the direction normal to the $X$-$Z$ plane in Fig. 1-2.

| Dimension | Symbol | Value (μm) |
|---|---|---|
| Implanted-$SiO_2$ Thickness | $d_o$ | 0.4 |
| Additional-$SiO_2$ Thickness | $d_e$ | 0.6 |
| Interconnect Thickness | $d_m$ | 0.5 |
| Device Thickness | $d_d$ | 0.08 |
| Gate Thickness | $d_g$ | 0.3 |
| Gate-Channel Separation | $d_{go}$ | 0.0055 |
| Channel-Interconnect Separation | $L_d$ | 0.5 |
| Channel Length | $L_c$ | 0.5 |
| Device Width in $Y$ direction | $w_d$ | 0.8 |

phonons, the quanta of lattice waves, in dielectrics and semiconductors. Boundary scattering becomes more important as the ratio of the layer thickness to the carrier mean free path decreases, and can cause the effective thermal conductivity of the layer to be significantly lower than the conductivity of a bulk material with the same microstructure. Chapter 6 predicts that boundary scattering will have a strong effect on thermal conduction in the source and drain of SOI FETs when they are operated at or below 77 K.

(b) The available analytical tools and temperature-measurement techniques are often not appropriate for determining device-level temperature fields. Finite-element conduction analysis cannot at present account for heat-carrier boundary scattering, and this may yield large errors, particularly at low temperatures where the heat-carrier mean free path can be much larger than the dimensions of electronic microstructures. Most temperature-measurement techniques have insufficient spatial resolution to probe device-level temperature fields, e.g., infrared thermography works above the diffraction limit,

which is of the order of 10 μm at 300 K. But a much finer resolution is needed to investigate the temperature of the channel hotspot of the SOI FET in Fig. 1-2.

## 1.3 Objectives

A major difficulty with working on small-lengthscale thermal-conduction problems is that there is uncertainty about which experimental and analytical tools are applicable to a given process. The next three chapters address this difficulty, without providing new physics information. Chapter 2 defines the *microscale thermal-conduction regime*, in which the use of the Fourier equation for the heat flux yields significant error, and plots regime maps for electronic materials. Chapter 3 reviews the existing techniques for measuring the thermal conductivity in the directions along and normal to thin layers, and points out the need for standard techniques with well-known uncertainties. Chapter 4 reviews techniques which analyze microscale thermal conduction processes in dielectrics and semiconductors.

Chapters 5 and 6 directly address the problems (a) and (b) discussed in Section 1.2. Chapter 5 provides a technique for measuring the thermal conductivity in the direction normal to amorphous dielectric layers, and investigates the influence of the fabrication process on this property. This yields the first data for the conductivity of the implanted silicon-dioxide layers in SOI circuits, and for the annealing-temperature dependence of the conductivity of low-pressure chemical-vapor deposited (LPCVD) layers. The data are compared with predictions of analyses accounting for phonon-boundary scattering and porosity. Chapter 6 uses the thermal-conductivity data for the implanted layers to predict the temperature fields in SOI circuits, and develops a technique to measure the channel temperature. An approximate analysis of boundary scattering in the source and drain of SOI FETs estimates the impact of microscale conduction on the FET thermal packing limit. Chapter 7 proposes a research program which is motivated by this work.

# 2. THERMAL-CONDUCTION REGIMES IN MICROELECTRONIC STRUCTURES

## 2.1 Introduction

Due to the small dimensions of microelectronic structures, it is often not known if the thermal conduction processes in these structures can be analyzed with *macroscale* theories, i.e., methods which do not consider the influence of the boundaries of the structure on the thermal conductivity within the structure. If macroscale theory is applied to a microstructure in a situation for which it is inappropriate, then a significant error in the calculated heat transfer rate or temperature distribution can result. Such an error can cause the device to be designed to perform in a sub-optimal manner or prevent it from being able to function. In electronic devices, microscale effects in a thin layer can inhibit the flow of heat from hotspots within the layer, resulting in peaks of temperature of a magnitude greater than those predicted by macroscale analysis. These temperature peaks can affect the performance and reliability of the devices and interconnects in the circuit. Circuit designers can benefit from a criterion which shows whether macroscale theory can be applied to a given device or whether *microscale* theory must be used. Microscale theory determines the effect of the structure dimensions on a transport property by considering the physical mechanism of transport, i.e., thermal conduction by electrons in metals and phonons, the quanta of lattice waves, in dielectrics and semiconductors.

Fundamentals and applications were presented for microscale thermal conduction by Ziman (1960) and Tien et al. (1969). Recently, microscale heat transfer phenomena have received intensive interest due to the emergence of thermal microsensors (Udell, 1990) and high-$T_c$ superconducting layers (Flik and Tien, 1990; Goodson and Flik, 1992). None of these studies presented the boundary of the macroscale heat-transfer regime for a given transport mechanism in terms of the parameters available to the circuit designer, i.e., the dimensions of the microelectronic structure and the operating temperature. Hence, based on these works it is not immediately possible to decide if macroscale theory is applicable to a given conduction process.

This chapter develops heat transfer *regime maps* for microstructures which relate a geometric lengthscale to temperature. The boundary between the microscale and macroscale regimes is determined as a function of temperature by the requirement that the application of macroscale theory yields an error not exceeding 5 percent. Through the mechanistic lengthscale governing the transport process, this functional relation depends on the material properties, i.e., the scattering mechanisms for electron and phonon thermal conduction in solids. The geometric lengthscale is the smallest structure dimension. Previous regime maps delineating boundaries between applicable theories of transport phenomena were published for rarefied gas dynamics by Tsien (1946) and for thermal radiation in packed beds by Tien (1988). Majumdar (1991) illustrated the analogy between microscale conduction in dielectrics and radiative transfer, and presented a regime map for diamond layers similar to the one developed in this chapter. Recently, Tien and Chen (1992) observed that there are two microscale thermal-conduction regimes. The first includes conduction processes for which the *mean free path* of heat carriers is comparable to or larger than the geometric lengthscale. The second microscale regime is a subset of the first, and includes processes where the *wavelength* of the heat carriers is comparable to or larger than the geometric lengthscale. This chapter investigates the boundary between the first microscale regime and the macroscale regime.

The impact of the regime maps is twofold. First, specific devices can be represented with a region in a regime map, showing immediately whether or not a certain transport process in a given device can be analyzed with macroscale theory. Second, demands for future research in microscale heat transfer can be anticipated by marking regions in the regime maps which correspond to the expected development of a given microtechnology. This work does not present new physics information. It relies on known physical foundations of transport phenomena. But this knowledge has not been applied to date in thermal analysis and design. By providing regime maps, this work attempts to aid in the development of tools for microscale thermal analysis and experimentation.

## 2.2 Mechanistic Lengthscales

In solids, heat is carried by electrons and lattice waves, whose quanta are phonons. In pure metals, the electron contribution dominates. In dielectrics and semiconductors, the phonon contribution dominates. Kinetic theory yields the thermal conductivity of metals, dielectrics, and semiconductors (Ziman, 1960),

$$k = \frac{1}{3} C \, v \, \Lambda \tag{2-1}$$

For metals, $C = C_e$ is the electron specific heat, $v = v_e$ is the electron Fermi velocity (Kittel, 1986), and $\Lambda = \Lambda_e$ is the electron mean free path. For conduction in dielectrics and semiconductors, $C = C_s$ is the phonon specific heat, $v = v_s$ is the speed of sound, and $\Lambda = \Lambda_s$ is the phonon mean free path. The specific heat $C$ in Eq. (2-1) is only that portion of the total specific heat of the material which is brought about by the carrier being analyzed.

Figure 2-1 illustrates that for a thin layer, the importance of boundary scattering relative to internal scattering increases with the ratio $\Lambda / d$, where $\Lambda$ is the bulk value of the

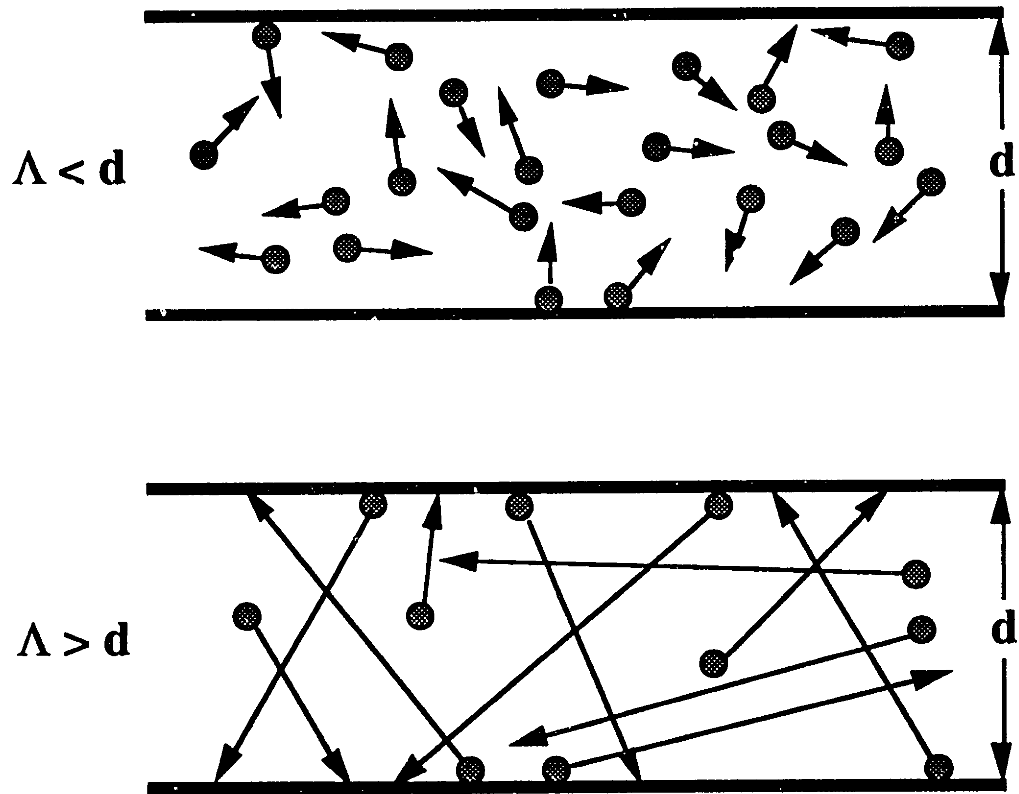


Fig. 2-1 Thermal conduction in a thin layer.

mean free path of the dominant carriers of heat, and $d$ is the layer thickness. Scattering on the boundaries of the layer reduces the carrier mean free path from its bulk value, reducing the thermal conductivity according to Eq. (2-1). For $\Lambda \ll d$, this reduction may be neglected. But for $\Lambda \sim d$ and $\Lambda > d$, the influence of boundary scattering must be considered, and the effective thermal conductivity even in an isotropic layer depends on the direction of energy flow. In what follows, the effective thermal conductivity along the layer is the absolute value of the ratio of the heat flux to the temperature gradient along the layer. The effective thermal conductivity normal to the layer is the product of the heat flux normal to the layer and the layer thickness divided by the temperature difference between the top and bottom surfaces of the layer.

Fuchs (1938) and Sondheimer (1952) determined the influence of electron-boundary scattering on the effective electrical conductivity along thin metal layers by solving the Boltzmann equation. Tien et al. (1969) and Kumar and Vradis (1991) showed that this result may be used with little error up to room temperature to determine the effective thermal conductivity along thin metal layers. Majumdar (1991) developed the equation of phonon radiative transfer from the Boltzmann equation to analyze microscale phonon conduction in dielectrics. This equation considers the variation of the phonon free paths about the mean free path and the dependence of the phonon mean free path on the phonon frequency. Chen and Tien (1992) solved the equation of phonon radiative transfer considering the transmission of carriers through the layer boundaries to determine the effective thermal conductivity normal to and along GaAs layers in a GaAs-AlGaAs multilayered structure.

Flik and Tien (1990), by assuming that all carrier free paths are equal to the mean free path in the absence of boundary scattering, obtained approximate closed-form solutions for the effective electron or phonon conductivity along or normal to a layer. The result for conduction along a layer agrees within 20 percent with that of Fuchs (1938) and Sondheimer (1952). For $d > \Lambda$, the analysis of Flik and Tien (1990) yielded

$k_{n,eff} / k_{bulk} = 1 - \Lambda/(3d)$ for the effective conductivity normal to the layer, and

$k_{a,eff} / k_{bulk} = 1 - 2\Lambda/(3\pi d)$ for the effective conductivity along the layer, where $k_{bulk}$ and $\Lambda$ are the isotropic bulk values of the conductivity and the mean free path. The use of the bulk value of $k_{bulk}$ rather than the effective conductivity in an error greater than 5 percent for $d < 7\ \Lambda$ for conduction normal to the layer, and for $d < 4.5\ \Lambda$ for conduction along the layer. These inequalities determine the microscale regimes in the present analysis.

These criteria determine whether microscale effects increase the volume resistance of the layer. They do not consider the thermal boundary resistance, which can cause the effective conductivity normal to multilayered structures to vary with the layer thicknesses. If the temperature difference across the interface is small and the temperature is below about 30 K, the thermal boundary resistance at a dielectric-dielectric or metal-dielectric interface is governed by the acoustic mismatch between the materials and is inversely proportional to the third power of the lower temperature (Swartz and Pohl, 1989). At temperatures above 100 K, the boundary resistance is between $10^{-7}$ and $10^{-8}$ $m^2\ K\ W^{-1}$. The partial transmission of carriers through the boundaries, which is limited by the boundary resistance, is not considered in the present analysis. Partial transmission increases the free path of some carriers, and can reduce the dimension separating the microscale and macroscale regimes for conduction normal to a layer. Chen and Tien (1992) predicted that if carrier transmission through the boundaries is diffuse, the effective phonon conductivity along a dielectric layer does not depend on the phonon transmission coefficients at the boundaries.

The hyberbolic thermal-conduction equation considers the finite propagation speed of energy and was proposed for use when the duration of a thermal disturbance is very small (Joseph and Preziosi, 1989; 1990), i.e., in a temporal microscale situation. For conduction in the absence of a heat source, the hyperbolic conduction equation is

$$\frac{\tau}{\alpha}\frac{\partial^2 T}{\partial t^2} + \frac{1}{\alpha}\frac{\partial T}{\partial t} = \nabla^2 T \qquad (2\text{-}2)$$

where $\alpha$ is the thermal diffusivity and $\tau$ is the relaxation time. The relaxation time $\tau = \Lambda / v$ is the average time a carrier travels between collisions. Majumdar (1991) showed that Eq. (2-2) can be derived from the Boltzmann equation for dielectric layers only if the layer thickness is much larger than the phonon mean free path. Equation (2-2) reduces to the macroscale thermal-conduction equation if the second term on the left is much larger than the first term. Order-of-magnitude analysis yields the criterion $(\tau/\alpha)(\Delta T/\Delta t^2) << (1/\alpha)(\Delta T/\Delta t)$ for the macroscale regime, where $\Delta t$ is the characteristic time scale of the heat transfer process and $\Delta T$ is the characteristic temperature difference. If for a thin layer of thickness $d$ the characteristic time scale $\Delta t$ is given by diffusion across the layer, then it satisfies $d \sim (\alpha\Delta t)^{1/2}$, and the macroscale criterion is $d^2 >> \alpha\,\tau$. Using Eq. (2-1), the thermal diffusivity is $\alpha = k/C \sim v\Lambda$. Since $\tau = \Lambda/v$, the final criterion for macroscale conduction is $d^2 >> \Lambda^2$. If no timescales shorter than $d^2/\alpha$ are present, then the Fourier equation is valid for conduction across a thin layer as long as boundary scattering is not important. For shorter timescales, or if $d$ is of the order of or smaller than $\Lambda$, the Fourier equation is not valid. Vedavarz et al. (1991) prepared a regime map for hyperbolic heat conduction, but their use of Eq. (2-2) in the limit of $d^2 \sim \Lambda^2$ needs to be reexamined.

## 2.3 Material Properties

### 2.3.1 Metals

The theory of thermal conduction in metals was summarized by Wilson (1953) and Ziman (1960). The electron mean free path may be obtained from experimental values of the thermal conductivity using Eq. (2-1), the electron specific heat, $C_e$, and the Fermi velocity, $v_e$. The thermal conductivity of metals was given by Touloukian et al. (1970a).

The Fermi velocities of electrons in metals are of the order of $10^6$ m s$^{-1}$ and were tabulated by Kittel (1986). The volumetric specific heat of electrons, $C_e$, is proportional to temperature,

$$C_e = \gamma T \tag{2-3}$$

The Sommerfeld parameter, $\gamma$, was tabulated for metals by Kittel (1986) and is of the order of 100 J m$^{-3}$ K$^{-2}$.

The mean free path of electrons in metals is limited by scattering on imperfections and phonons. Imperfections include impurity atoms and lattice defects. Matthiessen's rule separates the inverse electron mean free path, $1/\Lambda_e$, into components due to imperfection scattering, $1/\Lambda_{e,i}$, and phonon scattering, $1/\Lambda_{e,s}$,

$$\frac{1}{\Lambda_e} = \frac{1}{\Lambda_{e,i}} + \frac{1}{\Lambda_{e,s}} \tag{2-4}$$

The imperfection-limited mean free path $\Lambda_{e,i}$ is independent of temperature, while the phonon-limited mean free path $\Lambda_{e,s}$ decreases with increasing temperature. At very low temperatures, $T << \theta$, the absence of phonon scattering allows $\Lambda_{e,i}$ to be determined. The Debye temperatures $\theta$ of monatomic solids were given by Kittel (1986).

The scattering of electrons on phonons dominates over the scattering of electrons on imperfections above a temperature near 50 K. When phonon scattering dominates, $\Lambda_{e,s}$ can be calculated from thermal conductivity data using Eq. (2-1). The value of $\Lambda_{e,s}$ may be extrapolated to lower temperatures using the formula of Wilson (1953) for electron thermal conduction limited by scattering on phonons. At temperatures below a low reference temperature, $T < T_r < \theta / 10$, this formula may be simplified with less than 10 percent error in metals to $k_{e,s}(T)/k_{e,s}(T_r) = (T_r/T)^2$. Using this result and Eqs. (2-1) and (2-3) yields the mean free path for $T < T_r$,

$$\frac{\Lambda_{e,s}(T)}{\Lambda_{e,s}(T_r)} = \left(\frac{T_r}{T}\right)^3 , \qquad T_r < \theta / 10 \tag{2-5}$$

### 2.3.2 Dielectrics and Semiconductors

Phonon conduction in dielectrics was reviewed by Ziman (1960). The phonon mean free path in dielectrics is calculated from experimental conductivity data using Eq. (2-1), the phonon specific heat, $C_s$, and the average speed of sound in the material, $v_s$. The specific heats of dielectrics and semiconductors were given by Touloukian and Buyco (1970a; 1970b). Phonon conduction in dielectrics is limited by scattering on other phonons and on imperfections, which include lattice defects and isotopes. In doped semiconductors, the free carriers also scatter phonons. Matthiessen's rule yields

$$\frac{1}{\Lambda_s} = \frac{1}{\Lambda_{s,i}} + \frac{1}{\Lambda_{s,s}} + \frac{1}{\Lambda_{s,e}} \tag{2-6}$$

where $\Lambda_s$ is the phonon mean free path, $\Lambda_{s,i}$ is the phonon mean free path limited by scattering on imperfections, $\Lambda_{s,s}$ is the phonon mean free path limited by scattering on phonons, and $\Lambda_{s,e}$ is the phonon mean free path limited by scattering on free carriers in semiconductors. The third term on the right of Eq. (2-6) is zero for dielectrics.

Below a reference temperature, $T < T_r << \theta$, the phonon mean free path limited by scattering on phonons is approximately

$$\frac{\Lambda_{s,s}(T)}{\Lambda_{s,s}(T_r)} = \exp\left[\frac{\theta}{2}\left(\frac{1}{T} - \frac{1}{T_r}\right)\right] \tag{2-7}$$

At low temperatures, the phonon mean free path in undoped crystals is limited by scattering on isotopes and point imperfections. When this mechanism is dominant and $T < T_r << \theta$, the phonon mean free path is well approximated by (Berman et al., 1956)

$$\frac{\Lambda_s(T)}{\Lambda_s(T_r)} = \left(\frac{T_r}{T}\right)^4 \tag{2-8}$$

### 2.4 Regime Maps

Figure 2-2 shows the regimes for thermal conduction in annealed, polycrystalline copper. The mean free path below 30 K is given by Eq. (2-5). Above 30 K, $\Lambda_{e,s}$ is obtained using Eqs. (2-1) and (2-3) and values of the thermal conductivity recommended by Touloukian et al. (1970a). Below 30 K, $\Lambda_{e,s}$ is obtained using Eq. (2-5) with $T_r = 30$ K. Based on Eqs. (2-1) and (2-2) and low-temperature thermal conductivity data from the following sources, the imperfection-limited mean free path for copper at least 99.999 percent pure by weight is $\Lambda_{e,i} = 57$ μm (White and Tainsh, 1960), for copper containing 0.0013 percent oxygen is $\Lambda_{e,i} = 3.2$ μm (Powell et al., 1957), and for copper containing 0.056 percent iron is $\Lambda_{e,i} = 0.096$ μm (White and Woods, 1954). Below 30 K, the layer thickness denoting the microscale regime boundary varies by three orders of magnitude depending on the purity. In cryogenic electronics applications, the effective thermal conductivity of layers thinner than 1 μm is size-dependent, while at room temperature layers of thickness greater than about 0.1 μm belong to the macroscale regime.

Figure 2-3 is a regime map for thermal conduction normal to silicon layers. The average speed of sound is $v_s = 6500$ m s$^{-1}$ (McSkimin, 1953) and the values of the pure crystalline thermal conductivity are those recommended by Touloukian et al. (1970a). The mean free path is extrapolated to low temperatures for an infinite crystal using Eq. (2-8) with $T_r = 25$ K. The data of Rosenberg (1954) are employed for the thermal conductivity of polycrystalline silicon below 100 K. The dashed curve in the left of Fig. 2-3 indicates that the mean free paths for the crystal and polycrystal must approach one another with increasing temperature and is not supported by experimental data. Slack (1964) gave the thermal conductivity of a boron-doped silicon crystal from which the dashed curve on the right of Fig. 2-3 is extrapolated. The dimension bounding the

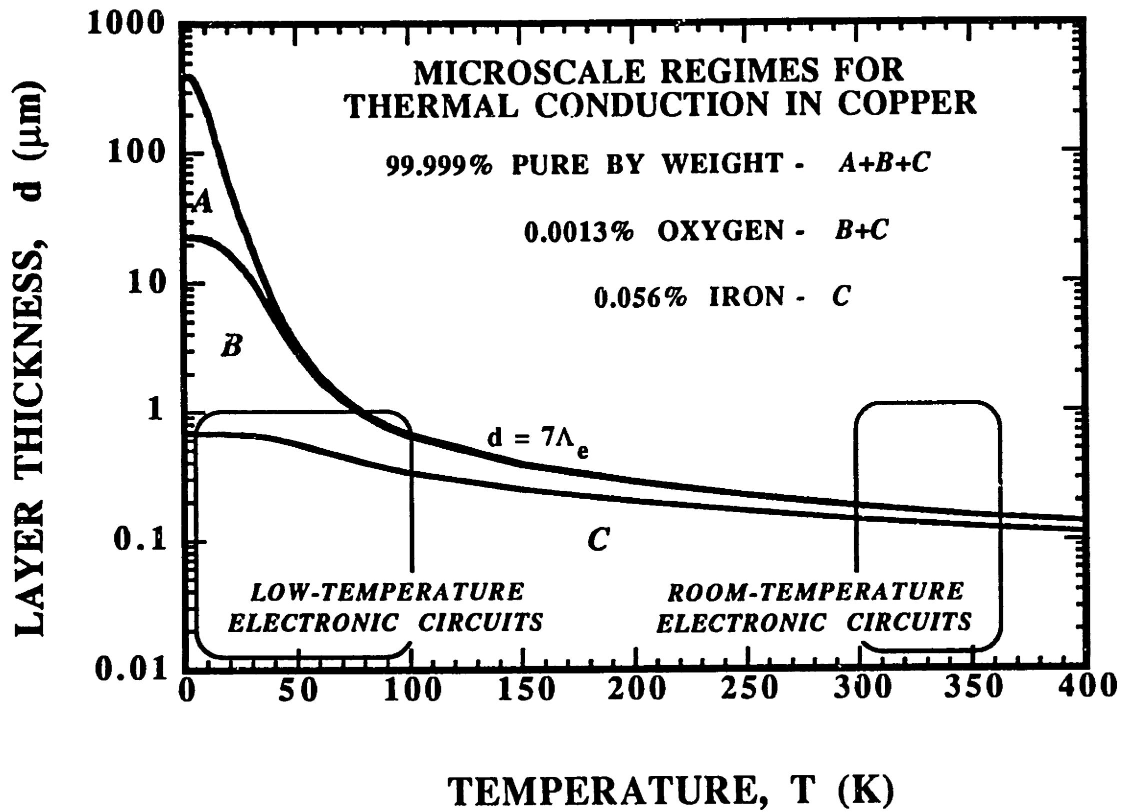


Fig. 2-2 Regime map for thermal conduction normal to copper layers.

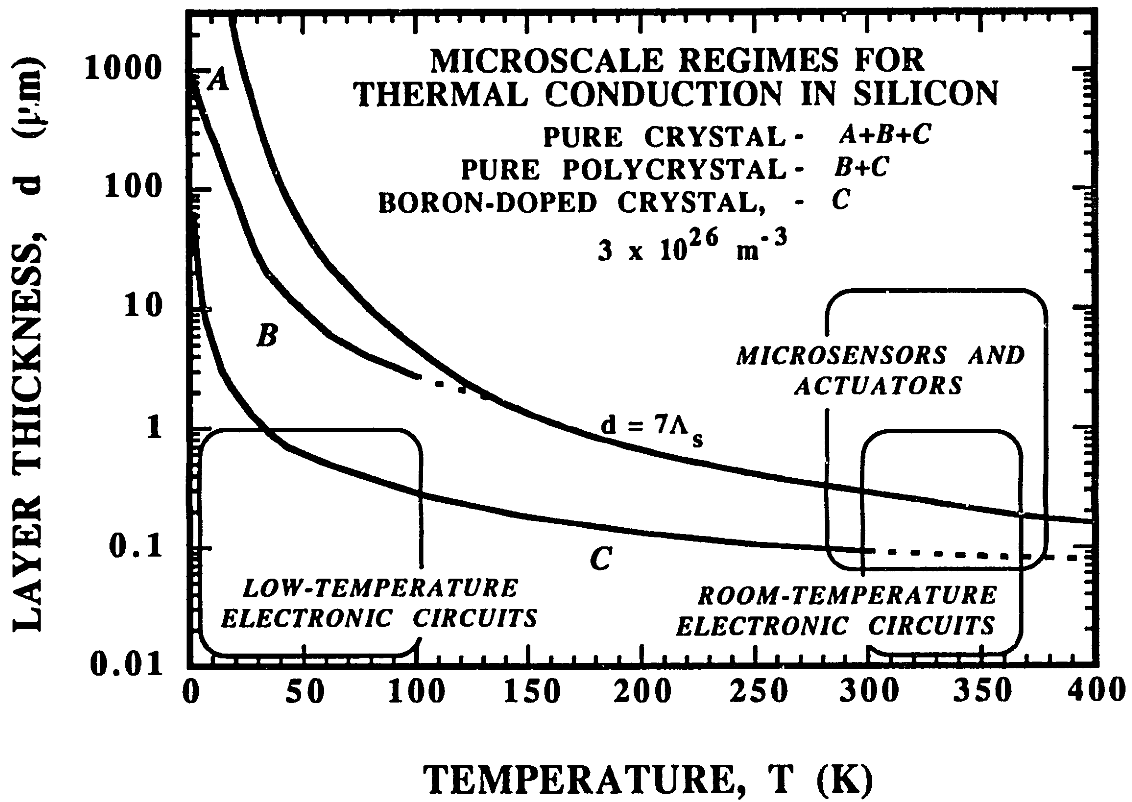


Fig. 2-3 Regime map for thermal conduction normal to silicon layers.

microscale regime is highly dependent on the carrier concentration. At low temperatures, it is reduced by the grain-boundary scattering in a polycrystalline specimen. Silicon microstructures used in the majority of room-temperature sensors and actuators do not exhibit a size-dependent thermal conductivity, in contrast to layers in low-temperature electronic circuits. The doping level determines whether a silicon layer is in the microscale conduction regime at room temperature.

Regimes for conduction normal to type IIa diamond layers are shown in Fig. 2-4. The thermal conductivity was given by Berman et al. (1956) and the average speed of sound, $v_s = 13500$ m s$^{-1}$, by McSkimin and Andreatch (1972). Equation (2-8) determines the imperfection-limited mean free path at temperatures where boundary scattering was important. The reference temperature is $T_r = 100$ K, which satisfies $T_r \ll \theta$ because the Debye temperature of diamond is $\theta = 1880$ K. Although the primary constituent of diamond is the $^{12}C$ atom, naturally occurring diamond contains 1.1 percent of the isotope $^{13}C$. At low temperatures, scattering on this isotope limits the thermal conductivity of natural diamond. Majumdar (1991) presented an algorithm to determine the regime boundary for diamond as a function of the fraction of $^{13}C$. In Fig. 2-4, the regime boundary for diamond with a $^{13}C$ content of 1.1 percent calculated using his algorithm agrees well with the regime boundary of the present analysis.

Anthony et al. (1990) achieved a $^{13}C$ content of 0.07 percent in a synthetic diamond crystal and showed that its thermal conductivity at room temperature was 50 percent greater than that measured previously for diamond. Based on this result, the mean free path of a hypothetical crystal containing no isotopes or lattice defects is estimated using Eq. (2-7) with $T_r = 300$ K. The microscale regime for this case is shown in Fig. 2-4 and indicates the largest value of $d$ for a given temperature at which microscale conduction may ever occur in diamond. It is not possible to achieve in thin diamond layers in electronic circuits the same high thermal conductivities measured in bulk crystals. Because of the low coefficient of friction between diamond surfaces, diamond layers possess great

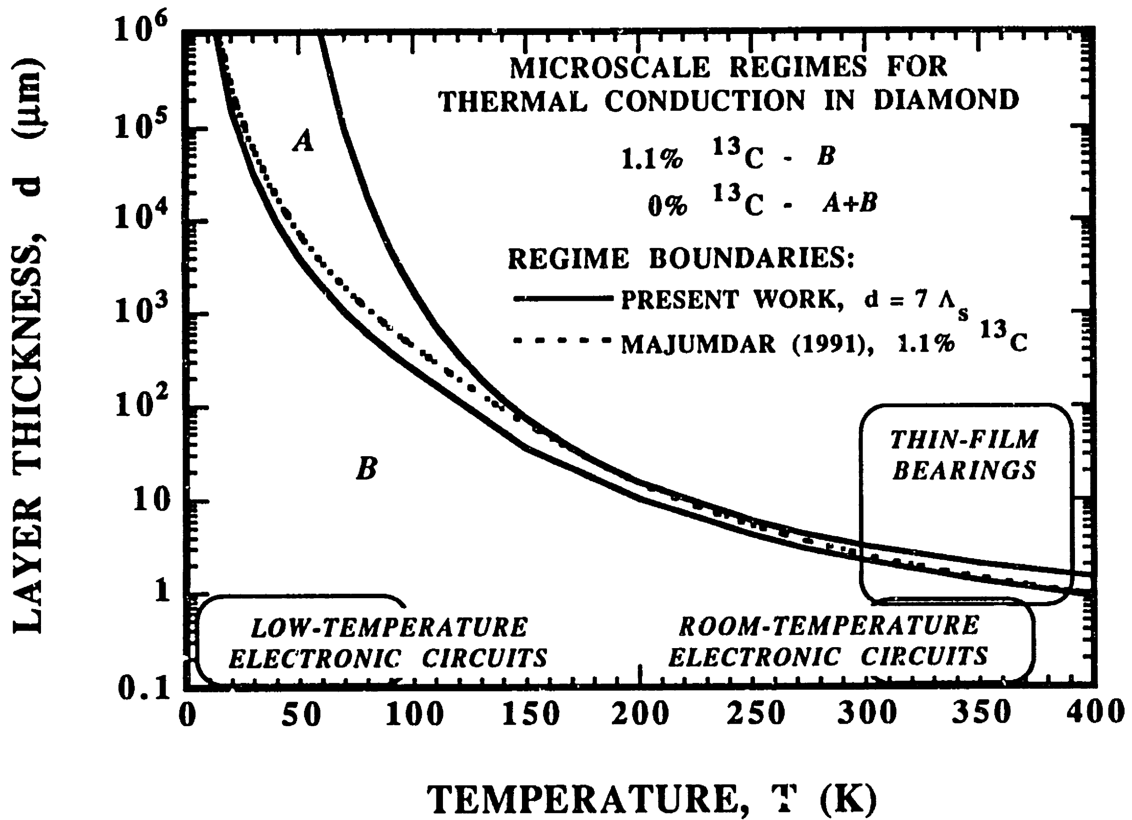


Fig. 2-4 Regime map for thermal conduction normal to diamond layers.

potential for application as bearing materials (Guyer and Koshland, 1990). Figure 2-4 shows that for room-temperature applications, the thermal conductivity of bearing layers thinner than 3 μm is size dependent. This fact can strongly affect the temperature fields existing in such bearings due to dissipation.

Figure 2-5 is a regime map for thermal conduction *along* epitaxial layers of the high-temperature superconductor $YBa_2Cu_3O_7$. The orthorhombic, nearly tetragonal crystal structure of this material results in similar thermal conductivities in the a and b crystal axis directions, but a different thermal conductivity in the c direction. The layers with the best superconducting properties are deposited epitaxially with the c axis normal to the layer surface, such that conduction along the layers occurs in the a-b plane. Goodson and Flik (1992) determined as functions of temperature the mean free path of each carrier and its contribution to the thermal conductivity. The thinnest high-$T_c$ superconductor layers exhibit microscale conduction in detectors and electronic circuits. Superconducting transmission lines and Josephson junctions made of thin superconducting layers are elements of hybrid superconductor-semiconductor circuits operating near 50 K (e.g., Ono, 1992). The thermal conductivities of many of these structures depend on their thicknesses. For thicknesses less than 0.01 μm, $YBa_2Cu_3O_7$ layers lose their superconducting properties.

## 2.5 Concluding Remarks

For thermal conduction in solids, the dimension which separates the microscale and macroscale regimes is related to the carrier mean free path and depends strongly on the purity, microstructure, and temperature of the solid. The regime maps developed in this chapter are only useful if the microstructure and the purity of the microelectronic structures are similar to those in bulk materials. If this is not the case, the influences of boundary scattering on the conduction process may be overwhelmed by the effects of the different

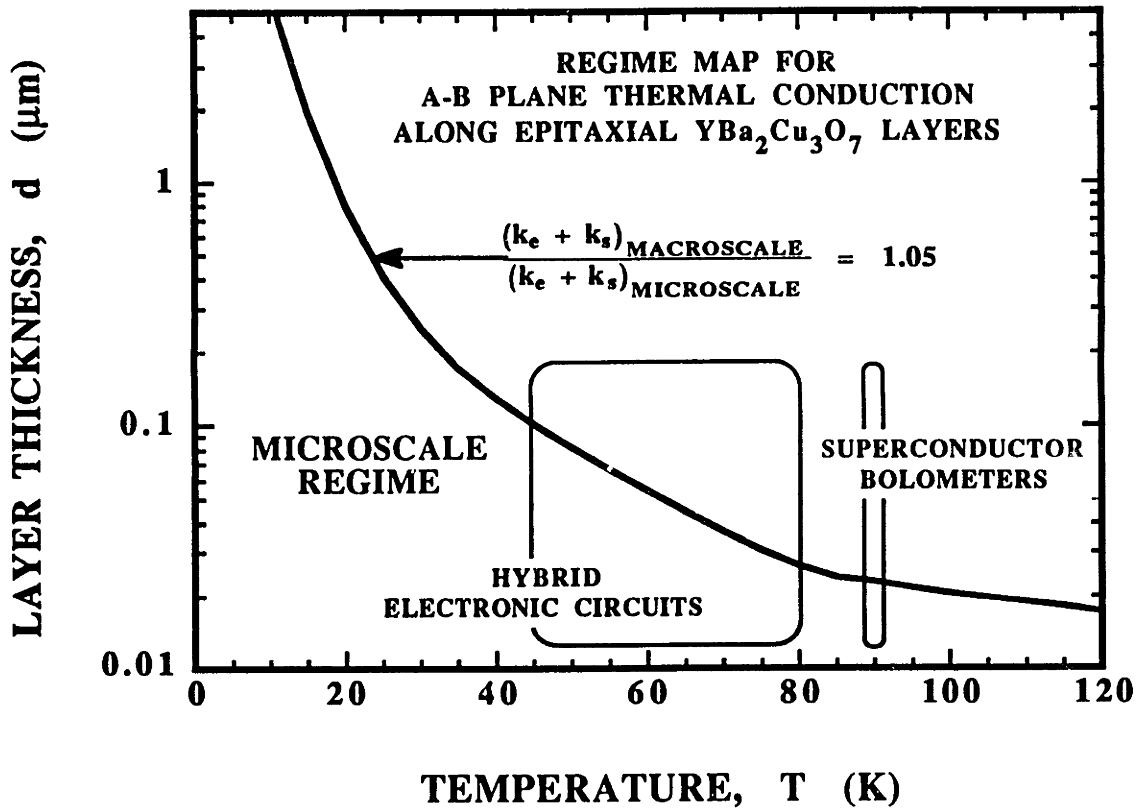


Fig. 2-5 Regime map for thermal conduction along epitaxial layers of the high-$T_c$ superconductor $YBa_2Cu_3O_7$.

microstructure and purity. This is discussed in greater detail in Chapter 5, which examines the influence of porosity on the thermal conductivity of amorphous silicon dioxide layers.

The present state of research in microscale heat transfer displays an imbalance between theoretical and experimental achievements. Several analytical studies were presented recently, such as those of Majumdar (1991), Kumar and Vradis (1991), and Chen and Tien (1992). But much more experimental work is needed to verify the predictions of these analyses. Chapter 4 assists this experimental work by reviewing measurement techniques which can investigate microscale thermal conduction processes in layers.

# 3. SOLID-LAYER THERMAL-CONDUCTIVITY MEASUREMENT TECHNIQUES

## 3.1 Introduction

The thermal conductivities of solid layers are needed for the design of field-effect transistors, optical coatings for laser systems (Guenther and McIver, 1988), and amorphous membranes in superconducting radiation detectors (Verghese et al., 1992). The thermal conductivity of a layer can differ from that of a bulk sample of the same material for two reasons. Layer fabrication techniques, such as chemical vapor deposition, can result in a different microstructure which changes the thermal conductivity. In addition, the small thickness of the layer can increase the importance of interfacial effects, such as thermal boundary resistances and the boundary scattering discussed in Chapter 2, which can reduce the effective conductivity of the layer. Techniques such as transmission electron microscopy provide information about the microstructure of layers (Marcus and Sheng, 1983), but the precise microstructural information, e.g., the grain-size distribution, point defect density, and characteristic dimension of interfacial roughness, needed for thermal-conductivity and boundary-resistance predictions is often not available. Performing experiments is usually the only way to accurately determine the thermal conductivities of layers.

Cahill et al. (1989) reviewed several techniques for measuring the thermal conductivity in the direction normal to layers, and made helpful observations about the effects of phonon-boundary scattering and interfacial layers on the measurements. Some of

these insights are presented in greater detail in the review of thermal boundary resistance by Swartz and Pohl (1989). The article of Cahill et al. (1989) is not a complete review of thermal conductivity measurement techniques, and there remains a need for a comparative survey which includes other techniques, especially those available for room-temperature measurements and those measuring the conductivity along layers. Guenther and McIver (1988) and Lambropoulos et al. (1991) surveyed the existing data for the thermal conductivity in the direction normal to amorphous dielectric layers, but in most cases provided little information about the measurement techniques used to obtain these data. As a result, it is often difficult to assess the accuracy of the techniques or their applicability to layers which have different thicknesses or are made of different materials.

This chapter helps to remedy this situation by reviewing solid-layer thermal-conductivity measurement techniques. The layer geometry is depicted in Fig. 3-1, which defines the coordinates $x$ and $y$ to be along and normal to the layer, respectively. The thermal conductivity measured in layers is not necessarily a property of the layer material. Due to phenomena such as heat-carrier boundary scattering and thermal-boundary resistances, the apparent thermal conductivities of layers often depend on the direction of heat propagation, even for isotropic materials, the layer thickness, and on the properties of the layer boundaries. For this reason, most measurements yield an *effective* thermal conductivity, which is valid only for a given layer thickness and direction of heat transport. The effective thermal conductivity along a layer is

$$k_{a,eff} = -q_x'' \left[\frac{dT}{dx}\right]^{-1} \tag{3-1}$$

where $T$ is the local layer temperature, which is assumed not to vary in the $y$ direction, and $q_x''$ is the heat flux in the $x$ direction. The thermal conductivity normal to a layer is defined

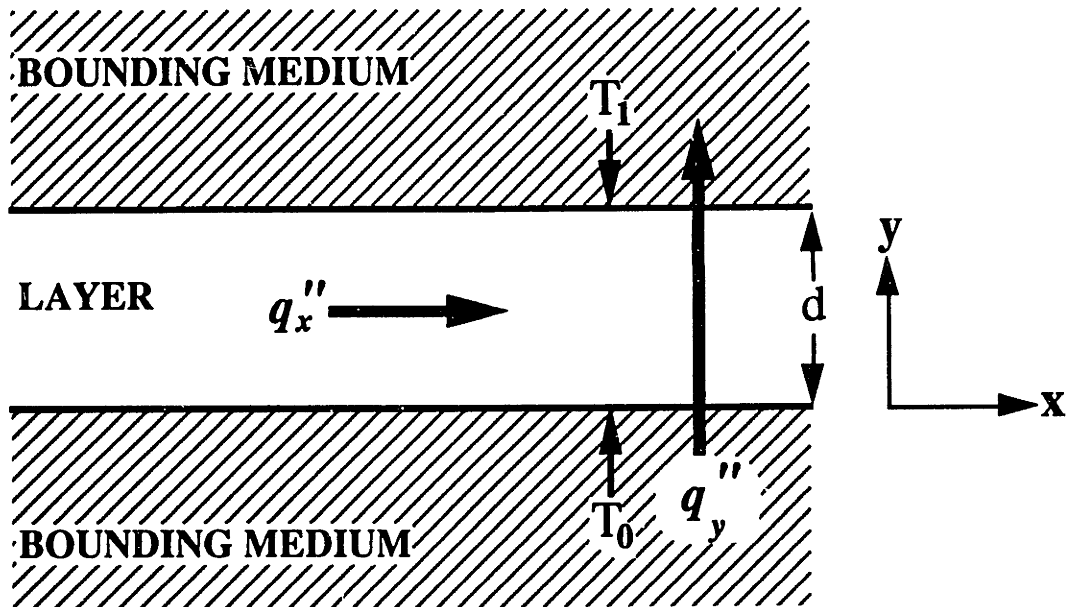


Fig. 3-1 Schematic of the layer geometry.

so that it accounts for the volume resistance of the layer *and the thermal resistances between the layer and the bounding media,*

$$k_{n,eff} = q_y'' \frac{d}{T_0 - T_1} \tag{3-2}$$

where the temperatures $T_0$ and $T_1$ are those of the bounding media just outside of the interfaces with the layer, $d$ is the layer thickness, and $q_y''$ is the heat flux in the $y$ direction. For highly-conductive layers, the in-plane conductivity $k_{a,eff}$ is important because these layers govern lateral heat conduction in multilayer structures, e.g., the silicon and aluminum thin-layer bridges in silicon-on-insulator circuits, which are investigated in Chapter 6. For layers made of materials which are poor thermal conductors, e.g., amorphous materials, $k_{n,eff}$ is of greatest importance because these layers dominate the thermal resistance in the $y$ direction. Recently, amorphous thin-layer membranes were used to thermally isolate radiation detecting elements (Verghese et al., 1992), providing an important exception to these general rules. For these membranes, the in-plane conductivity $k_{a,eff}$ governs the thermal conductance and therefore the sensitivity and time constant of the detector.

Layer thermal conductivity measurement techniques are distinguished by the time-dependence and the source of the heating they employ, as well as their method of temperature measurement. Steady-state techniques induce a time-independent heat flux, measure a resulting temperature difference or distribution, and calculate the thermal conductivity. Transient techniques induce a time-dependent heat-flux function, e.g., an impulse or a periodic function, and in most cases determine the thermal diffusivity $\alpha$ by comparing analytical solutions to the transient heat equation with a measured transient temperature. The thermal conductivity is then obtained using $k = \alpha C$, where $C$ is the bulk specific heat per unit volume. Nonporous layers of thickness large compared to the

wavelength of energy carriers, like those in most practical applications, possess the same energy-carrier densities of states and therefore the same specific heat per unit volume as bulk materials. Heating mechanisms include Joule heating, e.g., due to electrical conduction in a bridge deposited on the sample, and the absorption of laser radiation. Temperature-measurement tools include thermocouples, infrared (IR) pyrometers, and electrical-resistance thermometers.

This review separates the techniques into two basic groups: Section 3.2 discusses techniques which measure $k_{a,eff}$, and Section 3.3 discusses techniques which measure $k_{n,eff}$. The techniques are further divided into groups according to the time dependence of the heating source which is used, i.e., either a steady-state or transient time dependence. Sections 3.2.1 and 3.3.1 review steady-state techniques, and Sections 3.2.2 and 3.3.2 review transient techniques. While this work aims to be a complete review, several techniques have been omitted because of their close similarity to one of the techniques presented here.

## 3.2 Conductivity along Layers

### 3.2.1 Steady-State Techniques

Several of the techniques discussed here were applied both to free-standing layers and to layers on substrates with low thermal conductivities, e.g., lead layers on amorphous dielectric substrates. This is appropriate when the ratio $d\, k_{a,eff} / (d_{sub}\, k_{sub})$ is of the order of or larger than unity, where $d_{sub}$ is the substrate thickness and $k_{sub}$ is the substrate thermal conductivity. The temperatures in the layer and substrate are assumed not vary in the plane normal to the heat-flow direction. The total heat flow rate is the sum of the heat flow rates due to the layer and the substrate. For the case of steady-state conduction of the power $Q$ in the direction $x$ along a layer-substrate composite bridge of width $w$, the layer conductivity is

$$k_{a,eff} = -\frac{Q}{w\,d}\left[\frac{\mathrm{d}T}{\mathrm{d}x}\right]^{-1} - \frac{d_{sub}}{d}k_{sub} \tag{3-3}$$

In what follows, the term "free standing" denotes layers without substrates and layer-substrate composites for which Eq. (3-3) is used. The term "bridge" denotes a patterned portion of a layer or a layer-substrate composite which possesses a finite cross-sectional area and is long in the direction normal to the cross section.

The most common technique has been applied to free-standing thin-layer bridges from 5 K to 450 K. The bridge was attached to an isothermal heat sink at the temperature $T_0$ in a vacuum chamber, as shown in Fig. 3-2. Attached to the opposite end of the bridge, which was mechanically unsupported, was an electrical-resistance heater. The two junctions of a thermocouple were attached to the bridge, one near the free end, and the other near the heat sink. The thermocouple measured the temperature difference $\Delta T$ which occurred over the length $L$ along the bridge. The thermal conductivity $k_{a,eff}$ was determined using Eq. (3-1) with $q'' = Q/(wd)$ and $-\mathrm{d}T/\mathrm{d}x = \Delta T/L$, where $Q$ is the heating power and $w$ is the bridge width. This technique was used for lead bridges by Pompe and Schmidt (1975) from 5 K to 20 K. More recently, Morelli et al. (1988) and Graebner et al. (1992a) used this technique to measure the thermal conductivity of diamond bridges from 10 K to room temperature. The primary causes of experimental error in this technique are conduction through the thermocouple and heater wires, which can be minimized by using thin wires, and radiation from the heater. Pompe and Schmidt (1975) and Graebner et al. (1992a) used a heater near the heat sink, shown in Fig. 3-2, to investigate the magnitude of this error. When the heater near the heat sink is on and the heater at the tip is off, the temperature drop along the bridge can be used to estimate the energy flow out of the bridge due to radiation and conduction from the wires. Graebner et al. (1992a ) used several thermocouples along the length of the sample to more accurately estimate the heat leak, yielding an uncertainty of a few percent, among the smallest below room temperature.

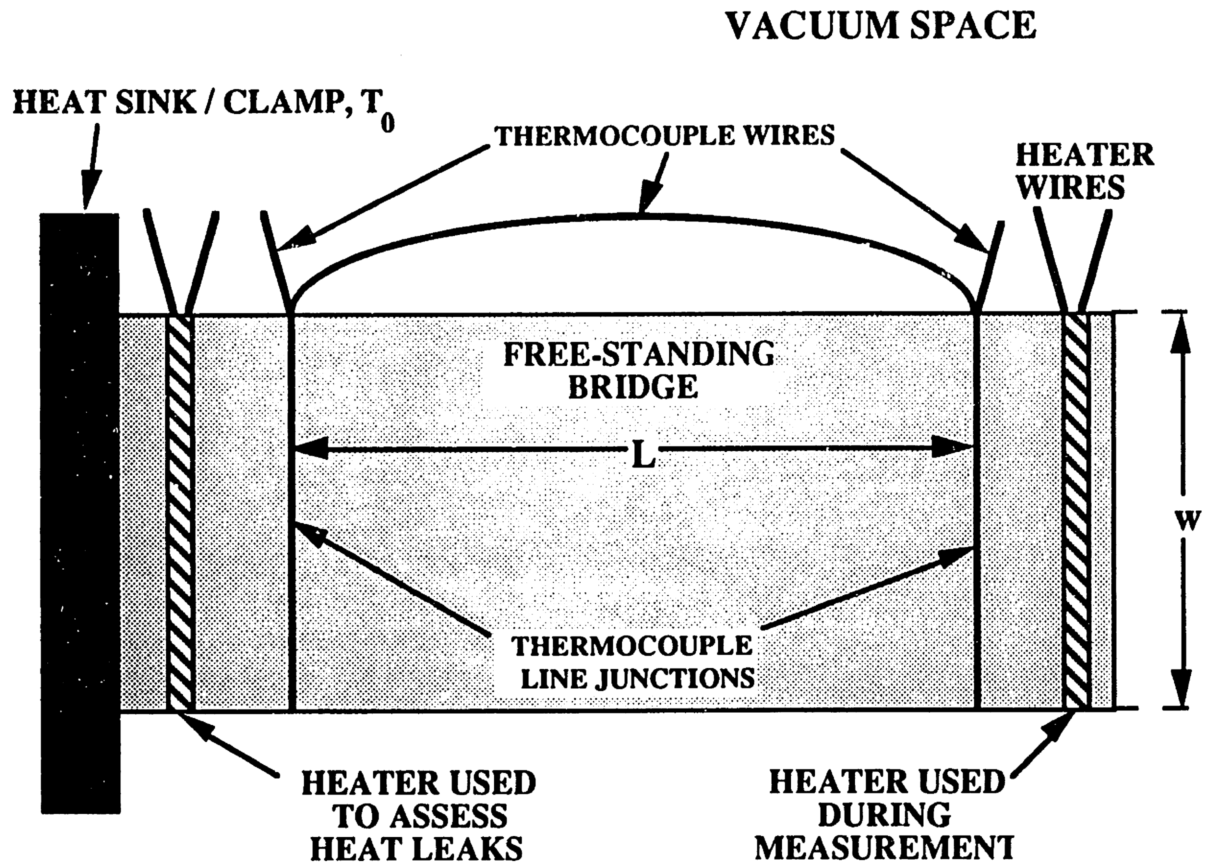


Fig. 3-2 Test structure used to measure thermal conductivity along a bridge by Pompe and Schmidt (1975).

The technique of Nath and Chopra (1973) is similar, but these authors attached the cold end of the layer to an isolated block with a known heat capacity. The other end of the bridge was secured to an isothermal heater. A thermocouple measured the temperature drop from the heater to the block. The rate of heat flow through the bridge $Q$ was radiated by the block at temperature $T$ to the nearly black surroundings at the temperature $T_0$, $Q = A\, \varepsilon\, \sigma\, (T^4 - T_0^4)$, where $A$ is area and $\varepsilon$ the emissivity of the block surface, and $\sigma$ is the Stefan-Boltzmann constant. This expression was approximated by $Q = G\,(T - T_0)$ for $(T - T_0)/ T_0 << 1$, where $G = 4\, A\, \varepsilon\, \sigma_0\, T_0^3$ is the conductance from the block. The conductance $G$ was obtained from the heat capacity of the block and the measured time dependence of the block temperature when it was allowed to cool to $T_0$. The accuracy of this technique is reduced by radiative losses from the bridge and conduction losses through the cold thermocouple junction, but is not influenced by radiation from the heater or conduction through the warm thermocouple junction. Nath and Chopra (1973) did not give the experimental uncertainty. They used this technique for copper layers on amorphous dielectric substrates above room temperature. Due to the requirement $(T - T_0)/ T_0 << 1$, this technique is most useful above room temperature.

Nath and Chopra (1973) developed a complementary low-temperature technique which uses a bare-substrate bridge and a layer-substrate composite bridge, each attached to blocks of identical heat capacity. The differences between the temperatures of the blocks and the cooling bath temperature were small and radiation was neglected. Both substrates were assumed to possess the same thermal conductivity and cross-sectional area. At time $t = 0$, the free ends of both bridges were attached to a warmer block, which was assumed to remain isothermal while cooling through the two samples. Neglecting the heat capacity of the free-standing layers, one-dimensional conduction analysis determined $k_{a,eff}$ in the layer from the substrate dimensions, the identical heat capacities of the cooler blocks, and the transient temperatures of the three blocks. This technique yields the conductivity independently from the substrate conductivity, so that Eq. (3-3) is not required. Although

this technique involves a transient response, it is discussed in this section because the heat capacity in the layer is neglected.

Boiko et al. (1973) and Völklein and Kessler (1984) developed similar techniques which measured both the thermal conductivity and the emissivity of free-standing electrically-conducting bridges. The technique of Boiko et al. (1973) was applied to metal bridges from 300-900 K, and the technique of Völklein and Kessler (1984) was applied to semimetal bridges from 80-400 K. In both cases, the sample bridge was suspended between two heat sinks at the temperature $T_0$, as shown in Fig. 3-3. Both techniques employed Joule heating in the sample bridge to induce heat flow, and solved the one-dimensional heat-conduction equation in the bridge considering Joule heating and radiation from the bridge.

Boiko et al. (1973) measured the bridge temperature at seven locations along its length using the temperature dependence of the lattice parameter of the bridge material, which was measured using electron diffraction. The change in the lattice parameter was assumed to be proportional to the product of the temperature change and the coefficient of thermal expansion. The reported uncertainty in temperature changes measured this way was +/- 5 K. As a result, large temperature changes were employed, varying between 50 K and 720 K for one set of measurements. The authors determined the values of the temperature-independent thermal conductivity $k_{a,eff}$ and the emissivity which were consistent with the heat equation and the measured temperature distribution. The large temperature changes required by this technique render it inappropriate for materials whose thermal conductivities depend on temperature, e.g., semiconductors and semimetals above room temperature.

Völklein and Kessler (1984) used much smaller temperature changes, and calculated the average thermal conductance from the bridge, i.e., the ratio of the Joule heating power dissipated in the bridge to its average temperature change, from current-voltage data. The change in the average bridge temperature from the reference temperature

$T_0$ is approximately proportional to the change of the bridge electrical resistance from its resistance when isothermal at $T_0$. Using the heat equation, the authors predicted the average thermal conductance from the bridge as a function of its thermal conductivity and emissivity, which were both assumed to be temperature independent. By measuring the thermal conductance from two bridges of different lengths but identical thermal properties, the thermal conductivity and emissivity were obtained independently. The error due to the use of a temperature-independent emissivity was not determined. This approximation needs to be examined for metals, whose normal total emissivity is nearly linearly proportional to temperature above room temperature (Siegel and Howell, 1981). This technique requires two layers of identical thermal properties. But if the emissivity of a layer is known, the thermal conductivity can be calculated from measurements performed only on that layer. This technique should only be used when radiation losses are large compared to the energy conducted along the layer, which can occur in very thin free-standing layers, and can render the basic technique depicted in Fig. 3-2 inappropriate.

Recently, Graebner et al. (1992c) and Tai et al. (1988) microfabricated novel test structures. Graebner et al. (1992c) etched the substrate from underneath rectangular 2 x 4 $mm^2$ sections of 2.8 - 13.1 μm thick diamond layers. They deposited a thin-layer heater bridge and thin-layer thermocouple bridges on the top of each diamond rectangular layer section, as shown in Fig. 3-4. The boundaries of the suspended layer were assumed to be isothermal at the heat-sink temperature, $T_0$. The validity of this assumption for the case of the highly-conductive diamond layers must be investigated. Comparison of the measured temperature profile with that predicted by a numerical solution to the two-dimensional heat-conduction equation yielded $k_{a,eff}$ in the diamond layers.

Tai et al. (1988) suspended 1.5 μm thick heavily-doped polysilicon bridges of lengths from 100 to 200 μm between phosphosilicate glass (PSG) supports. These test structures resembled microfabricated flow sensors whose thermal design requires the

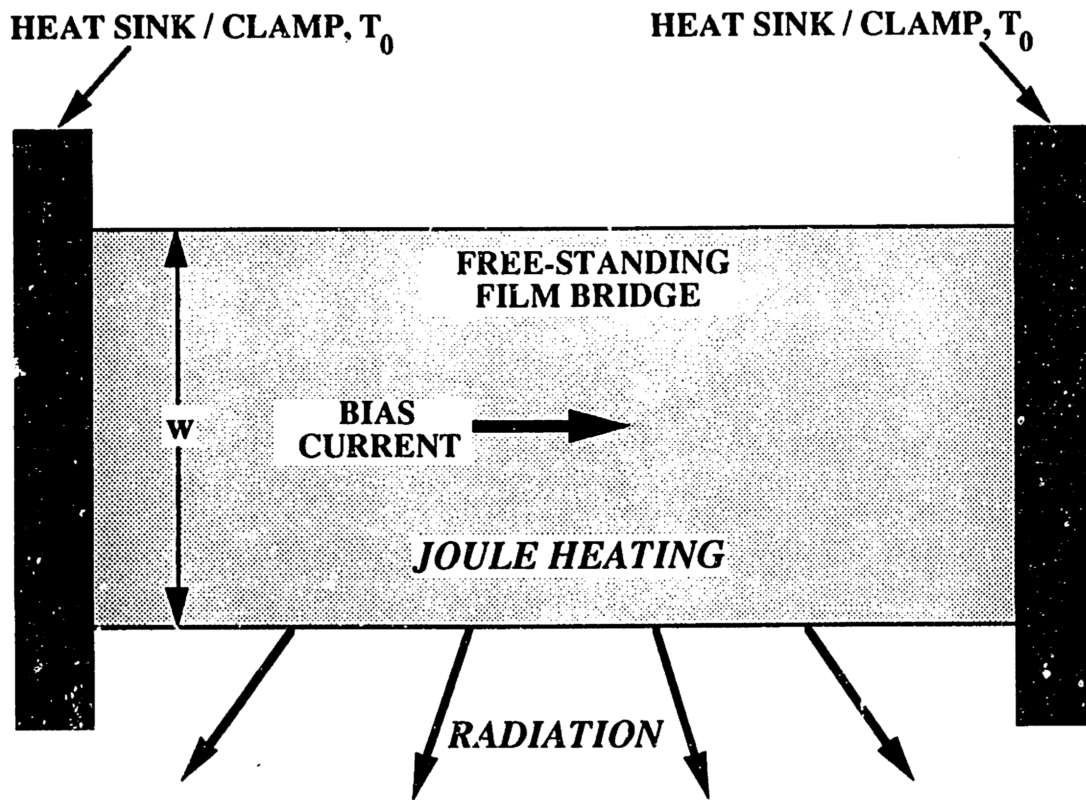


Fig. 3-3 Self-heated bridge test structure used by Boiko et al. (1973).

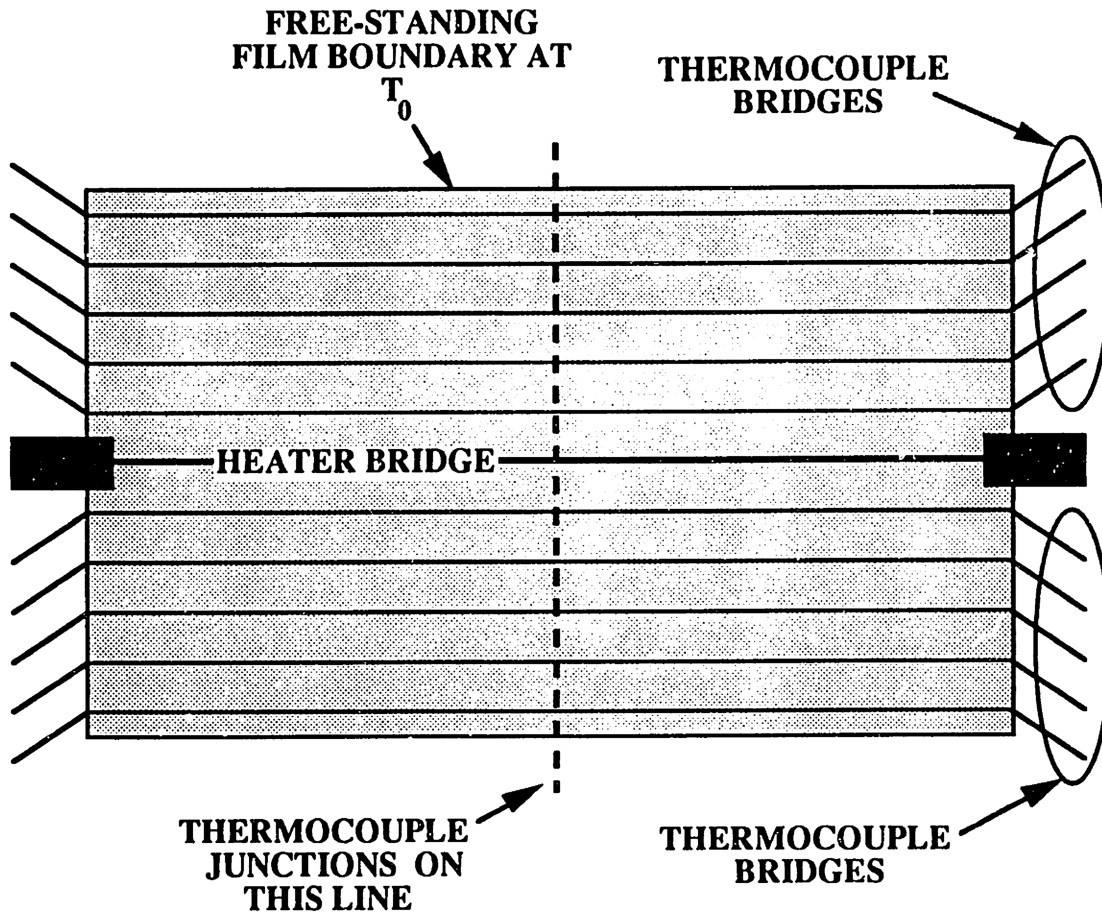


Fig. 3-4 Novel test structure of Graebner et al. (1992c) for measuring $k_{a,eff}$ of diamond layers. The substrate is etched from beneath the rectangular layer section shown.

conductivity of the doped silicon bridges. Each bridge had a short, lightly-doped center segment whose electrical resistance dominated that of the entire bridge. A bias current induced heat flow from the lightly-doped segment, and a solution to the one-dimensional heat-conduction equation yielded the conductivity of the bridge from its measured electrical resistance. The works of Graebner et al. (1992c) and Tai et al. (1988) indicated the potential of microfabrication technology to assist in the measurement of layer thermal conductivities.

Dua and Agarwala (1972) used the Wiedemann-Franz law (Kittel, 1986),

$$k_{a,eff} = \frac{L_0 T}{\rho_e} \tag{3-4}$$

where $L_0$ is the Lorenz number, to estimate the thermal conductivity of metal layers from the measured electrical resistivity $\rho_e$. Equation (3-4) is valid at temperatures above the Debye temperature, which is of the near 100 K for most metals, or when defect- or boundary-scattering dominates. The second condition is satisfied below about a fifth of the Debye temperature for most metals, but is satisfied at higher temperatures by impure metals. Equation (3-4) is accurate within 14 percent for common metals at room temperature (Kittel, 1986).

### 3.2.2 Transient Techniques

Mastrangelo and Muller (1988) used test structures similar to those of Tai et al. (1988), i.e., a heavily-doped polycrystalline-silicon bridge suspended between PSG supports. In this case the bridges were 180 - 280 μm in length and 1.3 μm in thickness and were uniformly doped. A bias current in the layer induced Joule self-heating. The authors solved the transient one-dimensional heat-conduction equation in the bridge accounting for its temperature-dependent electrical resistivity and neglecting radiation. The thermal diffusivity was obtained by comparing the predicted time-dependent electrical

resistance response with the measured response. Using the bulk specific heat, the measured thermal diffusivity values agreed well with the thermal conductivity measured in similar structures by Tai et al. (1988). These techniques are promising for the measurement of thermal conductivity values needed for flow-sensor design.

Hatta (1985) developed a technique which is illustrated in Fig. 3-5. A portion of a free-standing rectangular layer was masked from a sheet of laser light with periodic heat flux in the $y$ direction, $q_y'' = q_a''(1 + \sin \omega t)$, where $q_a''$ is the amplitude of the absorbed heat flux and $\omega$ is its angular frequency. Lying under the mask was a thermocouple junction separated from the mask edge by the distance $x$. A solution to the transient one-dimensional heat-conduction equation neglecting heat transfer from the layer yields the approximate amplitude $T_a$ of the periodic component of the temperature at location $x$,

$$T_a(x) = \frac{q_a''}{2\,\omega C\, d} \exp\left(-\frac{\lambda_T\, x}{\sqrt{2}}\right) \tag{3-5}$$

The inverse thermal-diffusion length is $\lambda_T = (\omega/\alpha)^{1/2}$, where $\alpha$ is the thermal diffusivity in the $x$ direction. The distance between the thermocouple and the mask edge can be changed by moving the mask. Equation (3-5) and the measured function $T_a(x)$ yield $\alpha$. The frequency must be small enough so that the thermal diffusion length is much larger than the layer thickness. Subsequent research investigated the influence of the thermocouple on the temperature in the layer (Hatta et al., 1986) and optimized the sample dimensions for the measurement (Hatta et al., 1987). The authors did not investigate the potential of a microfabricated thermocouple, such as those employed by Graebner et al. (1992c), for measuring temperature without disturbing the layer conduction.

Similar techniques developed by Visser et al. (1992) and Shibata et al. (1991) avoided the influence of the thermocouple on conduction in the layer by using an infrared (IR) pyrometer to measure the layer temperature. Visser et al. (1992) used a highly-

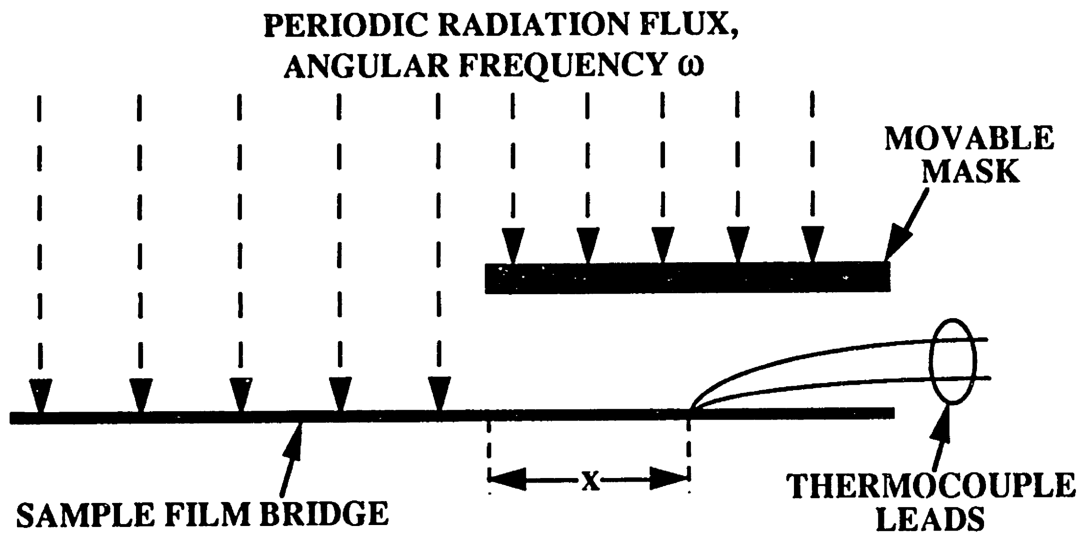


Fig. 3-5 Side view of the experimental set-up of Hatta (1985) for measuring the thermal diffusivity along layers heated by a sheet of laser light. The mask was moved to change the distance $x$ while the thermocouple junction remained fixed.

focussed, periodic laser beam to heat a spot with diameter near 10 μm on a layer of large dimensions. A solution to the transient one-dimensional heat equation with cylindrical coordinates accounts for heat transfer from the layer and yields the phase and amplitude of the periodic temperature as a function of $\alpha$, $C$, the distance from the focus, and the heat transfer coefficient $h$ from the layer surface to the ambient temperature. Fitting the measured amplitude and phase of the temperature fluctuations to the predictions yields $\alpha$ and $h$. In the techniques of Hatta (1985) and Visser et al. (1992), the phase of the temperature fluctuations yields the thermal diffusivity without requiring the heat transfer coefficient $h$. The primary advantage of these techniques is that they are non-contact.

Shibata et al. (1991) employed a brief line pulse of 0.694 μm ruby laser light of duration $t_L$ and width $2l$ to irradiate a rectangular free-standing layer section. The line cut across the entire width $w$ of the layer section at its center, inducing one-dimensional heat conduction along its length. The half-width $l$ and the time duration $t_L$ of the laser-pulse line satisfied $l^2 >> \alpha_a t_L$, and the transient temperature in the layer was calculated by assuming an initial temperature change $T_i - T_0 = E / (2l\, d\, w\, C)$ in the irradiated portion of the layer, where $E$ is the total energy deposited. Finite-length effects and heat transfer from the layer were neglected. The temperature was detected from the bottom of the layer at a distance from the heat source which was large compared to the layer thickness, and the solution to the heat equation yielded the thermal diffusivity from the time required for the measured temperature to achieve half of its maximum value. The authors stated that the short duration of the experiment rendered heat transfer from the layer insignificant, but the impact of neglecting this heat transfer needs to be assessed.

For the case of layers with low absorptances, the optical techniques discussed above required the deposition of a thin absorbing coating to the layer. For coatings of low thermal diffusivity, the thermal energy cannot diffuse quickly enough through the coating during the relevant time interval, e.g., one period of the laser flux. If the diffusivity of the coating is too high, however, it contributes to transport in the plane of the layer. Visser et

al. (1992) investigated the influence of the coating material by comparing measured values of the thermal diffusivity of 100 μm copper sheets with the thermal diffusivity of bulk copper for different coating materials. They found that the use of the wrong coating material could severely affect the measured diffusivity, but they achieved reasonable results using a graphite spray. The influence of the coating material on the diffusivity measurement increases with decreasing layer thickness. Further investigation are needed to determine the usefulness of optical techniques for measuring the thermal diffusivity of thin layers with low absorptances. At present, the need for an optical coating renders these techniques inappropriate for layers of thicknesses relevant to electronic devices.

## 3.3 Conductivity normal to Layers

### 3.3.1 Steady-State Techniques

All of the techniques described in Section 3.3.1 apply only to layers on substrates satisfying $k_{n,eff} << k_{sub}$. Goldsmid et al. (1983) developed a technique to measure the thermal conductivity of an amorphous silicon layer, which was deposited on half of a substrate as shown in Fig. 3-6. Two bismuth bridges were deposited, one each on the layer and on the bare substrate. An antimony bridge was deposited over the two bismuth bridges as shown, yielding two thermocouples. The portion of the sample in the dashed rectangle in Fig. 3-6 was coated to enhance radiation absorption. The thermocouple junctions were heated sequentially using a disc of laser light with radius $r_c$ = 55 μm. For each case, all of the laser light was incident on the junction. The temperature rise due to the laser light was measured for each case. The ratio of the temperature rise of the thermocouple above the sample layer and the temperature rise of the thermocouple above the bare substrate is $U_T$. The substrate was modelled as a semi-infinite medium with thermal resistance $R_{sub} = (\pi/4)(r_c/k_{sub})$, corresponding to heat flow in a semi-infinite medium originating from an isothermal disc of radius $r_c$. The thermal resistance of the

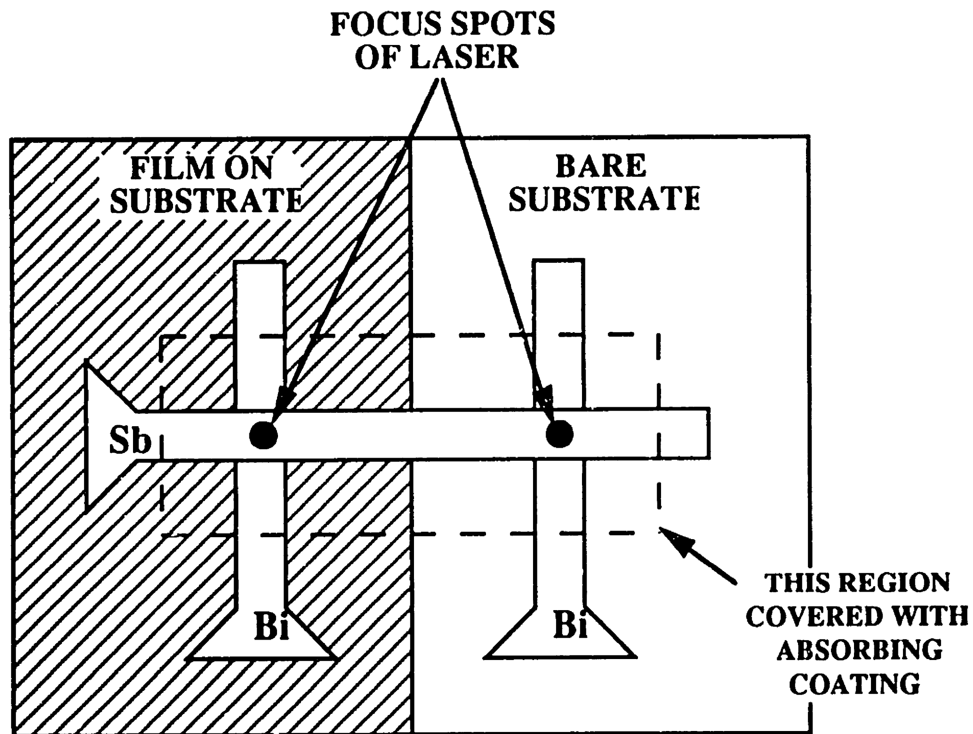


Fig. 3-6 Top view of test structure of Goldsmid et al. (1983) for measuring $k_{n,eff}$.

sample layer is $d/k_{n,eff}$, and the thermal resistance between the thermocouple junction and the sample surface is $d_T/k_T$, where $d_T$ and $k_T$ are the thickness and thermal conductivity of the bismuth layer, respectively. The effective layer thermal conductivity $k_{n,eff}$ can be determined by equating the ratio of the temperature changes to the ratio of the summed resistances,

$$U_T = \frac{R_{\text{sub}} + \frac{d_T}{k_T} + \frac{d}{k_n}}{R_{\text{sub}} + \frac{d_T}{k_T}} \tag{3-6}$$

This technique is attractive because it does not require knowledge of the absorbed power. However, the calculation of $R_{sub}$ requires accurate knowledge of the laser beam diameter, which results in a +/- 9 percent error in the measurements. The uncertainty due to modelling the substrate as a semi-infinite medium and due to lateral conduction in the thermocouple bridges needs to be assessed. If these uncertainties are satisfactorily low, this could be a useful technique for many applications.

The technique of Cahill et al. (1989) was originally developed for the measurement of the thermal boundary resistance between metal layers and dielectric substrates at low temperatures (Swartz and Pohl, 1987), but can also measure $k_{n,eff}$ of a layer deposited between the metal and the substrate. Figure 3-7 shows a cross section of the test structure. Two long, parallel metal resistance-thermometer bridges were deposited on the sample layer, each of width about $w = 1$ µm, separated by about $x_s = 1$ µm. Bridge A carried a large current density, serving as a heater, while bridge C carried a low current density and experienced negligible Joule heating. The energy dissipated in bridge A traveled through the sample layer, resulting in a heater-substrate temperature difference. The temperature $T_A$ of the heater bridge was determined from its electrical resistance. Bridge C measured $T_C$, from which $T_B$ was calculated by modelling the substrate as a semi-infinite medium.

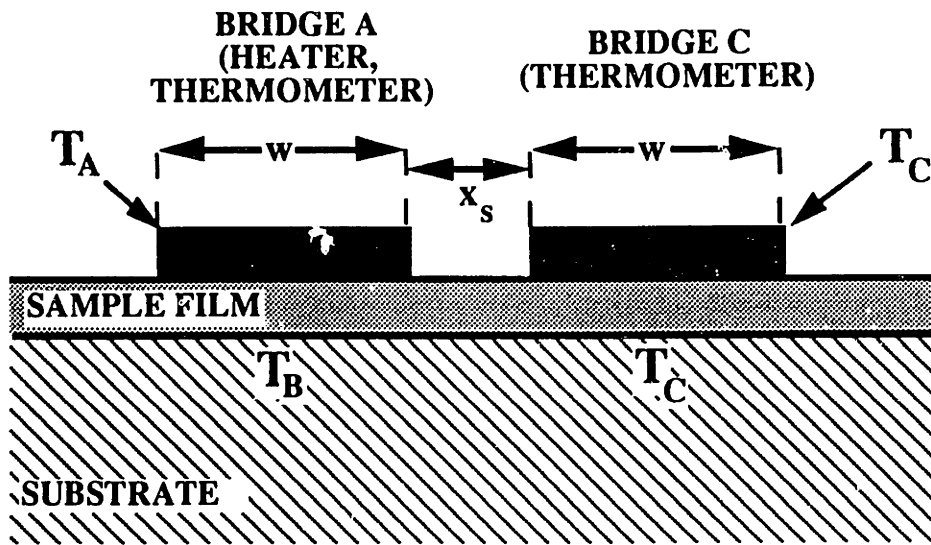


Fig. 3-7 Cross section of test structure of Cahill et al. (1989) for measuring $k_{n,eff}$.

The total power dissipated in bridge A is $Q$, and the width and length of bridge A are $w$ and $L$. The effective thermal conductivity for conduction normal to the layer is

$$k_{n,eff} = \frac{Q\ d}{w\ L\ (T_A - T_B)} \tag{3-7}$$

This is a very effective technique. The approximations employed in the thermal analysis are only important when the temperature difference in the substrate beneath the two bridges is comparable to the temperature difference normal to the sample layer. This occurs in very thin layers near room temperature, where the substrate thermal conductivity is lower than at low temperatures. Section 5.4 presents a more detailed analysis of conduction in the substrate for this technique and an estimate of the experimental uncertainty as a function of the thermal resistance to conduction normal to the sample layer. The uncertainty analysis given in Section 5.4 employs measurements by a second non-heating bridge. The separation between bridges A and C is optimized by balancing the competing goals of minimizing the effects of conduction *along* the sample layer on the temperature $T_C$, and minimizing the temperature difference $T_B - T_C$. The technique is then used to measure $k_{n,eff}$ for amorphous silicon dioxide layers of thicknesses as low as 300 Å near room temperature.

Schafft et al. (1989) and Brotzen et al. (1992) also used metal bridges as Joule heaters when they measured $k_{n,eff}$ for amorphous silicon dioxide layers. Both techniques employ only a single bridge. The temperature at the interface between the silicon dioxide layer and the silicon substrate was obtained by an analysis of heat conduction in the substrate, which assumes that the bottom surface of the substrate was isothermal. For the case of Schafft et al. (1989), who measured 1.7 and 3 μm layers using a 3.4 μm wide heater bridge, this resulted in little error because the measured thermal resistance of the silicon dioxide was more than twenty times that of the substrate. As in the technique of

Cahill et al. (1989), the heater bridge was a resistance thermometer. Since the ratio $w/d$ was of the order of unity, the two-dimensional heat-conduction equation was solved in the sample layer to determine its thermal conductivity. The assumptions used to solve the heat-conduction equation in the substrate would need further investigation if this technique were applied to thinner layers.

Brotzen et al. (1992) measured $k_{n,eff}$ of layers of thickness down to 1000 Å using a 0.19 mm wide heater bridge. The temperature drop in their substrate was significant because the sample layer was thinner and the ratio $w/d_{sub}$, where $w$ is the heater bridge width, was much larger than in the measurements of Schafft et al. (1989). Increasing this ratio causes the two-dimensional conduction in the substrate to approach one-dimensional conduction normal to the substrate, which increases the substrate thermal resistance. The influence of two important assumptions on the analysis of Brotzen et al. (1992) was not investigated: (a) The aluminum heat sink was assumed to be isothermal and (b) the boundary resistance between the heat sink and the substrate was neglected. Both assumptions are questionable because of the large value of $w/d_{sub}$, which was of the order of unity, and may have resulted in an overprediction of the temperature at the bottom interface of the sample layer and therefore an underprediction of $k_{n,eff}$. The investigation of these issues is especially important because Brotzen et al. (1992) reported values of $k_{n,eff}$ which are much smaller than those measured in bulk samples. It is not yet possible to determine whether this difference was due to a different layer property or to the approximations in the heat-conduction analysis.

The technique of Cahill et al. (1989), which is employed in Section 5, is more accurate than those of Schafft et al. (1989) and Brotzen et al. (1992) because the temperature under the sample layer is calculated using the substrate temperature measured nearby. As a result, $k_{n,eff}$ is less sensitive to approximations in the thermal analysis, yielding a much higher experimental certainty.

Lambropoulos et al. (1989) modified the thermal comparator technique, which was developed by Powell (1957) to measure the thermal conductivity of bulk materials, to measure $k_{n,eff}$ for layers on substrates. A sensing finger and thermocouple apparatus were mounted in a copper heating block as shown in Fig. 3-8. One junction of the thermocouple was at the tip of the finger while the other was inside the block. The temperatures of the copper block and the sample were maintained at 329 K and 309 K, respectively. During the measurements, the finger was pressed against the sample with a controlled force and the steady-state thermocouple voltage was recorded. The samples were assumed to be well modelled as semi-infinite media. The temperature of the sensing tip decreased and the thermocouple voltage increased with the increasing thermal conductivities of the sample materials. Measurements performed on bulk samples with known thermal conductivities yielded a calibration curve from which the apparent thermal conductivity of a sample, $k_{app}$, could be obtained from the thermocouple voltage. For a layer on a substrate, $k_{n,eff}$ can be calculated by assuming the thermal resistance of the substrate is $R_{sub} = (\pi/4)(r_c/k_{sub})$, the same relation used by Goldsmid (1983). The difference between $R_{sub}$ and the apparent resistance $R_{app} = (\pi/4)(r_c/k_{app})$ is due to the layer resistance $d/k_{n,eff}$, yielding

$$k_n = \frac{4\,d}{\pi\, r_c}\left(\frac{1}{k_{app}} - \frac{1}{k_{sub}}\right)^{-1} \tag{3-8}$$

This expression is valid when $r_c >> d$ is satisfied.

The main uncertainty in this technique is due to the determination of the contact-spot radius $r_c$. Powell (1957) showed that the thermocouple voltage varied rapidly with the applied force, which was attributed to a change in the contact area. The contact area also varied with the hardness and elastic properties of the material. While this resulted in less than 6 percent error for many materials, including aluminum, steel, and silicon dioxide, data for lead fell far from the calibration curve established using these materials. Powell (1957) required that $r_c$ was the same during calibration and measurement, but did not need

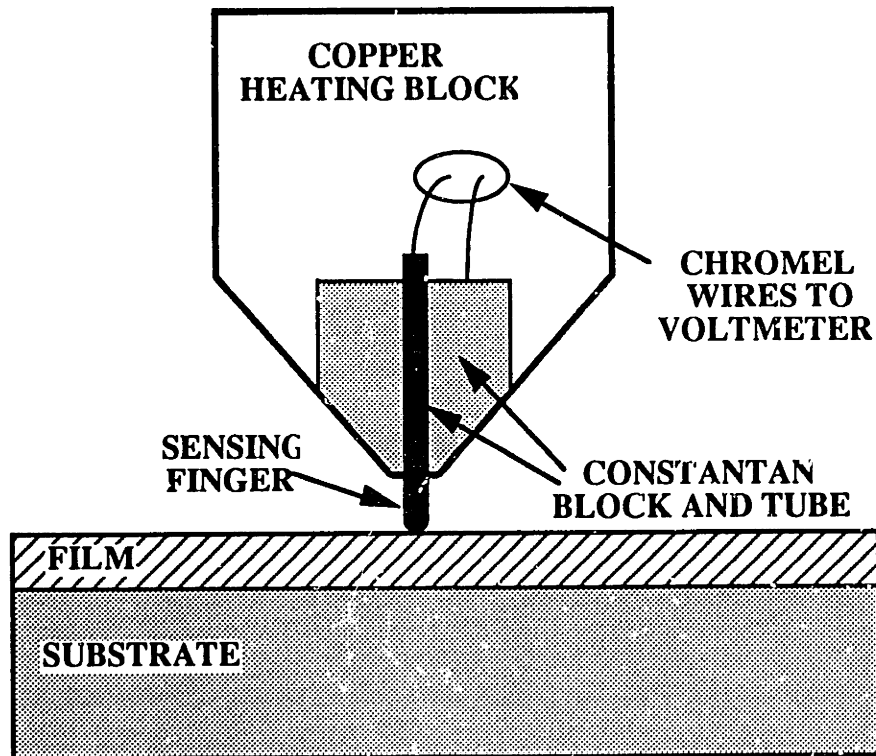


Fig. 3-8 Schematic of the thermal comparator used by Lambropoulos et al. (1989).

to determine its magnitude. In contrast, the accuracy of the measurements of Lambropoulos et al. (1989) required both a constant value of $r_c$ and the knowledge of its magnitude, which appears in Eq. (3-8). Thus, the uncertainty due to the differences in the hardnesses of materials is augmented by the uncertainty in the contact radius magnitude. Lambropoulos et al. (1989) reported a +/- 80 percent uncertainty in $r_c$, which was estimated using elastic contact theory and optical inspection. After performing measurements on a variety of dielectric layers, they concluded that in almost all cases the layer thermal conductivity was significantly lower than the bulk conductivity. In many cases, however, the bulk values of the conductivity fell within the experimental uncertainty of the measured values. This method is attractive because it is nondestructive, and can be rapidly applied to surface layers. But the technique will be quantitatively useful only when the uncertainty in the contact radius can be dramatically reduced.

### 3.3.2 Transient Techniques

There are two types of transient techniques which measure the thermal conductivity normal to layers. Techniques of the first type use periodic heating on the surface of the layer, and determine the thermal conductivity from the periodic temperature at the layer surface. The most common version of this approach is the 3-$\omega$ technique of Cahill et al. (1989), who applied the technique developed by Cahill and Pohl (1987) for bulk amorphous solids to thin layers. A thin, narrow bridge was deposited on the layer-substrate composite. The bridge served both as a heater and as an electrical-resistance thermometer. The bridge carried a sinusoidal current of angular frequency $\omega$. Because positive and negative currents both heated the bridge, the frequency of the rate of heating was $2\omega$. The inverse thermal diffusion length for this case is $\lambda_T = (2\omega/\alpha)^{1/2}$. The amplitude of the temperature oscillations in the layer is approximately (Carslaw and Jaeger, 1959)

$$T_a(r) = \frac{q_a'}{\pi k} K_0(\lambda_T r) \quad (3\text{-}9)$$

where $K_0$ is the modified Bessel function of order zero, $r$ is the distance from the heating source, and $q_a'$ is the amplitude of the energy deposited in the bridge per unit time and length. This assumes that the bridge is a line source and neglects any variation in the properties of the semi-infinite medium with depth. The frequency of the temperature oscillations is equal to that of the driving source, $2\omega$. For $\lambda_T r << 1$, the Bessel function may be approximated, yielding the derivative

$$\frac{\partial T_a(r)}{\partial [\ln(\omega)]} = - \frac{q_a'}{2 \pi k} \quad (3\text{-}10)$$

The electrical resistance of the bridge varies linearly with temperature. The voltage along the bridge is the product of the applied bias current, periodic with frequency $\omega$, and the bridge electrical resistance, periodic with frequency $2\omega$. This yields a small component of the voltage signal with frequency $3\omega$ whose amplitude is related to the amplitude of the periodic bridge temperature. The thermal conductivity can be obtained using Eq. (3-10) and the bridge-temperature amplitude at two frequencies.

This technique has the advantage of allowing the thermal conductivity to be probed within a desired thickness of the layer-substrate composite. For $d \lambda_T << 1$, where $d$ is the layer thickness, it measures the properties of the substrate. For $d \lambda_T >> 1$, it yields the properties of the layer. The resolution of the technique is limited by the requirement for radial symmetry about the heater bridge, $\lambda_T w << 1$, where $w$ is the width of the bridge. The available fabrication technology yields a minimum layer thickness of about 10 µm. For the opposing limit, $\lambda_T w >> 1$, the conduction is approximately one-dimensional in rectangular coordinates. The possibility of using this limit to measure the thermal conductivity of thinner layers should be explored.

The value of the thermal conductivity obtained using the 3-$\omega$ technique is not necessarily equal to $k_{n,eff}$. If the thermal conductivity is anisotropic, the radial symmetry of the technique yields a conductivity which is a function of the thermal conductivities both normal to and along the layer. If the thermal conductivity in the layer is nonuniform, the measured value is affected most by regions near the surface of the layer. The influence of thermal boundary resistances on this technique has not been assessed. These could be important, particularly at low temperatures, and it may be possible to use this technique to measure thermal boundary resistances. The thermal conducitivity obtained using the 3-$\omega$ method may not be appropriate for analyzing steady-state conduction normal to thin-layered structures. The steady-state technique of Cahill et al. (1989) is much better for this case, and is much simpler to perform. But the 3-$\omega$ method is probably the best available for investigating a layer within a targeted depth.

The second type of transient technique for measuring the thermal conductivity normal to layers is non-contact and applies to free-standing layers. A brief pulse of laser energy is applied at the layer surface, and the thermal conductivity is calculated from the transient temperature at the back of the layer, measured using IR thermography. This approach was recently applied to amorphous polymer layers by Tsutsumi and Kiyotsukuri (1988), to metals by Shibata et al. (1991), and to diamond layers by Graebner et al. (1992b). Like the optical techniques discussed in Section 3.2.2, this one benefits from the deposition of optically-absorbing layers on the front and rear surfaces. The thermal resistances and heat capacities per unit area of these layers can be made small compared to those of the sample layer. For a sheet of laser light incident on one surface of the layer, the analysis of one-dimensional conduction through the layer yields the approximate temperature rise at the opposite side at time $t$ after the energy deposition (Graebner et al., 1992b),

$$\Delta T(t) = \frac{E''}{C\,d}\left[1 + 2\sum_{i=1}^{\infty}(-1)^n \exp\left(\frac{-i^2\pi^2}{d^2}\alpha\, t\right)\right] \tag{3-11}$$

where $\alpha_n$ is the thermal diffusivity in the direction normal to the layer, $E''$ is the energy deposited per unit area and $C$ is the specific heat per unit volume. Fitting the measured response of the detector to Eq. (3-11) yields $\alpha$. Both the period of the pump laser and the response time of the detector need to be much smaller than $d^2 / \alpha$. This limits the practical application of this technique to layers relatively thick compared to those in microelectronic circuits. For 5 μm amorphous layers at room temperature, $d^2 / \alpha$ is of the order of 25 μs, which requires a rather fast IR detector. The time constant is several orders of magnitude faster for highly-conductive layers, such as silicon and diamond, limiting this technique to layers several tens of micrometers thick. The possibility of using an electrical-resistance thermometer bridge, deposited on the back surface of the layer, should be investigated. This would increase the response time for the temperature measurement by several orders of magnitude, allowing thinner layers to be measured.

## 3.4 Summary and Recommendations

The techniques measuring the thermal conductivity along layers are summarized in Table 3-1. The most versatile is the standard steady-state technique for free-standing layers used by Pompe and Schmidt (1973), but the periodic optical techniques of Hatta (1985) and Visser et al. (1992) are promising. The application of these techniques to very thin layers with low absorptances is questionable because of the necessity for optical coatings, which can perturb the measurement. These optical techniques will be more useful if the coatings are optimized and the error for thin layers is investigated. Graebner et al. (1992c), Tai et al. (1988), and Mastrangelo and Muller (1988) developed novel microstructures for thermal conductivity measurements.

Techniques measuring the effective thermal conductivity normal to layers are summarized in Table 3-2. Goldsmid (1983) developed a useful technique whose uncertainty needs further investigation. The technique of Cahill et al. (1989) is the most accurate because it comes the closest to measuring the temperature on both sides of the sample layer. The technique of Lambropoulos et al. (1989), which employs a thermal comparator, is an easily-applied nondestructive technique, but requires much more work to

Table 3-1 Summary of techniques measuring the effective thermal conductivity along layers.

| | **Thin-Layer Test Structure** | **Tested Temp. Range** | **Heating Time-Dependence and Source** | **Temperature Measurement** | **References** |
|---|---|---|---|---|---|
| **1** | free-standing bridge | 10-450 K | steady-state heater | thermocouple | Nath and Chopra (1973); Morelli et al. (1988) |
| **2** | free-standing electrically conducting bridge | 80-700 K | steady-state or periodic Joule heating | sample-bridge resistance | Völklein and Kessler (1984); Mastrangelo and Muller (1988); Boiko et al. (1973); Tai et al. (1988) |
| **3** | substrate etched from rectangular portion of layer | near 300 K | steady-state heater-bridge | thermocouple bridges | Graebner et al. (1992c) |
| **4** | free-standing bridge | near 300 K | periodic laser sheet on half of bridge | thermocouple | Hatta (1985) |
| **5** | free-standing bridge | near 300 K | laser pulse, line focus | IR thermography | Shibata et al. (1991) |
| **6** | free-standing plane | near 300 K | periodic laser, point focus | IR thermography | Visser et al. (1992) |

precisely determine the contact area. The 3-$\omega$ technique of Cahill et al. (1989) allows a targeted depth within the layer to be probed, but is limited to layers thicker than about 10 μm.

This review shows that more detailed uncertainty analysis is required for most of the techniques available. Uncertainty analysis is made more important by the large heat

Table 3-2 Summary of techniques measuring the effective thermal conductivity normal to layers.

| | Thin-Layer Test Structure | Tested Temp. Range | Heating Time-Dependence and Source | Temperature Measurement | References |
|---|---|---|---|---|---|
| 1 | dielectric layer on substrate | near 300 K | steady-state laser, disc-shaped focus | thermocouple bridges | Goldsmid et al. (1983) |
| 2 | dielectric layer on substrate | 10-400 K | steady-state heating bridge | bridge resistance thermometers | Cahill et al. (1989); Schafft et al. (1989) |
| 3 | dielectric layer on substrate | near 300 K | steady-state heating bridge | thermocouple on heater | Brotzen et al. (1992) |
| 4 | layer on substrate | near 300 K | heated copper block | thermocouple | Lambropoulos et al. (1989) |
| 5 | layer on substrate | 1 - 300 K | periodic heating bridge | bridge resistance thermometer | Cahill et al. (1989) |
| 6 | free-standing layer | near 300 K | laser pulse, sheet | IR thermography | Graebner et al. (1992b); Shibata et al. (1991); Tsutsumi and Kiyotsukuri (1988) |

fluxes present in thin layers in microelectronic circuits. A relatively small error in the measured conductivity of a layer can cause a large absolute temperature error, resulting in inaccurate predictions of the circuit performance and reliability.

The microstructures of thin layers depend strongly on the fabrication techniques used to make them. Thermal conductivity measurements should be performed using microstructures fabricated by the same processes as those of the real devices for which the thermal conductivity is needed, as was done by Tai et al. (1988) and Mastrangelo and Muller (1988).

# 4. TECHNIQUES FOR ANALYZING MICROSCALE CONDUCTION PROCESSES IN DIELECTRICS AND SEMICONDUCTORS

## 4.1 Introduction

The regime maps developed in Chapter 2 show when thermal analysis of a microelectronic structure must consider the boundary scattering of heat carriers. This chapter investigates the techniques available for this microscale analysis in dielectrics and semiconductors. The techniques are based on the microscopic equation of phonon transport developed by Peierls (1929; 1955). The equation is very similar to the Boltzmann equation for molecular transport (Boltzmann, 1964; Tien and Lienhard, 1979), and offers a similar ability to investigate the interaction of carriers with boundaries. While the collision integral in the molecular transport equation can sometimes be evaluated explicitly, the complexity of phonon scattering processes necessitates the use of the relaxation-time approximation to this integral when solving the Peierls-Boltzmann equation. Section 4.2 presents the transport equation and the relaxation-time approximation. Section 4.3 reviews the techniques available for solving the equation.

## 4.2 The Peierls-Boltzmann Equation

Predictions of phonon energy transport are based on the Peierls-Boltzmann equation (Beck, 1975),

$$\frac{\partial N(\vec{q}, \vec{r}, t)}{\partial t} + \nabla \cdot [\vec{v}(\vec{q})\, N(\vec{q}, \vec{r}, t)] = \left[\frac{\partial N(\vec{q}, \vec{r}, t)}{\partial t}\right]_{COLL} \tag{4-1}$$

where the right-hand side is the collision integral. The equation must be satisfied in space $\vec{r}$ and time $t$ by each phonon mode, which is distinguished by its wavevector $\vec{q}$. The symbol $\nabla$ is the gradient operator in space. The number of phonons in the mode $\vec{q}$ at location $\vec{r}$ and time $t$ is $N(\vec{q}, \vec{r}, t)$, and their velocity is $\vec{v}(\vec{q})$. The velocity $\vec{v}(\vec{q})$ of phonons in a mode is often assumed not to vary in space, allowing the second term to be written $\vec{v}(\vec{q}) \cdot \nabla N(\vec{q}, \vec{r}, t)$. The collection of all $N(\vec{q}, \vec{r}, t)$ for a given time and location is approximated by a function, called the phonon distribution function. Equation (4-1) and those which follow are written for a single phonon branch, e.g., the longitudinal branch, corresponding to compression lattice waves. But the arguments and conclusions given here are valid for a real system, which has longitudinal and transverse branches, corresponding to compression and shear lattice waves.

#### 4.2.1 Energy Conservation

The energy of a single phonon is $h_P\, \omega(\vec{q})$, where $h_P = 1.05 \times 10^{-34}$ J s is Planck's constant divided by $2\pi$, $\omega$ is the phonon frequency, and $\omega(\vec{q})$ is the phonon dispersion relation (Kittel, 1986). The phonon energy per unit volume is

$$u(\vec{r}, t) = \frac{1}{V_0} \sum_{\text{all } \vec{q} \text{ in } V_0} h_P\, \omega(\vec{q})\, N(\vec{q}, \vec{r}, t) \tag{4-2}$$

The summation and those which follow are over all of the finite number of wavevectors which are available in the volume $V_0$. Techniques for determining these wavevectors were discussed by Peierls (1955). The net energy flux is

$$\vec{J}_E(\vec{r}, t) = \frac{1}{V_0} \sum_{\text{all } \vec{q} \text{ in } V_0} h_P\, \omega(\vec{q})\, \vec{v}(\vec{q})\; N(\vec{q}, \vec{r}, t) \tag{4-3}$$

Energy conservation requires

$$\frac{\partial u(\vec{r}, t)}{\partial t} + \nabla \cdot \vec{J}_E(\vec{r}, t) = \dot{u}_g(\vec{r}, t) \tag{4-4}$$

where $\dot{u}_g(\vec{r}, t)$ is the energy added to the phonon system per unit volume and time. If the phonons are the only carriers of energy in the material, as in dielectrics, it is valid to assume $\dot{u}_g(\vec{r}, t) = 0$. This is not an appropriate simplification when there is significant interaction between phonons and other energy carriers, as in doped semiconductors or during the absorption of thermal radiation energy or electron-beam energy. For these cases, $\dot{u}_g(\vec{r}, t)$ is the net rate of energy transfer from other carriers to the phonon system per unit volume and time. If simultaneous phonon and electron transport is studied, $\dot{u}_g(\vec{r}, t)$ accounts for the energy exchange between the two systems due to electron-phonon collisions.

If Eq. (4-1) is multiplied by $h_P\, \omega(\vec{q})$ and summed over all wavevectors, the first and second terms on the left of the resulting equation are respectively identical to the first and second terms on the left of the energy Eq. (4-4), yielding the requirement for energy conservation

$$\frac{1}{V_0} \sum_{\text{all } \vec{q} \text{ in } V_0} h_P\, \omega(\vec{q}) \left[\frac{\partial N(\vec{q}, \vec{r}, t)}{\partial t}\right]_{\text{COLL}} = \dot{u}_g(\vec{r}, t) \tag{4-5}$$

### 4.2.2 Relaxation-Time Approximation

Quantitative predictions of phonon transport in solids use the relaxation-time approximation (Beck, 1975),

$$\left[\frac{\partial N(\vec{q},\vec{r},t)}{\partial t}\right]_{\mathrm{COLL}} = \frac{N_0\left[\omega(\vec{q}),\, T(\vec{r},t)\right] - N(\vec{q},\vec{r},t)}{\tau_R\left[\omega(\vec{q}),\, T(\vec{r},t)\right]} + \frac{N_{0d}\left[\omega(\vec{q}),\, \vec{v}_d(\vec{r},t),\, T(\vec{r},t)\right] - N(\vec{q},\vec{r},t)}{\tau_N\left[\omega(\vec{q}),\, T(\vec{r},t)\right]} \tag{4-6}$$

For a system which is not in equilibrium, the thermodynamic temperature of the phonon system is not defined. The local temperature $T(\vec{r},t)$ must be viewed as a parameter which is used to calculate the rates of scattering of the phonons at location $\vec{r}$ and time $t$, and guidelines for its determination are given in the next subsection. The relaxation time $\tau_R$ is for resistive scattering processes, such as phonon-defect and phonon-phonon Umklapp scattering, which do not conserve the sum of the local phonon momenta. It determines the rate of the relaxation of the distribution function to the *local equilibrium distribution function*, which is the Planck distribution function at the temperature equal to the parameter $T(\vec{r},t)$,

$$N_0\left[\omega(\vec{q}),\, T(\vec{r},t)\right] = \frac{1}{\exp\left[\dfrac{h_P\,\omega(\vec{q})}{k_B T(\vec{r},t)}\right] - 1} \tag{4-7}$$

Normal phonon-phonon scattering processes conserve the sum of the local phonon momenta, causing the distribution function to approach

$$N_{0d}\left[\omega(\vec{q}),\, \vec{v}_d(\vec{r},t),\, T(\vec{r},t)\right] = \frac{1}{\exp\left[\dfrac{h_P\left[\omega(\vec{q}) - \vec{v}_d(\vec{r},t)\bullet\vec{q}\right]}{k_B T(\vec{r},t)}\right] - 1} \tag{4-8}$$

at a rate determined by the relaxation time $\tau_N$. The local drift velocity $\vec{v}_d(\vec{r},t)$ is the vectorial sum of all phonon velocities at the location $\vec{r}$ and time $t$, is reduced by resistive scattering, and is zero in equilibrium or when $\tau_R << \tau_N$. Note that the net energy flux, Eq. (4-3), can

be nonzero even if the drift velocity is zero. The error resulting from using the relaxation-time approximation increases as the system departs from equilibrium, but has not been quantified.

### 4.2.3 Local Equilibrium Distribution Function

The local equilibrium distribution, $N_0\left[\omega(\vec{q}),\, T(\vec{r},t)\right]$, to be employed in the relaxation-time approximation, Eq. (4-6), is completely specified by $T(\vec{r},t)$. The correct value of $T(\vec{r},t)$ is that which makes the relaxation-time approximation satisfy energy conservation, Eq. (4-5). Substituting Eq. (4-6) into Eq. (4-5) yields the defining equation of $T(\vec{r},t)$,

$$\frac{1}{V_0}\sum_{\text{all } \vec{q} \text{ in } V_0} h_P\,\omega(\vec{q})\left[\frac{N_0\left[\omega(\vec{q}),\,T(\vec{r},t)\right]-N(\vec{q},\vec{r},t)}{\tau_R\left[\omega(\vec{q}),\,T(\vec{r},t)\right]}+\frac{N_{0d}\left[\omega(\vec{q}),\,\vec{v}_d(\vec{r},t),\,T(\vec{r},t)\right]-N(\vec{q},\vec{r},t)}{\tau_N\left[\omega(\vec{q}),\,T(\vec{r},t)\right]}\right]=\dot{u}_g(\vec{r},t) \qquad (4\text{-}9)$$

For dielectrics, the right-hand side is zero. If a value of $T(\vec{r},t)$ exists which satisfies Eq. (4-9), it may be obtained from the local distribution function, the drift velocity, the elastic properties of the solid, which determine the available wavevectors, the functions $\tau_R\left[\omega(\vec{q}),\,T(\vec{r},t)\right]$ and $\tau_N\left[\omega(\vec{q}),\,T(\vec{r},t)\right]$, and Eqs. (4-7) and (4-8). It is not known whether a value of $T(\vec{r},t)$ which satisfies Eq. (4-9) may always be found.

Equation (4-9) may be simplified under certain conditions. Define the net relaxation time

$$\tau\left[\omega(\vec{q}),\,T(\vec{r},t)\right]=\left[\frac{1}{\tau_R\left[\omega(\vec{q}),\,T(\vec{r},t)\right]}+\frac{1}{\tau_N\left[\omega(\vec{q}),\,T(\vec{r},t)\right]}\right]^{-1} \qquad (4\text{-}10)$$

If the drift velocity is zero, then $N_0[\omega(\vec{q}), T(\vec{r}, t)]$ and $N_{0d}[\omega(\vec{q}), \vec{v}_d(\vec{r}, t), T(\vec{r}, t)]$ are equal for each mode. If, in addition, $\tau[\omega(\vec{q}), T(\vec{r}, t)]$ is independent of the phonon frequency and $\dot{u}_g(\vec{r}, t) = 0$, multiplication of both sides of Eq. (4-9) by $\tau[\omega(\vec{q}), T_\tau(\vec{r}, t)]$ and adding $u(\vec{r}, t)$ to both sides yields

$$\frac{1}{V_0} \sum_{\text{all } \vec{q} \text{ in } V_0} h_P\, \omega(\vec{q})\, N_0[\omega(\vec{q}), T(\vec{r}, t)]$$

$$= \frac{1}{V_0} \sum_{\text{all } \vec{q} \text{ in } V_0} h_P\, \omega(\vec{q})\, N(\vec{q}, \vec{r}, t) = u(\vec{r}, t) \tag{4-11}$$

These approximations may be appropriate for some processes in dielectrics above room temperature, where phonons are the only energy carriers and the drift velocity is strongly reduced by phonon-phonon Umklapp scattering. Equation (4-11) states that $T(\vec{r}, t)$ is uniquely related to the local energy per unit volume, $u(\vec{r}, t)$. This is illustrated in Fig. 4-1, which shows an energy-entropy diagram (Gyftopoulos and Beretta, 1991) for a phonon system. The equilibrium states of the phonon system lie on the curve, whose slope is the thermodynamic temperature. During net energy transport, the phonon system occupies one of the nonequilibrium states. When Eq. (4-11) is valid, the value of $T(\vec{r}, t)$ which satisfies Eq. (4-10) in a nonequilibrium state is the thermodynamic temperature of the equilibrium state with the same energy per unit volume.

## 4.3 Solutions to the Peierls-Boltzmann Equation

This section reviews existing methods for calculating phonon transport using the Peierls-Boltzmann equation. The first subsection briefly discusses second sound. The second subsection reviews the Fourier equation, the hyperbolic heat equation, and the nonlocal theory of heat conduction, indicating that each employs an approximate form of the left of Eq. (4-1) which renders it invalid for processes with small time- and

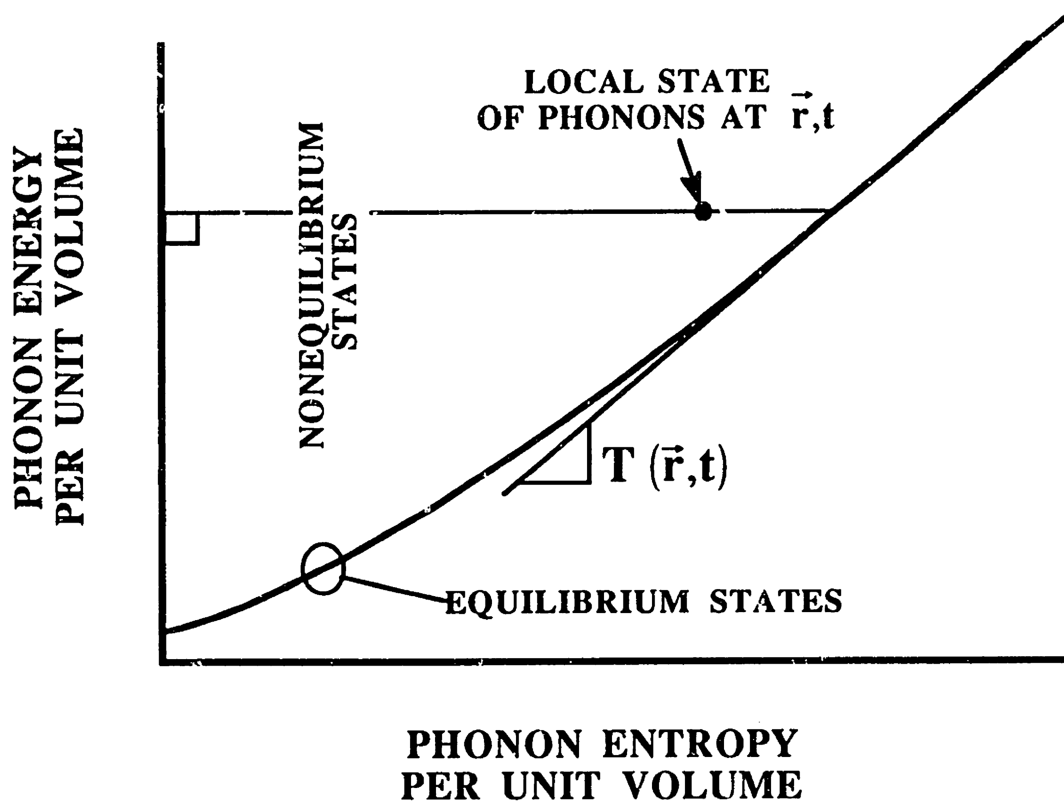


Fig. 4-1 Phonon energy-entropy diagram depicting Eq. (4-11). Note that this recipe for determining $T(\vec{r}, t)$ is only exact under the conditions discussed preceding Eq. (4-11).

lengthscales. The second subsection discusses the technique of Majumdar (1991), which has been proposed for these processes.

### 4.3.1 Second Sound

If the rate of resistive scattering is very small compared to that of normal scattering, which may occur below 20 K in nearly perfect crystals, and if a disturbance in temperature small compared to the absolute temperature is applied, a linearized form of Eqs. (4-1) and (4-6) may be solved with the energy equation, Eq. (4-4). Because normal processes conserve the phonon momentum, a local disturbance in the temperature propagates without attenuation at a velocity near $v_s / \sqrt{3}$, where $v_s$ is the speed of sound. This phenomenon is called second sound. The existence of second sound in solids was confirmed by experimental heat pulse propagation data in a Na[illegible] crystal at 14 K and 19 K (Beck, 1975).

### 4.3.2 The Fourier Equation, the Hyperbolic Heat Equation, and the Nonlocal Theory of Conduction

When resistive scattering is significant, the drift velocity is often assumed to be zero, and the net relaxation time is employed, Eq. (4-10). A more rigorous formula for $\tau[\omega(\vec{q}), T(\vec{r}, t)]$ which accounts for a nonzero drift velocity was given for the case of steady-state conduction by Callaway (1959). Equations (4-1) and (4-6) can be further simplified by employing the Debye model for phonons (Kittel, 1986) which assumes a linear dispersion relation $\omega = v_s |\vec{q}|$, a maximum phonon frequency $\omega_D$, and yields a phonon velocity $\vec{v}(\vec{q}) = v_s \hat{n}$, where $\hat{n}$ is the unit vector in the direction of $\vec{q}$. The use of the Debye model limits this approach to isotropic solids. The frequency $\omega$ and direction $\hat{n}$ now specify the phonon mode. Equations (4-1) and (4-6) reduce to

$$\frac{\partial N(\omega, \hat{n}, \vec{r}, t)}{\partial t} + v_s \hat{n} \cdot \nabla N(\omega, \hat{n}, \vec{r}, t) = \frac{N_0[\omega, T(\vec{r}, t)] - N(\omega, \hat{n}, \vec{r}, t)}{\tau[\omega, T(\vec{r}, t)]} \qquad (4\text{-}12)$$

The differences between techniques for calculating phonon energy transport are clarified by defining

$$N_{DE}(\omega, \hat{n}, \vec{r}, t) = N(\omega, \hat{n}, \vec{r}, t) - N_0[\omega, T(\vec{r}, t)] \tag{4-13}$$

which is the departure of the value of the distribution function for a given mode from the equilibrium value. Using this variable and the chain rule to expand the derivatives in time and space of $N_0[\omega, T(\vec{r}, t)]$, Eq. (4-12) becomes

$$\frac{\partial N_0[\omega, T(\vec{r}, t)]}{\partial T} \frac{\partial T(\vec{r}, t)}{\partial t} + \frac{\partial N_{DE}(\omega, \hat{n}, \vec{r}, t)}{\partial t}$$
$$+ \frac{\partial N_0[\omega, T(\vec{r}, t)]}{\partial T} v_s \hat{n} \bullet \nabla T(\vec{r}, t) + v_s \hat{n} \bullet \nabla N_{DE}(\omega, \hat{n}, \vec{r}, t) \tag{4-14}$$
$$= - \frac{N_{DE}(\omega, \hat{n}, \vec{r}, t)}{\tau[\omega, T(\vec{r}, t)]}$$

Previous numerical calculations of transient phonon transport in solids neglected either the second term, or the fourth term, or both the second and the fourth terms in Eq. (4-14). These simplifications allowed the local energy flux to be related to $T(\vec{r}, t)$, and the resulting expression was solved simultaneously with Eq. (4-4) using

$$\frac{\partial u(\vec{r}, t)}{\partial t} = C_s[T(\vec{r}, t)] \frac{\partial T(\vec{r}, t)}{\partial t} \tag{4-15}$$

where $C_s[T(\vec{r}, t)]$ is the phonon specific heat at constant volume per unit volume of the equilibrium state with temperature equal to $T(\vec{r}, t)$. Note that if Eq. (4-11) is satisfied, i.e., if the energy of the nonequilibrium state is equal to the energy of the equilibrium state with temperature equal to $T(\vec{r}, t)$, then Eq. (4-15) is exactly correct. Otherwise, the validity of this substitution is not guaranteed. A simple scaling analysis of Eq. (4-14) to estimate the

importance of the second and fourth terms is not possible because the energy flux combines solutions to Eq. (4-14) for all modes. But approximate criteria indicating when these terms may *not* be neglected can be established by examining existing solutions.

The first technique employs the Fourier law for the energy flux, $\vec{J}_E(\vec{r}, t) = - k\left[T(\vec{r}, t)\right] \nabla T(\vec{r}, t)$, where $k\left[T(\vec{r}, t)\right]$ is the thermal conductivity. To obtain the Fourier law from Eq. (4-14), the second and fourth terms are neglected, allowing the explicit solution for $N_{DE}(\omega, \hat{n}, \vec{r}, t)$ in terms of $T(\vec{r}, t)$ and known quantities. Equations (4-13) and (4-3) yield the Fourier law. For the case of a frequency-independent relaxation time, $\tau\left[\omega, T(\vec{r}, t)\right] = \tau\left[T(\vec{r}, t)\right]$, the resulting conductivity is

$$k\left[T(\vec{r}, t)\right] = \frac{1}{3}(v_s)^2 C_s\left[T(\vec{r}, t)\right] \tau\left[T(\vec{r}, t)\right] \tag{4-16}$$

This is identical to Eq. (2-1) if the mean free path is substituted for $v_s\, \tau\left[T(\vec{r}, t)\right]$. Kittel (1949; 1986) used Eq. (4-16), with a different numerical constant, and specific heat and thermal conductivity data to show that the mean free path near room temperature in most amorphous dielectrics is a few Angstroms. For a frequency-dependent relaxation time, the thermal conductivity is calculated using the frequency-dependent phonon specific heat function at constant volume per unit volume $C_s\left[x_\omega, T(\vec{r}, t)\right]$ (Berman, 1976),

$$k\left[T(\vec{r}, t)\right] = \frac{1}{3}(v_s)^2 \int_0^{\frac{\theta}{T(\vec{r}, t)}} C_s\left[x_\omega, T(\vec{r}, t)\right] \tau\left[x_\omega, T(\vec{r}, t)\right] \mathrm{d}x_\omega \tag{4-17}$$

where $x_\omega = h\omega / (k_B T(\vec{r}, t))$ and $\theta$ is the Debye temperature, and $k_B = 1.38 \times 10^{-23}$ J K$^{-1}$ is the Boltzmann constant. The frequency-dependent phonon specific heat function is

$$\begin{aligned} C_s\left[x_\omega, T(\vec{r}, t)\right] &= \frac{3(k_B)^4\left[T(\vec{r}, t)\right]^3}{2\pi^2 (h_P\, v_s)^3} \frac{(x_\omega)^4 \exp(x_\omega)}{\left[\exp(x_\omega) - 1\right]^2} \\ &= 9 N_a k_B \left(\frac{T(\vec{r}, t)}{\theta}\right)^3 \frac{(x_\omega)^4 \exp(x_\omega)}{\left[\exp(x_\omega) - 1\right]^2} \end{aligned} \tag{4-18}$$

where $N_a$ is the atomic number density. Callaway (1959) calculated the thermal conductivity in this manner for the case of a frequency-dependent relaxation time. His expression for the thermal conductivity employs two adjustable parameters in the function $\tau[\omega, T(\vec{r}, t)]$, and fits experimental data for Ge within 30 percent between 3 K and 100 K.

A second class of solutions neglects the fourth term of Eq. (4-14), but retains the second term. For $\tau[\omega, T(\vec{r}, t)] = \tau[T(\vec{r}, t)]$, Tavernier (1962) showed that Eq. (4-14) without the fourth term yields the following expression for the energy flux,

$$\vec{J}_E(\vec{r}, t) = -k[T(\vec{r}, t)]\,\nabla T(\vec{r}, t) - \tau[T(\vec{r}, t)]\frac{\partial \vec{J}(\vec{r}, t)}{\partial t} \tag{4-19}$$

The hyperbolic energy equation can be derived from Eq. (4-19) (Joseph and Preziosi, 1989; 1990). Solutions to this equation differ significantly from those to the energy equation based on the Fourier law if the transport process is microscale in time (Vedavarz et al., 1991), i.e., the timescale of the process, such as the temporal duration of a laser pulse, is comparable to or smaller than the relaxation time.

A third approach is to solve Eq. (4-14) in the steady state with the third and fourth terms. This is identical to solving the equation neglecting only the second term, because the first term does not contribute to the net energy flux. The resulting energy flux depends on the geometry of the medium and the location, as well as on $T(\vec{r}, t)$. It differs significantly from the Fourier law only for processes which are microscale in space, i.e., which possess a geometric lengthscale, such as a dimension of the medium, comparable to or smaller than the phonon mean free path $v_s\tau[T(\vec{r}, t)]$. The use of this energy flux in a transient energy equation governing $T(\vec{r}, t)$ was called the nonlocal theory of energy transport by Claro and Mahan (1989).

A solution of the complete Eq. (4-14) is not available The following conclusions can be drawn from this review: (a) The energy balance based on the Fourier equation fails for processes which are microscale in either time or in space, (b) the nonlocal theory of energy transport fails for processes which are microscale in time, and, as observed by

Majumdar (1991), (c) the hyperbolic energy equation fails for processes which are microscale in space.

### 4.3.3 Technique of Majumdar (1991)

Majumdar (1991) proposed an approximate technique for solving the complete Eq. (4-14) which defines the value of the equilibrium number of phonons in a mode as the average number of phonons in all modes having the same frequency at that location. The equilibrium distribution $N_0\left[\omega, T\left(\vec{r}, t\right)\right]$ in Eq. (4-12) is replaced by an expression which depends on $\omega$, $\vec{r}$, and $t$, and is the average value of the distribution function for a given $\omega$ over all directions $\hat{n}$. This yields the following transport equation,

$$\frac{\partial N(\omega, \hat{n}, \vec{r}, t)}{\partial t} + v_s \hat{n} \cdot \nabla N(\omega, \hat{n}, \vec{r}, t) = \frac{\int_{4\pi} N(\omega, \hat{n}, \vec{r}, t)\frac{d\Omega}{4\pi} - N(\omega, \hat{n}, \vec{r}, t)}{\tau\left[\omega, T\left(\vec{r}, t\right)\right]} \tag{4-20}$$

where $d\Omega$ is the differential solid angle. The set of the equilibrium numbers of phonons in each of the modes at a given location and time employed by Eq. (4-20) is not necessarily a Planck equilibrium distribution function, given by Eq. (4-7). Therefore, this is not an exact technique for solving the Peierls-Boltzmann equation in the relaxation-time approximation. The sum of the approximate collision integral in Eq. (4-20) over all modes possessing a given frequency $\omega$ at a given location and time is zero. As a result, the satisfaction of energy conservation, Eq. (4-5), is guaranteed by the conservation of energy within each phonon frequency $\omega$. This approach neglects the transfer of phonon energy between modes with different frequencies, and therefore makes an error when it is used to predict phonon *distribution functions*. The impact of this error on the prediction of *energy transport* is not clear. Neglecting energy transfer between modes may yield an estimate of

the steady-state radiation energy flux in a non-gray medium (Brewster, 1992). This is a promising, approximate technique whose accuracy needs to be experimentally determined.

Although Eq. (4-20) should not be used to predict phonon distribution functions when energy exchange between phonon modes of different frequencies is appreciable, it may be the best technique available for a very special regime of phonon transport. Define $\tau_s$ as the characteristic relaxation time for phonon-phonon normal and Umklapp scattering, $\tau_d$ as the characteristic relaxation time for phonon scattering on defects, and $\Delta t$ as the characteristic timescale of the transport process. If $\tau_d \leq \Delta t << \tau_s$ holds, there is significant scattering of phonons by defects, but the exchange of energy between phonons may be negligibly small because few phonons have enough time to scatter on other phonons. For a steady-state process, such as steady-state transport normal to a layer, an analogous situation may occur if $v_s \tau_d \leq \Delta x << v_s \tau_s$ holds, where $\Delta x$ is the characteristic lengthscale of the process, such as the layer thickness. Transport processes in this regime may include those in amorphous materials at low temperatures, whose analysis is important for the design of cryogenic silicon-on-insulator electronic circuits.

## 4.4 Summary and Recommendations

Microelectronic structures experience thermal conduction processes which are microscale in space, such as those in a 200 Å thick quantum-well laser, and microscale in time, such as those in the channel of a transistor operating at 77 K and experiencing 100 ps pulses of current. The validity of tools for analyzing these processes is summarized in Table 4-1. For processes which are microscale in both space and time, the technique proposed by Majumdar (1991) is the only one available. Before these tools can be applied with confidence to processes in integrated circuits, they must be tested experimentally. The assumption used by Majumdar (1991), that phonon modes of different frequencies act independently, must be investigated. It is possible that this may render the technique invalid in regimes where phonon-phonon scattering dominates, e.g., in crystals above

Table 4-1 Summary of the validity of techniques for analyzing microscale phonon conduction processes.

| | Microscale in Time Only, $\Delta t \leq \tau$, $\Delta x >> v_s \tau$ | Microscale in Space Only, $\Delta t >> \tau$, $\Delta x \leq v_s \tau$ | Microscale in Time and Space, $\Delta t \leq \tau$, $\Delta x \leq v_s \tau$ |
|---|---|---|---|
| **Fourier Equation** | No | No | No |
| **Hyperbolic Equation** | Yes | No | No |
| **Nonlocal Theory** | No | Yes | No |
| **Majumdar (1991)** | Yes | Yes | Yes |

room temperature. This assumption is less problematic in amorphous materials, where phonon-defect scattering dominates, and is employed in Section 5.2 to determine the effect of phonon-boundary scattering on conduction in amorphous layers. As was recently observed by Tien and Chen (1992), the application of any of the techniques in Table 4-1 is questionable when the wavelength of a significant fraction of the phonons is comparable to the dimensions of the conducting medium. When this is the case, the Boltzmann equation is not strictly valid, and it may be necessary to solve the Schrödinger equation to determine the rate of energy transport. This is an outstanding problem in small-lengthscale heat transfer.

# 5. PREDICTION AND MEASUREMENT OF THE THERMAL CONDUCTIVITY OF AMORPHOUS DIELECTRIC LAYERS

## 5.1 Introduction

The performance and reliability of transistors and interconnects are affected by temperature fields in circuits. Layers of amorphous dielectric materials, e.g., silicon dioxide and silicon nitride, electrically insulate circuit components and protect them from corrosion. These layers have very low thermal conductivities, near 1 W m$^{-1}$ K$^{-1}$ at room temperature. Conduction along the layers is not important due to the much higher thermal conductivities of the bounding semiconducting and metal layers, but conduction *normal* to the layers can be an important obstacle to the cooling of devices and interconnects. Energy dissipated in aluminum interconnects, for example, must travel through a silicon dioxide layer between 0.5 and 1.0 μm thick to reach the substrate heat sink. In silicon-on-insulator (SOI) circuits, devices are separated from the substrate by a silicon-dioxide layer approximately 0.4 μm thick. To predict the median time to failure of an interconnect or the drain current of a SOI field-effect transistor, both of which depend on the temperature field, the thermal conductivity for conduction normal to amorphous layers is needed.

Data for the thermal conductivity of bulk amorphous dielectrics vary little among different samples (Berman, 1976). In contrast, Fig. 5-1 shows that the effective thermal conductivity for conduction normal to amorphous dielectric layers, $k_{n,eff}$, depends on the layer thickness and can be an order of magnitude less than the conductivity measured in bulk samples, $k_{bulk}$. The conductivity $k_{n,eff}$ is defined by Eq. (3-2) to account for the

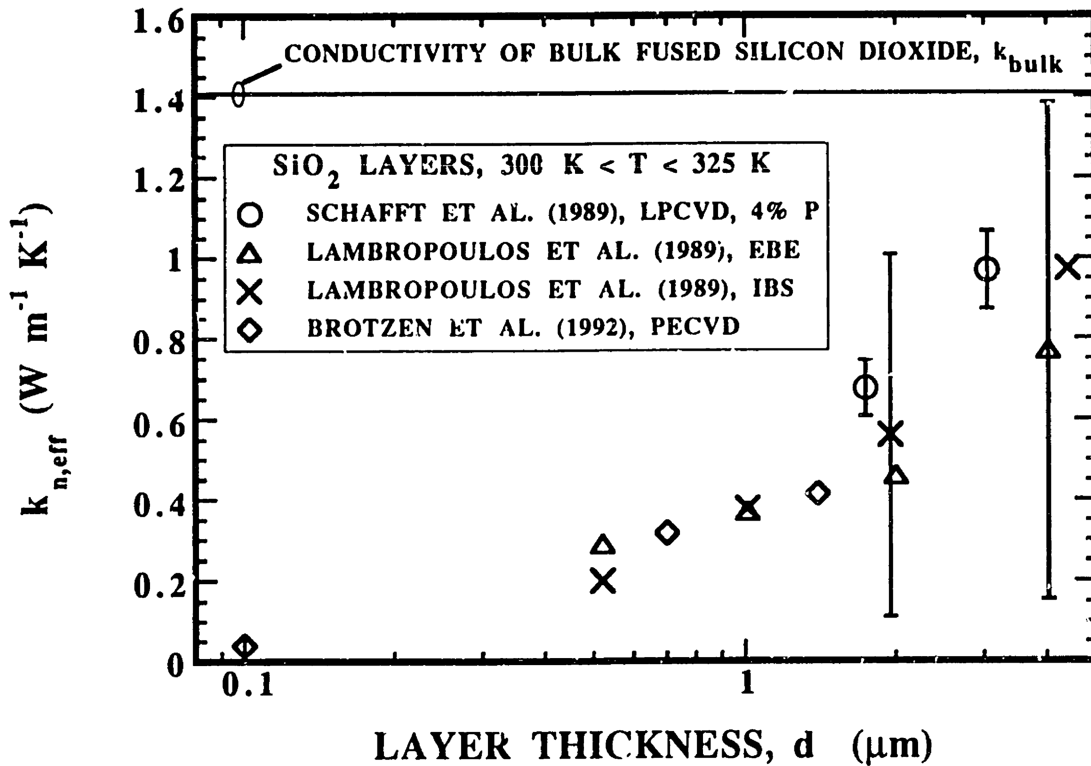


Fig. 5-1 Previous data for the effective thermal conductivity for conduction normal to silicon dioxide layers, $k_{n,eff}$. The acronyms in the legend indicate the fabrication techniques, whose full names are given in Table 5-1. The layers of Schafft et al. (1989) contained 4 mass percent of Phosphorus atoms. The bulk conductivity $k_{bulk}$ was measured by Sugawara (1969).

thermal resistance due to the layer boundaries. Analysis of the data in Fig. 5-1 is complicated because different experimental methods were used, with often very large or unknown uncertainties, and the layers were fabricated using different techniques. This is summarized in Table 5-1. The difference between $k_{n,eff}$ and $k_{bulk}$ has been attributed to three phenomena: (a) Schafft et al. (1989) indicated qualitatively that the boundary scattering of phonons may be responsible. (b) A microstructure or stoichiometry in the layers different than in the bulk could make $k_{n,eff}$ smaller than $k_{bulk}$. The conductivity $k_{n,eff}$ would be thickness dependent if the microstructure or stoichiometry changed near the layer boundaries. (c) A thermal boundary resistance would cause $k_{n,eff}$ to decrease with

Table 5-1 Summary of the data in Fig. 5-1. The relative uncertainty in the measurement of $k_{n,eff}$ is $U(k_{n,eff})$. The measurement techniques are reviewed on the indicated pages in Section 3.3.1.

| **Authors** | **Layer Fabrication Technique** | **Measurement Technique** | $U(k_{n,eff})$ |
|---|---|---|---|
| Schafft et al. (1989) | low-pressure chemical-vapor deposition (LPCVD) with 4 mass-percent Phosphorus | microfabricated test structure (see pp. 66 - 67) | 10 % |
| Lambropoulos et al. (1989) | electron-beam evaporation (EBE) | thermal comparator (see pp. 68 - 70) | 80 % |
| Lambropoulos et al. (1989) | ion-beam sputtering (IBS) | thermal comparator | 80 % |
| Brotzen et al. (1992) | plasma-enhanced chemical-vapor deposition (PECVD) | microfabricated test structure (see pp. 66 - 67) | not determined |

decreasing layer thickness. This would be indistinguishable from the highly-resistive interfacial layers proposed by Brotzen et al. (1992), so these two mechanisms are grouped together.

This chapter makes progress towards resolving the puzzle by investigating two of these hypotheses, and by measuring $k_{n,eff}$ in layers fabricated using different processing techniques. Section 5.2 determines the effect of (a) phonon-boundary scattering on $k_{n,eff}$, and Section 5.3 investigates hypothesis (b) by showing how the porosity of low-pressure chemical-vapor deposited (LPCVD) layers, which may depend on their annealing temperature, can reduce $k_{n,eff}$. Section 5.4 develops a steady-state technique for measuring $k_{n,eff}$ based on that of Cahill et al. (1989) and determines the experimental uncertainty. Section 5.5.1 compares the predictions of the boundary-scattering analysis with data for silicon-dioxide layers fabricated using the SIMOX process, i.e., separation by implantation with oxygen. The substrates for silicon-on-insulator (SOI) circuits are made using the SIMOX process, so these measurements help determine temperature fields in SOI circuits in Chapter 6. Section 5.5.2 compares data for LPCVD silicon-dioxide layers which are annealed at different temperatures with the predictions of the model accounting for porosity.

## 5.2 Phonon-Boundary Scattering

Chapter 2 shows that boundary-scattering analysis in a layer begins with a microscopic look at conduction in the bulk material, in this case amorphous silicon dioxide. Research on thermal conduction in amorphous materials was reviewed by Zaitlin and Anderson (1975), Berman (1976), and Freeman and Anderson (1986b). Thermal conduction in amorphous materials is governed by their microstructure, a subject reviewed by Bartenev (1970) and Ziman (1979). Kittel (1949; 1986) explained the temperature dependence of the thermal conductivity in amorphous materials by defining a lengthscale of disorder comparable to the lattice constant of the material in crystalline form. Figure 5-2

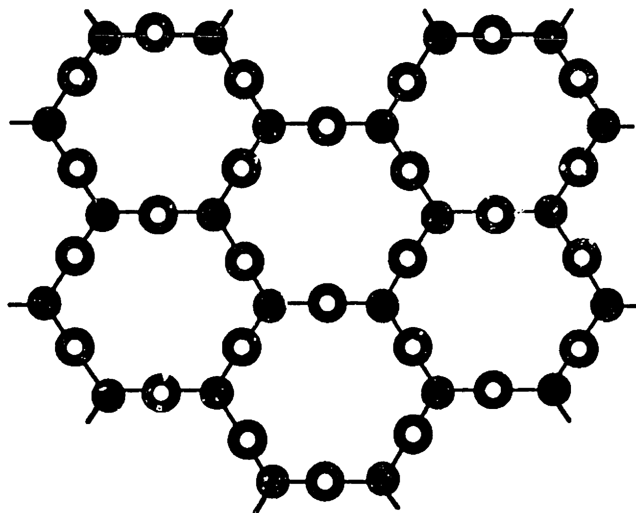


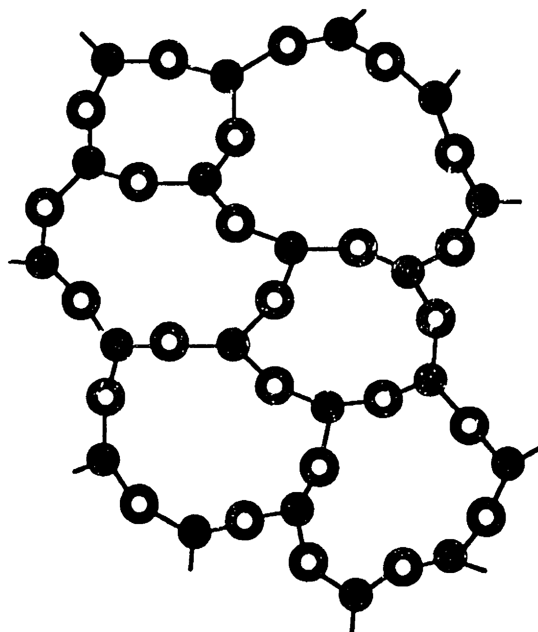




Fig. 5-2 Two-dimensional analogs of crystalline and amorphous $Al_2O_3$ (after Zachariasen, 1932).

shows the difference between the periodic structure of a crystal and the random network of atoms in an amorphous material for two-dimensional analogs of sapphire. Phonons of wavelength small compared to this disorder lengthscale are scattered strongly by the disorder and have mean free paths of a few Angstroms. Phonons of wavelength long compared to this lengthscale have mean free paths which increase rapidly with the wavelength. This is analogous to the Rayleigh scattering of radiation on particles small compared to the radiation wavelength, where the photon mean free path is proportional to the fourth power of the wavelength (Bohren and Huffman, 1983).

Studies of phonon-boundary scattering in amorphous layers were for low temperatures, where the long-wavelength, long-free-path phonons dominate conduction. Matsumoto et al. (1977) showed that the boundary scattering of long-wavelength phonons strongly reduces $k_{n,eff}$ of epoxy layers with thicknesses between 1 and 10 μm below 10 K. But Zaitlin et al. (1975) observed no effect of boundary scattering on the thermal conductivity along 2.9 to 71 μm thick mylar and glass layers below 10 K. This was attributed to the specular reflection of phonons at the layer boundaries, which reduces conduction normal to a layer but does not affect conduction along a layer. At higher temperatures, from 77 K to 300 K, the long-wavelength phonons constitute a small fraction of the energy in the material, but may contribute significantly to conduction because of their relatively long mean free paths (Freeman and Anderson, 1986b). The boundary scattering of these phonons may be responsible for the low values of $k_{n,eff}$ measured in amorphous dielectric layers.

This section predicts the influence of boundary scattering on $k_{n,eff}$ of amorphous layers above 10 K. The frequency dependence of phonon mean free paths in bulk amorphous silicon dioxide is determined using sound-attenuation data, Rayleigh scattering theory, and the model of Kittel (1949). The effective conductivity considering boundary scattering is calculated using the approximate expressions of Matsumoto et al. (1977) and Chen and Tien (1992).

### 5.2.1 Effective Conductivity Considering Boundary Scattering

The kinetic formula for the conductivity of dielectrics is given in Section 2.2,

$$k = \frac{1}{3} C_s \, v_s \, \Lambda_s \tag{5-1}$$

where $C_s$ is the phonon specific heat per unit volume and $v_s$ is the speed of sound. Equation (5-1) defines the phonon mean free path $\Lambda_s$ *accounting for phonons of all frequencies*, and is used to construct the regime maps in Chapter 2. This section introduces the *frequency-dependent* phonon mean free path, $\Lambda_\omega$, the mean distance phonons of a given frequency, or energy, travel between collisions. The use of the phonon mean free path $\Lambda_s$ or the analogous electron mean free path $\Lambda_e$, defined by Eq. (2-1), neglects the energy dependence of the carrier free paths. This approximation has been used with reasonable success to analyze electron-boundary scattering (Tien et al., 1969; Flik and Tien, 1990; Kumar and Vradis, 1991), since electrons contributing to net transport all possess nearly the same energy. But in dielectrics, where phonons of energies varying by several orders of magnitude contribute to conduction, $\Lambda_s$ must be used with care.

This was demonstrated by Savvides and Goldsmid (1972), who observed boundary-scattering effects on the phonon conductivity in silicon crystals of dimensions orders of magnitude larger than $\Lambda_s$. The crystals had been irradiated with neutrons, introducing point defects which cause the Rayleigh scattering of phonons. Kittel (1949; 1986) used Eq. (5-1) and specific heat and thermal conductivity data to show that near room temperature in most amorphous materials, $\Lambda_s$ is independent of temperature and equal to a few Angstroms. This is much smaller than the thicknesses of most practically-used layers, suggesting that boundary scattering is not important. But an accurate boundary-scattering analysis for amorphous materials must account for the strong frequency dependence of $\Lambda_\omega$ in these materials, which is similar to that in neutron-irradiated crystals.

Equation (5-1) can be written as an integral over all phonon angular frequencies $\omega$, but this requires a model for the phonon density of states. The Debye model for the phonon density of states (Kittel, 1986), although derived for a crystal, remains the most accurate available (Freeman and Anderson, 1986b). While it may be in error for phonons of wavelength comparable to the lengthscale of disorder, it is a very good approximation for the much-longer-wavelength phonons which experience significant boundary scattering. Equation (4-17) applies in this case, written here using $\Lambda_\omega = v_s\, \tau$,

$$k = \frac{1}{3} v_s \int_0^{\frac{\theta}{T}} C_s[x_\omega, T]\; \Lambda_\omega[x_\omega, T]\, \mathrm{d}x_\omega \tag{5-2}$$

The Debye model constants for amorphous silicon dioxide are $\theta = 492$ K, $v_s = 4100$ m s$^{-1}$, and $N_a = 6.62 \times 10^{28}$ m$^{-3}$ (Stephens, 1973). The Debye angular frequency, which is used later, is $\omega_D = k_B\theta/h_P = 6.441 \times 10^{13}$ rad s$^{-1}$.

If the material is bulk, i.e., has no boundaries, then $\Lambda_\omega$ is the bulk mean free path, $\Lambda_{\omega,bulk}$. Callaway (1959) and Holland (1963) accounted for boundary scattering using a frequency-independent mean free bath for boundary scattering, $\Lambda_{s,b} = B\, d$, where $B$ is a dimensionless constant not too far from unity and $d$ is the smallest specimen dimension, e.g., the layer thickness. Matthiessen's rule (Ziman, 1960) yields

$$\frac{1}{\Lambda_\omega} = \frac{1}{\Lambda_{\omega,bulk}} + \frac{1}{\Lambda_{s,b}} = \frac{1}{\Lambda_{\omega,bulk}} + \frac{1}{B\, d} \tag{5-3}$$

Matsumoto et al. (1977) used Eqs. (5-2) and (5-3) to calculate the $k_{n,eff}$ for epoxy layers below 10 K. They assumed a frequency and temperature dependence for $\Lambda_{\omega,bulk}$ and fitted bulk epoxy thermal conductivity data using $d = \infty$, i.e., $\Lambda_\omega = \Lambda_{\omega,bulk}$. The predicted

temperature dependence of $k_{n,eff}$ agreed well with data for layers when $B$ was used as an adjustable parameter.

The nature of phonon reflection and transmission at the boundaries depends on the ratio of the phonon wavelength to the standard deviation of the boundary profile (Ziman, 1960). When this ratio is near or smaller than unity, the phonons are reflected and transmitted diffusely. At room temperature, phonons with wavelengths from a few Angstroms to a few tens of nanometers contribute to energy transport. The shortest wavelength phonons, which carry most of the energy, are diffusely reflected by any practical interface. The longest wavelength phonons may not scatter diffusely on the boundaries of many interfaces. Swartz and Pohl (1989) derived the approximate diffuse mismatch model for the diffuse transmission and reflection of phonons at an interface, and showed that the boundary resistance predicted by this model is in excellent agreement with data for metal-dielectric interfaces and differs little from that predicted by the theory of Little (1959) for an ideal smooth interface. The diffuse mismatch model is much simpler than the acoustic mismatch model of Little (1959) and is used here for the transmission coefficients of phonons of all wavelengths. The error due to the non-diffuse transmission and specular reflection of long wavelength phonons at the boundaries is expected to be small, but has not been quantified.

The diffuse mismatch model assumes complete contact between the layer and the bounding media, and accounts neither for changes in microstructure near the interface, nor for interfacial layers. High-resolution transmission electron micrographs of interfaces of deposited (Schroder, 1987) and SIMOX (Celler and White, 1992) amorphous silicon dioxide layers with silicon show no evidence of incomplete contact on lengthscales down to a few Angstroms, nor of a different microstructure in the silicon near the boundary. These micrographs show only that the microstructures of the layers were not periodic up to the interface with the silicon. Two of the hypotheses discussed in Section 5.1, (b) a thickness-dependent microstructure or stoichiometry, and (c) thermal boundary resistances or

interfacial layers, are not excluded. Section 5.2 investigates (a) phonon-boundary scattering independently from (b) and (c), and assumes the microstructure and stoichiometry of the layer are those of the bulk amorphous solid up to its boundaries with the surrounding media. The diffuse mismatch model yields a good estimate of the transmission coefficients for this case. Using the speeds of sound and the theory of Swartz and Pohl (1989), the transmission coefficients from amorphous silicon dioxide into aluminum and silicon are $\alpha_0 = 0.586$ and $\alpha_1 = 0.326$, respectively.

If the diffuse mismatch model is employed at both boundaries, one-dimensional phonon conduction normal to a layer is analogous to radiation between diffuse gray walls in an absorbing medium. This problem has been solved for grey media, i.e., when the photon mean free path is independent of the photon frequency (Siegel and Howell, 1981). To estimate the energy transport for nongrey media, the solution for grey media can be integrated over all frequencies to yield Eqs. (5-2) and (5-3) with

$$B = \frac{3}{4\left(\frac{1}{\alpha_0} + \frac{1}{\alpha_1} - 1\right)} \qquad (5\text{-}4)$$

where $\alpha_0$ and $\alpha_1$ are the phonon transmission coefficients from the layer into its bounding media (Chen and Tien, 1992). This approximation assumes that phonon modes of different frequencies are independent, i.e., that they do not exchange energy. The same assumption makes possible the technique of Majumdar (1991) for solving the Peierls-Boltzmann equation, given by Eq. (4-20). As discussed in Section 4.3.3, this may yield errors in predicted phonon distribution functions. But this approach provides a good estimate of *energy* transport in nongrey media, and is the best available.

### 5.2.2 Bulk Phonon Mean Free Paths

The frequency-dependent phonon mean free path in bulk amorphous materials has not been determined. But it is known that there are three regimes of its frequency

dependence (Freeman and Anderson, 1986b). There are similarities among the expressions for $\Lambda_{\omega,bulk}$ in each of these regimes, which were used to fit bulk conductivity data from 0.1 to 100 K (Klemens, 1951; Walton, 1974; Matsumoto et al., 1977). But there is little agreement on the mechanisms yielding these functions. This section combines models for $\Lambda_{\omega,bulk}$ which are successful in each regime into a single function for all frequencies.

For the *high frequency regime*, $\omega > \sim 0.1\ \omega_D$, one of the best approaches uses a frequency-independent phonon mean free path, $\Lambda_0$ (Kittel, 1949; 1986). It is equal to $\Lambda_s$ in Eq. (5-1) calculated using thermal-conductivity and specific-heat data above 300 K, where $\Lambda_s$ is nearly independent of temperature and the phonons in this regime dominate conduction. This approach is problematic because $\Lambda_0$ is shorter than the wavelengths $\lambda_s$ of some phonons in the high frequency regime. The phonon transport equation, from which Eq. (5-2) was derived, fails for these phonons due to the uncertainty principle. A phonon with frequency $\omega$ is a packet of waves with frequencies mostly within $\Delta\omega$ of $\omega$. The uncertainty in space of this wave packet is $\Delta z = (2\pi\ v_s) / \Delta\omega$. Energy transport by a phonon is well defined only if its mean free path is much larger than its uncertainty in space, i.e., $\Lambda_{\omega,bulk} >> \Delta z$, and its energy $h_P\ \omega$ is much larger than the uncertainty in its energy, i.e., $\omega > \Delta\omega$. The uncertainty principle yields the requirement $\Lambda_{\omega,bulk} >> \lambda_s$, where $\lambda_s = (2\pi\ v_s) / \omega$. This is satisfied in crystals, but not in amorphous materials in the high frequency regime.

The failure of the transport equation may eventually be remedied by molecular-dynamics calculations (e.g., Lee et al., 1991), but these techniques need refinement. The model of Kittel (1949) is used here even when the phonon transport is not described by a transport equation because it yields the correct conductivity at high temperatures, where the high frequency excitations dominate energy transport. Since only low frequency phonons, which satisfy the above requirement because of their very long mean free paths, scatter on the layer boundaries, this work is not concerned with the subtleties of the high-frequency lattice excitations as long as their contribution to the conductivity is correct. The smallest

phonon mean free path $\Lambda_0$ is calculated using Eq. (5-1), the measured bulk thermal conductivity (Sugawara, 1969), and the measured specific heat (Touloukian and Buyco, 1970b) of amorphous silicon dioxide. The average value between 300 and 500 K is used, $\Lambda_0 = 4.94$ Å.

In the *intermediate frequency regime*, $0.01\,\omega_D < \omega < 0.1\,\omega_D$, the mechanism responsible for phonon scattering is unknown. Freeman and Anderson (1986a) closely fitted the temperature dependence of the thermal conductivity of many amorphous solids, including silicon dioxide, using Eq. (5-2) and

$$\Lambda_{\omega,D} = \frac{S_D}{\omega^4} \quad , \; S_D = 1.76 \times 10^{42} \text{ m rad}^4 \text{ s}^{-4} \tag{5-5}$$

This frequency dependence is analogous to the Rayleigh scattering of phonons on regions with different elastic properties and dimensions small compared to the wavelength (Ziman, 1960). For a region with a deviation in mass density $\delta\rho$ compared to the surrounding medium of density $\rho$, the phonon mean free path is given approximately by Eq. (5-5) and

$$S_D = \frac{144\, v_s^4}{\pi\, N_D\, a^6} \left(\frac{\delta\rho}{\rho}\right)^{-2} \tag{5-6}$$

where $N_D$ is the number density and $a$ the typical dimension of the scattering sites. The opposing limit to Rayleigh scattering is geometrical scattering for high-frequency phonons, which yields the frequency-independent mean free path $\Lambda_G = (N_D\, \pi\, a^2 / 4)^{-1}$. To determine if $\Lambda_0$ and the Rayleigh scattering are brought about by the same defects, the expression for geometrical scattering is solved with Eq. (5-6) using $\Lambda_G = \Lambda_0$ and $\delta\rho = \rho$, yielding $a = 13$ Å and $N_D = 1.53 \times 10^{27}$ m$^{-3}$. The volume of scattering sites exceeds the material volume, a difficulty remedied only if $\Lambda_G > \Lambda_0$ is used. This indicates that if Rayleigh scattering occurs, $\Lambda_0$ is not determined by the same defects.

The mean free paths of phonons in the *low frequency regime*, $\omega < 0.01\ \omega_D$, were measured through the attenuation of sound waves. Research reviewed by Hunklinger and Arnold (1976) determined that a scattering process not present in crystals limits the mean free paths of long-wavelength phonons in amorphous materials. In a crystal, one position of an atom relative to the other atoms minimizes its potential energy, and the forces on the atom always increase as it departs from this position. But in an amorphous material, there may be two or more positions for an atom which yield local minima in its potential energy. The potential-energy barrier between these two atomic positions is overcome by the interaction of the atom with high-frequency phonons. The long-wavelength phonons, shear and compression sound waves, change the potential-energy values of the local minima. The motion of atoms to the favorable position, assisted by the high-frequency phonons, is called *structural relaxation*. The structural relaxation can occur out of phase with the long-wavelength phonons and absorb their energy, particularly if the time it takes for atoms to shift their positions is comparable to the wave period. The theory for this phenomenon is similar to the Debye relaxation model which determines the influence of electric dipoles in liquids on the photon mean free path (Bohren and Huffman, 1983).

Gilroy and Phillips (1981) developed an expression which closely fitted experimental sound-attenuation data in amorphous silicon dioxide at low temperatures. Bonnet (1991) approximated their integrals for higher temperatures, yielding

$$\frac{1}{\Lambda_{\omega,SR}} = \frac{\pi\, S_{SR}\,\omega}{2\, v_s}\left[\sqrt{\pi}\,\frac{\Gamma\left(\frac{T^*}{2}+1\right)}{\Gamma\left(\frac{T^*}{2}+\frac{3}{2}\right)}\,\frac{T^*}{\cos\left(\frac{\pi}{2}T^*\right)}\left(\omega^*\right)^{T^*} - \frac{T^*}{1-T^*}\,\omega^*\right] \tag{5-7}$$

where $\Lambda_{\omega,SR}$ is the phonon mean free path limited by structural relaxation, $\omega^* = \omega\tau_0$, $T^* = k_B T / E_0$, and $\Gamma$ is the gamma function. Bonnet (1991) closely fitted the data of Vacher et al. (1981) for amorphous silicon dioxide from 10 to 300 K using $\tau_0 = 2.5 \times 10^{-13}$ s, $E_0 = 5.02 \times 10^{-21}$ J, and $S_{SR} = 1.89 \times 10^{-3}$.

In the present work, these parameters and Eq. (5-7) model phonon scattering on structural relaxation in the low frequency regime. Equation (5-5) models Rayleigh scattering in the intermediate frequency regime. The transition between the low and intermediate frequency regimes is modeled using Matthiessen's rule,

$$\frac{1}{\Lambda_{\omega,bulk}} = \frac{1}{\Lambda_{\omega,D}} + \frac{1}{\Lambda_{\omega,SR}} \tag{5-8}$$

In the high frequency regime, the model of Kittel (1949) is used, $\Lambda_{\omega,bulk} = \Lambda_0$. The transition from the intermediate to the high frequency regimes occurs at $\omega = 7.73 \times 10^{12}$ rad s$^{-1}$ = 0.12 $\omega_D$ for silicon dioxide. For $\omega \leq 0.12\ \omega_D$, the mean free path is given by Eq. (5-8). For $\omega > 0.12\ \omega_D$, the mean free path is $\Lambda_{\omega,bulk} = \Lambda_0 = 4.94$ Å.

The bulk mean free path $\Lambda_{\omega,bulk}$ developed here for silicon dioxide is graphed in Fig. 5-3, showing its three regimes. Also shown is the phonon mean free path in silicon at room temperature limited by Umklapp scattering (Holland, 1963). The room-temperature thermal conductivity of silicon is about two orders of magnitude larger than that of silicon dioxide, which is due almost entirely to the much larger mean free path of phonons. In silicon dioxide, phonons experiencing Rayleigh scattering are responsible for more of the specific heat at 77 K than at 300 K. Since these phonons have longer mean free paths than the high-frequency phonons, boundary scattering is potentially more important at 77 K than at room temperature. The use of $\Lambda_0 = \Lambda_s$ for high frequency phonons overestimates $\Lambda_0$ because Eq. (5-1) includes the contribution to the conductivity of the long-wavelength phonons. This error is small only if the contribution of phonons of frequency less than 0.12 $\omega_D$ is small compared to the total conductivity above 300 K. The curves in Fig. 5-4, calculated using Eq. (5-2), show the fractions of the total thermal conductivity at 10 K, 77 K, and 300 K brought about by phonons with frequencies less than $\omega$. The integrand in Eq. (5-2) is the product of the phonon mean free path in Fig. 5-3 and the Debye specific

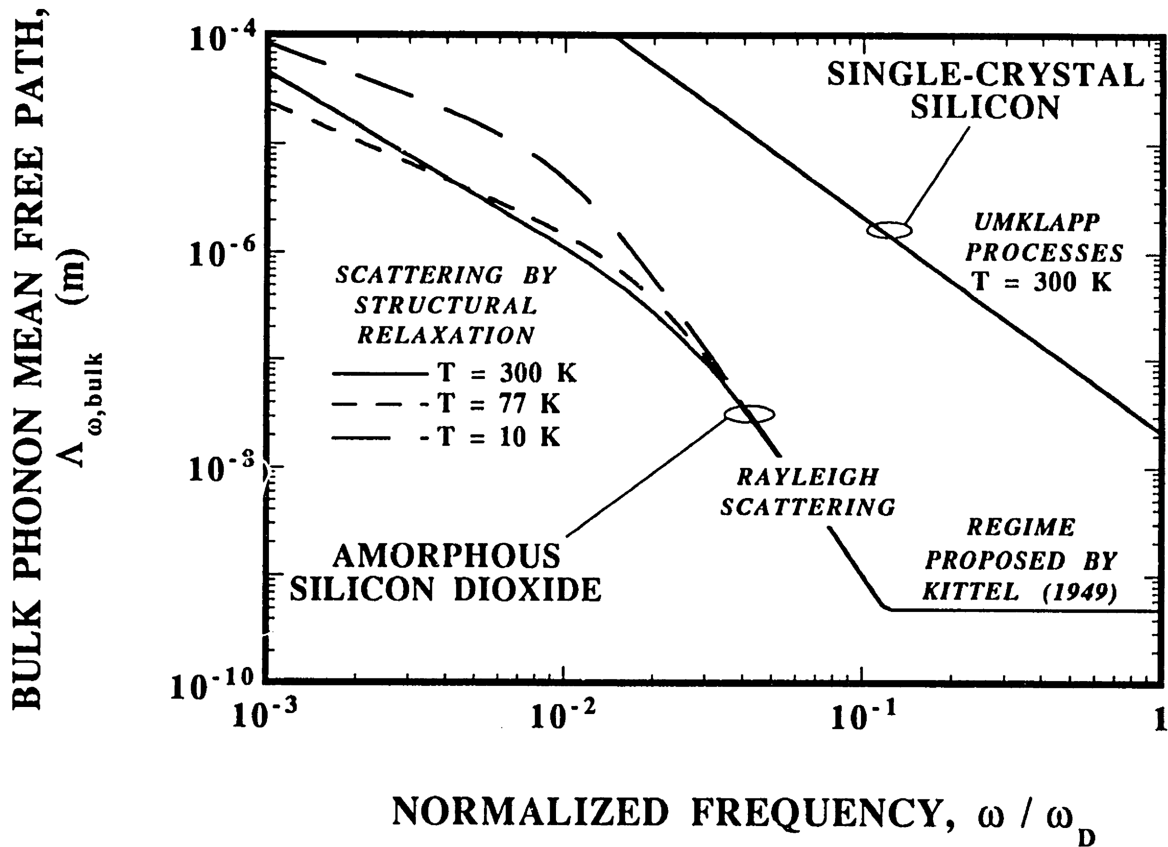


Fig. 5-3 The phonon mean free path in bulk amorphous silicon dioxide, $\Lambda_{\omega,bulk}$, showing the three regimes of its frequency dependence.

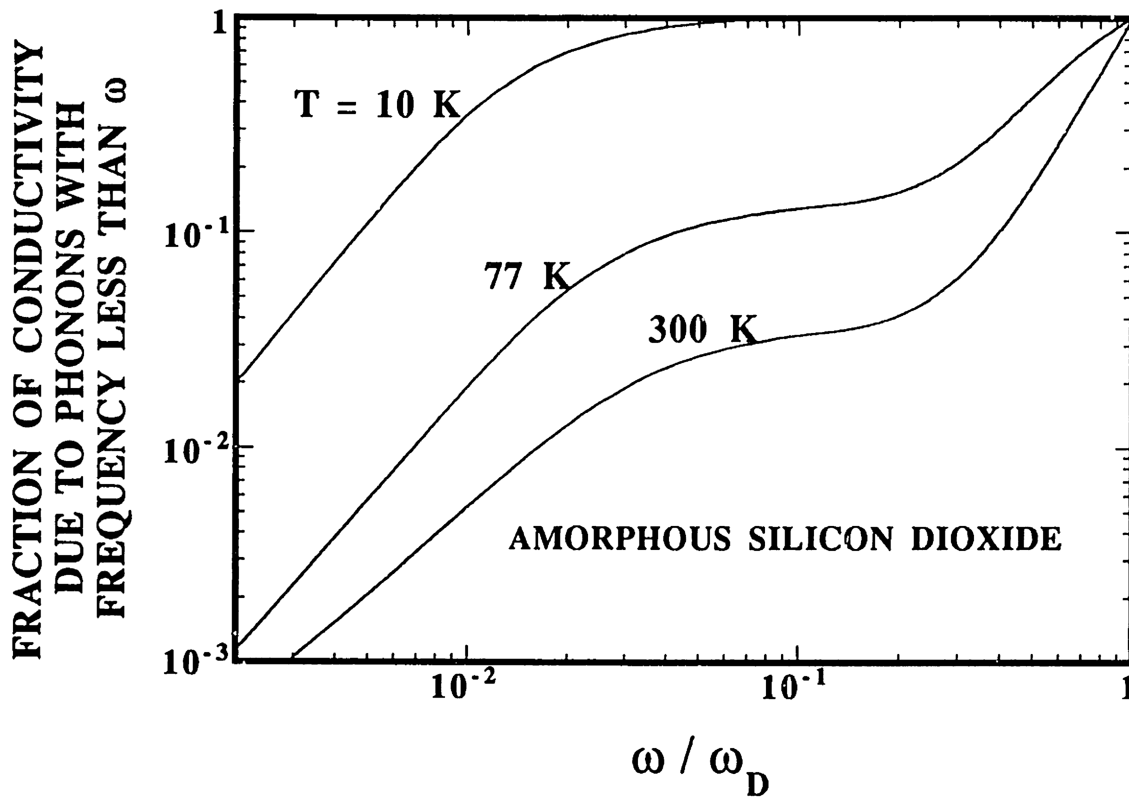


Fig. 5-4 Fraction of the conductivity due to phonons with angular frequencies less than $\omega$.

heat function, Eq. (4-18). The relative contribution of low-frequency phonons to the total specific heat increases with decreasing temperature, which increases the importance of these phonons for thermal conduction. Since the contribution of phonons of frequency greater than 0.12 $\omega_D$ to the conductivity is less than 5 percent above 300 K, the technique for obtaining $\Lambda_0$ is acceptably accurate.

The effective conductivity of silicon dioxide layers is calculated using Eqs. (5-2) - (5-5), (5-7) and (5-8). From 10 to 300 K, the conductivity predicted using $d = \infty$ differs by up to 20 percent from bulk data. This is due to the approximate Debye model for the phonon density of states. In this work, the Debye model is assumed only to predict the *relative contributions* of phonons of different frequencies to the total conductivity. This allows the calculated $k_{n,eff}$ to be normalized by the $k_{bulk}$ calculated using $d = \infty$. The final prediction for $k_{n,eff}$ is

$$k_{n,eff} = [k_{bulk}]_{measured} \times \left[\frac{k_{n,eff}}{k_{bulk}}\right]_{calculated} \qquad (5\text{-}9)$$

## 5.3 Influence of the Annealing Temperature of LPCVD Layers

The boundary-scattering analysis assumes that the microstructure and stoichiometry of the layer are identical to those of the bulk material. Section 5.5.1 shows that this may be a good approximation for SIMOX silicon-dioxide layers. But this is not a good approximation for unannealed LPCVD silicon-dioxide layers, which are shown in this section to have a mass density which depends on annealing temperature and can be up to 10 percent lower than that of bulk fused silicon dioxide. A model is developed here for the annealing-temperature dependence of $k_{n,eff}$ of LPCVD silicon dioxide layers. The first subsection discusses the conditions under which the thermal conductivity *internal* to the layer, $k_{int}$, and the total thermal boundary resistance, $R_B$, can be extracted from data for

$k_{n,eff}$. The second subsection relates $k_{int}$ to the annealing temperature by modeling the layer as a porous medium.

### 5.3.1 Resistances-in-Series Model

When analyzing data for $k_{n,eff}$, it is often useful assume that thermal resistances at the layer boundaries, $R_{B1}$ and $R_{B2}$, are in series with a volume resistance within the layer, $d/k_{int}$. The total thermal resistance is

$$R_T = \frac{d}{k_{n,eff}} = \frac{d}{k_{int}} + R_{B1} + R_{B2} = \frac{d}{k_{int}} + R_B \qquad (5\text{-}10)$$

where $R_B = R_{B1} + R_{B2}$ is the sum of the thermal resistances at both boundaries. Section 4.3.2 discusses the reasons why the Fourier equation, from which Eq. (5-10) is derived, fails for microscale processes. Equation (5-10) is only useful if conduction in the layer is macroscale, i.e., boundary scattering is not important. Section 5.5.1 shows that at room temperature, the short mean free paths of phonons in amorphous silicon dioxide make this a problem only in layers thinner than a few hundred Angstroms.

The thermal conductivity within a layer is not necessarily independent of the position in the layer. This was recently demonstrated by Graebner et al. (1992a) for CVD diamond layers, in which the grain size decreases near the substrate-layer interface. For layers where the thermal conductivity varies only with $y$, where $y$ is the distance from the substrate, $k_{int}$ is related to the local thermal conductivity $k(y)$ by

$$\frac{1}{k_{int}} = \int_0^d \frac{1}{k(y)} \frac{dy}{d} \qquad (5\text{-}11)$$

The present work applies Eq. (5-10) with the following assumption: The layer microstructure and interfacial properties which govern $k_{int}$ and $R_B$, respectively, depend on

the processing conditions, e.g., the annealing temperature, but *not* on the layer thickness. This assumes that the distance over which the boundaries influence the microstructure within the layer are small compared to the smallest layer thickness, which is about 350 Å. This allows $k_{int}$ and $R_B$ to be determined for the LPCVD layers with a given annealing temperature using data for the thickness-dependent thermal resistance and Eq. (5-10). This assumption is consistent with the dependences of $R_T$ on $d$ measured here in the LPCVD layers. It is shown in Section 5.5.2 that on a plot of $R_T$ as a function of $d$, all of the data for a given annealing temperature can be fitted within the experimental uncertainty by a line.

### 5.3.2 Model accounting for Porosity

Chemical-vapor-deposition of silicon dioxide yields layers with an amorphous microstructure (Adams, 1988). The mass density of a bulk amorphous material decreases as its temperature is increased (Bartenev, 1970). This is due in part to structural changes in the material which are facilitated by the increasing energies of the atoms, a phenomenon not present in crystals. By annealing and rapidly cooling an amorphous material, it is possible to achieve at low temperatures a level of the density which is smaller than the value resulting from slow cooling. In contrast, measurements of the room-temperature mass density of LPCVD silicon dioxide layers showed that annealing and rapid cooling in air cause this property to increase (Nagasimi, 1972; Smolinsky and Wendling, 1985). For LPCVD layers deposited near 650 K, such as those in the present study, Nagasimi (1972) showed that the density increased by an amount which increased with the annealing temperature. The largest increase was about 10 percent for a layer annealed at 1273 K. Nagasimi (1972) suggested that the lower density of the unannealed layers was due to a microstructure which was different from that of the annealed layers when observed on a lengthscale of the order of the interatomic spacing.

The present analysis is based on a different, simpler hypothesis. It is assumed that the LPCVD process introduces pores into the layers, which have characteristic dimensions

much larger than the atomic spacing. In an amorphous material, an imposed stress results in a relaxation process with a time constant which decreases rapidly with increasing temperature (Bartenev, 1970). The material flows until the stress is relieved. But when the temperature is far below the glass transition temperature, ~ 1330 K for silicon dioxide, these time constants are often too large to be observed experimentally. Pores cause stresses in the amorphous material, due both to surface tension and to buoyancy forces. The timescale for the relaxation of these stresses, which can cause the pore to move out of the layer, depends on temperature. If the LPCVD process introduces pores into the layer, it is plausible that the porosity could depend on the maximum temperature achieved for a significant length of time during the processing, $T_p$. For annealed layers, $T_p$ is the annealing temperature. For unannealed layers, $T_p$ is the deposition temperature. If $\rho_p$ is the density of the porous material and $\rho_d$ is the density of the material without pores, the data of Nagasimi (1972) are fitted within 0.5 percent by

$$\frac{\rho_p}{\rho_d} = 0.636 + 0.735\left(\frac{T_p}{T_r}\right) - 0.371\left(\frac{T_p}{T_r}\right)^2 \tag{5-12}$$

for 613 K < T < 1273 K, where $T_r$ = 1305 K. The porosity, $p$, is the volume fraction of the pores. The density of the gases within the pores is assumed to be much smaller than $\rho_d$, yielding $p = 1 - \rho_p/\rho_d$.

Thermal conduction in the porous layers is analyzed here using the Fourier equation. This approach is valid when (a) the pores are of dimension large compared to the wavelength of the phonons which carry the heat near room temperature, and (b) the pores do not significantly reduce the phonon mean free path, $\Lambda_s$. If $a$ is the characteristic pore dimension, (a) may be written as $a \gg \lambda_{s,dom}$, where $\lambda_{s,dom}$ is the dominant phonon wavelength (Ziman, 1960). It is approximately $\lambda_{s,dom} \sim 3.9\, h_P\, v_s / (k_B T) \sim 4$ Å in silicon dioxide. The requirement (b) is satisfied when $\Lambda_{s,p} \gg \Lambda_s$, where $\Lambda_{s,p} \sim 1/(N_P a^2)$ is the mean free path for geometrical scattering on pores of number density $N_P$ (Kittel and

Kroemer, 1976). The room-temperature phonon mean free path in amorphous materials is shown in Section 5.2.2 to be approximately $\Lambda_s = 5$ Å. Using $N_P a^3 \sim p$ allows (b) to be expressed as $a/p >> \Lambda_s$, which is less restrictive than (a) for amorphous materials. Requirement (a) indicates that the present analysis is valid when the pores are of dimension greater than about 50 Å. Such pores are distinct from the Angstrom-scale differences in structure proposed by Nagasimi (1972).

Research on thermal conduction in porous media was reviewed by Kaviany (1991). The low levels of porosity considered in this work, $p < 0.1$, make it reasonable to neglect the interaction of temperature fields around neighboring pores. Theories for this case considering pores of different shapes agree within a few percent for $p < 0.1$. The simplest of these is for conduction around a nonconducting sphere, and is approximated within 2 percent for $p < 0.1$ by

$$\frac{k_p}{k_d} = 1 - \frac{3}{2}p = \frac{3}{2}\frac{\rho_p}{\rho_d} - \frac{1}{2} \tag{5-13}$$

where $k_p$ is the effective thermal conductivity of the porous medium, $k_d$ is the thermal conductivity of the material surrounding the pores, and the conductivity within the pores is neglected. The use of this model assumes that the layer thickness is much larger than the pore dimension, $d >> a$, and that the pores do not have a columnar structure, such as is discussed by Lambropoulos (1991). If such columns are normal to the plane of the layer, i.e., microcracks, Eq. (5-13) underpredicts $k_p/k_d$.

The thermal conductivity within the LPCVD layers, $k_{int}$, is assumed to be given by Eq. (5-13) when $k_d = k_{bulk}$ is used. The thermal conductivity $k_{bulk}$ is that measured in nonporous, pure, bulk fused quartz (Sugawara, 1969), whose density is equal to that of the layer of Nagasimi (1972) which was annealed at 1273 K. Combining Eqs. (5-12) and (5-13) yields

$$\frac{k_{int}}{k_{bulk}} = 0.457 + 1.10\left(\frac{T_p}{T_r}\right) - 0.557\left(\frac{T_p}{T_r}\right)^2 \qquad (5\text{-}14)$$

Silicon dioxide layers fabricated using LPCVD contain up to 4 mass percent of silanol (SiOH), as observed by infrared spectroscopy (Adams, 1988). Impurities account for significant differences in the measured thermal conductivities of bulk fused silicon dioxide. The use of $k_d = k_{bulk}$, where $k_{bulk}$ is the value for a very pure sample, neglects the influence of the SiOH impurities on $k_d$, and may cause Eq. (5-14) to overpredict $k_{int}$. The effect of impurities on the thermal conductivity of LPCVD layers needs to be investigated.

## 5.4 Experimental Technique

The technique of Cahill et al. (1989), described in Section 3.3.1 and illustrated in Fig. 3-6, is adapted here to measured $k_{n,eff}$ in amorphous dielectric layers near room temperature with a known uncertainty.

### 5.4.1 Apparatus

Figure 5-5 is a cross section of the new test structure. The width of bridge A is $w = 5$ µm, yielding nearly nearly one-dimensional conduction normal to the sample layer. The width of the non-heating bridges is near 1 µm. Section 5.4.2 analyzes thermal conduction in the substrate, whose contribution to the uncertainty is estimated using a second non-heating bridge D. The center-to-center bridge separations are approximately $x_C = 7$ µm and $x_D = 16$ µm. The temperature change which occurs when the heater bridge A is switched on, i.e., when it suddenly carries a large current, is $\Delta T$. The temperature change $\Delta T_A$ is measured by bridge A, and $\Delta T_B$ is obtained from $\Delta T_C$ by modeling the heat conduction in the substrate. The conductivity $k_{n,eff}$ is calculated from the heater power $Q$ and length $L$ using

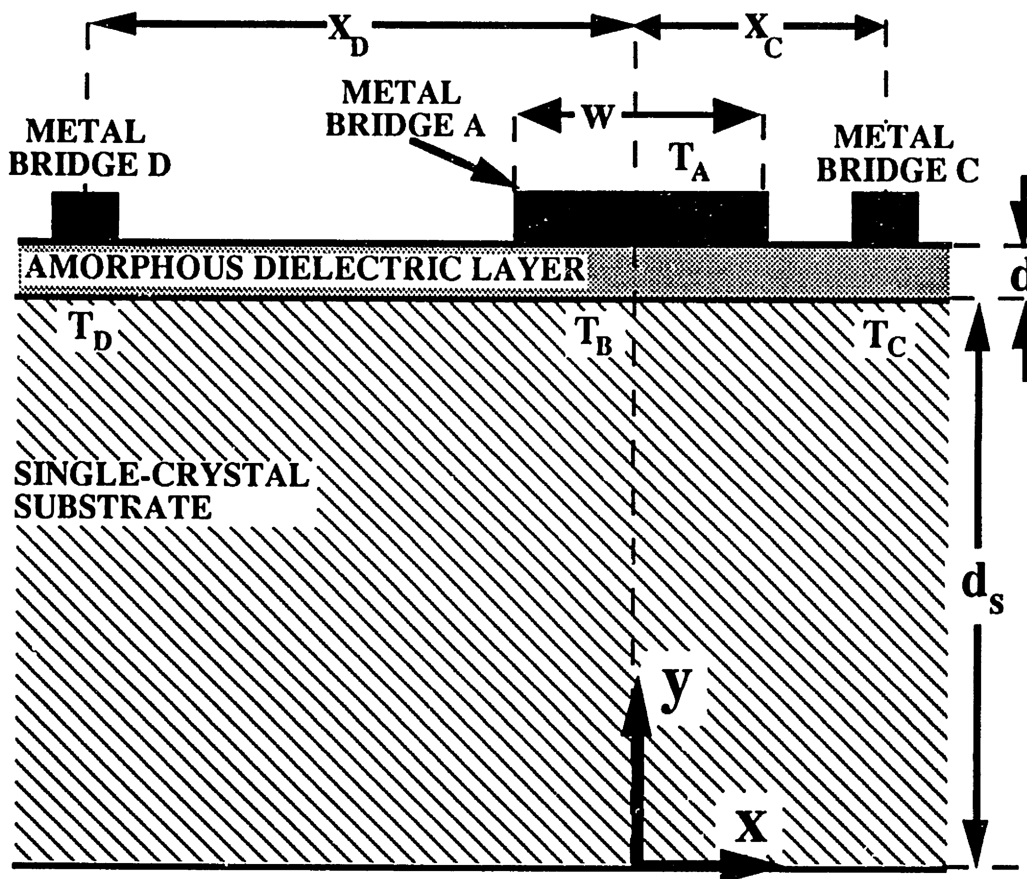


Fig. 5-5 Cross section of test structure used here to measure $k_{n,eff}$.

$$R_T = \frac{d}{k_{n,\,eff}} = \Psi \frac{\Delta T_A - \Delta T_B}{Q/(w\,L)} \tag{5-15}$$

where $\Psi$ is a parameter determined in Section 5.4.2 which depends on the ratio *w/d* and accounts for two-dimensional conduction in the sample layer.

The wafer is secured to a Temptronic Model TP38B temperature-control chuck, a copper disk with 88.9 mm diameter and thickness 19.1 mm, by means of suction through holes on the surface of the chuck. A thermocouple with one junction soldered to the chuck surface measures the test-structure temperature. The error due to this arrangement is determined using a second thermocouple attached to a wafer. The difference between the temperatures of the thermocouple junction and the test structure is due to temperature variations on the chuck surface, and is less than 0.5 K at 303 K, 1.5 K at 373 K, and 2.75 K at 423 K. The calibration of each bridge consists of determining the temperature derivative of its electrical resistance, which is affected by an error in the measured temperature *change* of the test structure. The relative uncertainty in the resistance thermometer calibration is be $U\,(\partial R_i/\,\partial T_i) = 0.04$ for all temperature changes between 273 and 423 K, where $U(q)$ is the relative uncertainty in the parameter $q$.

The bridge cross section is isothermal due to the low values of the thermal resistances for conduction normal to the bridge and across its cross section compared to the thermal resistance of the silicon dioxide layer. As a result, $w$ in Eq. (5-15) is the width of the aluminum-silicon dioxide contact. Scanning electron microscopy yields the relative dimensions of the cross section of the bridge, from which $w$ is calculated using the measured electrical resistivity of the bridge material and the length and electrical resistance of the bridge.

### 5.4.2 Substrate Thermal-Conduction Analysis

The temperature change $\Delta T_B$ is calculated from the measured $\Delta T_C$ by solving the heat diffusion equation, $\nabla^2 T = 0$, in the substrate. Except for the thinnest layers, the difference between $\Delta T_B$ and $\Delta T_C$ is much less than $\Delta T_A$, and approximations in this analysis have a small effect on the measurement. The model uses the two-dimensional coordinate system in Fig. 5-5 and the following approximations:

1. The effect of bridges C and D on conduction in the substrate is neglected. This results in a plane of symmetry and an adiabatic boundary condition at $x = 0$.
2. Substrate conduction is assumed to be two dimensional in the $x$-$y$ plane. The ratio of the bridge length to the substrate thickness is approximately 4.2.
3. The wafer is assumed to possess a uniform temperature $T_0$ at $y = 0$.
4. The energy flux from bridge A, of width near 5 μm, is uniform in $x$ and travels directly through the silicon dioxide layer of thickness less than 0.4 μm. This results in a heat-flux boundary condition at $y = d_{sub}$ of $- Q/(wL)$ for $0 < x < w/2$.
5. Conduction out of the substrate through the silicon dioxide to the air on top is neglected, yielding an adiabatic boundary condition at $y = d_{sub}$ for $x > w/2$.
6. The substrate side boundaries are assumed to be far from the heater compared to $d_{sub}$. The boundary condition there has no effect on the temperature near the heater. The boundary condition $T = T_0$ at $x = W$ and the requirement $W/d_{sub} >> 1$ are used.

Separation of variables yields $\Delta T_C$ and $\Delta T_D$,

$$\Delta T_{C,\,D} = \frac{2Q}{LwWk_{sub}} \sum_{i=0}^{\infty} \tanh\left(\lambda_i d_{sub}\right) \frac{\sin\left(\lambda_i w/2\right)\cos\left(\lambda_i x_{C,\,D}\right)}{\left(\lambda_i\right)^2}\,, \tag{5-16}$$

$$\lambda_i = \frac{\pi}{W}\left(\frac{2i+1}{2}\right)\,, \quad W >> d_{sub}$$

The average temperature at the interface of the silicon and the silicon-dioxide underneath the heater bridge is the average value of Eq. (5-16) for $0 < x < w/2$,

$$\Delta T_B = \frac{4Q}{Lw^2Wk} \sum_{i=0}^{\infty} \tanh\left(\lambda_i d_{sub}\right) \frac{\sin^2\left(\lambda_i w/2\right)}{\left(\lambda_i\right)^3} \tag{5-17}$$

The temperature difference $\Delta T_B$ for Eq. (5-15) is

$$\left[\Delta T_B\right]_{experiment} = \left[\Delta T_C\right]_{experiment} + \left[\Delta T_B - \Delta T_C\right]_{analysis} \tag{5-18}$$

The normalized uncertainty due to the approximate thermal-conduction analysis is estimated from the difference between the predicted and measured temperatures of bridges C and D,

$$U\left(\left[\Delta T_B - \Delta T_C\right]_{analysis}\right) = \frac{\left[\Delta T_C - \Delta T_D\right]_{experiment} - \left[\Delta T_C - \Delta T_D\right]_{analysis}}{\left[\Delta T_C - \Delta T_D\right]_{experiment}} \tag{5-19}$$

The parameter $\Psi$ in Eq. (5-15) is calculated by neglecting temperature variations in the $x$ direction at $y = d_{sub}$ compared to the temperature difference normal to the amorphous sample layer, and by assuming that the flux into the sample layer is uniform over the bridge width. The average temperature drop normal to the amorphous sample layer is given by Eq. (5-17) with the amorphous-layer thickness $d$ substituted for $d_{sub}$, yielding

$$\Psi = \left[\frac{W\, w\, d}{4 \sum_{i=0}^{\infty} \tanh\left(\lambda_i d\right) \sin^2\left(\lambda_i w / 2\right) / \left(\lambda_i\right)^3}\right] \tag{5-20}$$

Equation (5-20) is approximated by

$$\Psi = \left[1 - 0.54276 \frac{1 - 0.932 \exp\left(- 1.538 \frac{w}{d}\right)}{w / d}\right]^{-1} \tag{5-21}$$

which is within 0.5 percent for $w / d > 0.6$. This expression yields $\Psi = 1.084$ for $w / d = 7$, which is the largest value of this ratio in the present work.

### 5.4.3 Uncertainty Analysis

The thermal resistance determined in these experiments is related to the measured quantities by

$$R_T = \frac{\left[\Delta T_A\right]_{\mathrm{experiment}} - \left[\Delta T_C\right]_{\mathrm{experiment}} - \left[\Delta T_B - \Delta T_C\right]_{\mathrm{analysis}}}{Q/(w\,L)}$$

$$= \frac{\left[\Delta\left(\frac{V_A}{I_A}\right)\left(\frac{dR_A}{dT_A}\right)^{-1} - \frac{\Delta V_C}{I_C}\left(\frac{dR_C}{dT_C}\right)^{-1} - \left[\Delta T_B - \Delta T_C\right]_{\mathrm{analysis}}\right]}{I_A V_A/(w\,L)} \tag{5-22}$$

where $V_A$, $I_A$, $V_C$, and $I_C$ are the voltage drops and currents measured for bridges A and C. $\Delta(V_A/I_A)$ and $\Delta V_C/I_C$ are the changes of the resistances of bridges A and C which occur when $I_A$ is increased to turn the heater on. The current $I_C$ is very stable, but $I_A$, $V_A$, and $V_C$ experience small fluctuations in time which are used to for their uncertainties here. The uncertainty in the bridge length $L$ is negligible. For simplicity, the uncertainties in $\Delta(V_A/I_A)$ and $\Delta V_A$ are treated as independent. The total uncertainty in the thermal resistance is calculated using Eq. (5-22) and the sum-of-squares technique (Holman, 1984),

$$\begin{aligned}
\left[U(R_T)\right]^2 = {} & \left[U\left(\frac{dR_A}{dT_A}\right)\right]^2\left[\frac{\Delta T_A}{\Delta T_A - \Delta T_B}\right]^2 + \left[U\left(\Delta\left(\frac{V_A}{I_A}\right)\right)\right]^2\left[\frac{\Delta T_A}{\Delta T_A - \Delta T_B}\right]^2 \\
& + \left[U\left(\frac{dR_C}{dT_C}\right)\right]^2\left[\frac{\Delta T_C}{\Delta T_A - \Delta T_B}\right]^2 + \left[U\left(\Delta V_C\right)\right]^2\left[\frac{\Delta T_C}{\Delta T_A - \Delta T_B}\right]^2 \\
& + \left[U\left(\left[\Delta T_B - \Delta T_C\right]_{\mathrm{analysis}}\right)\right]^2\left[\frac{\Delta T_B - \Delta T_C}{\Delta T_A - \Delta T_B}\right]^2 \\
& + \left[U(V_A)\right]^2 + \left[U(I_A)\right]^2 + \left[U(w)\right]^2
\end{aligned} \tag{5-23}$$

The relative uncertainty in $R_T$ is found to be very similar for measurements yielding the same value of $R_T$. For $R_T \sim 5 \times 10^{-7}$, $1.5 \times 10^{-7}$, and $0.5 \times 10^{-7}$ m$^2$ K W$^{-1}$, $U(R_T)$ is approximately 8, 11, and 22 percent, respectively. The uncertainty is dominated by the uncertainty in the measured temperature derivative of the electrical resistance of bridge A. For the thinnest layers, where $\Delta T_B - \Delta T_C$ can be comparable to $\Delta T_A - \Delta T_B$, the uncertainty due to the thermal analysis is significant. This technique is similar to those of Schafft et al. (1989) and Brotzen et al. (1989), because it uses a thin-layer bridge to heat the sample layer. But both sets of authors determined $\Delta T_B$ using the measured temperature at the *bottom* of the substrate. This temperature difference is always much larger than $\Delta T_B - \Delta T_C$, so that the approximations in the thermal-conduction analysis are much more important than those used here. It is important to minimize this component of the uncertainty when measuring very thin layers, i.e., $d \leq 0.1$ μm. While this uncertainty was negligible in the measurements of Schafft et al. (1989) for layers thicker than 1 μm, its impact on the data of Brotzen et al. (1992) for layers as thin as 0.1 μm needs to be assessed.

## 5.5 Results and Discussion

### 5.5.1 Phonon-Boundary Scattering and $k_{n,eff}$ of SIMOX Layers

Figure 5-6 compares the predictions of the phonon-boundary scattering analysis with the low-temperature data of Schwartz and Pohl (1989). They measured $R_T$ for PECVD silicon dioxide layers bounded by Rh:Fe, rhodium with a small fraction of iron, and sapphire. The data points are represented in this plot of $k_{n,eff} / k_{bulk}$ using the $k_{bulk}$ data of Zeller and Pohl (1971). Boundary scattering becomes more important at low temperatures because low-frequency phonons, which have long mean free paths, contribute more to the conductivity. The agreement is excellent at 10 K for a range of thicknesses spanning more than an order of magnitude, which supports the frequency-dependence of

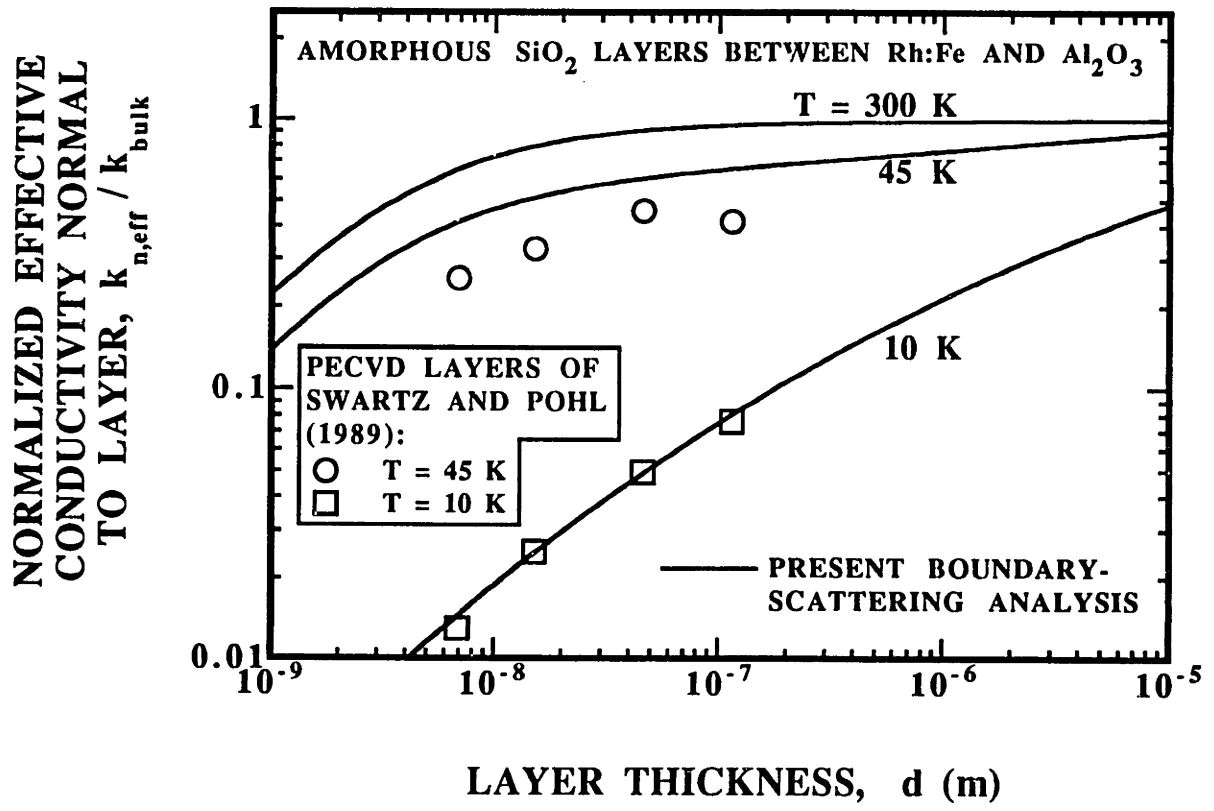


Fig. 5-6 Predictions of the thermal conductivity ratio $k_{n,eff} / k_{bulk}$ considering phonon-boundary scattering, compared with data for PECVD silicon-dioxide layers.

the mean free path given in Fig. 5-3 and the approximate solution to the transport equation, Eqs. (5-2) - (5-4). The success of the prediction at 10 K relies heavily on the transmission coefficients calculated using the diffuse mismatch model of Swartz and Pohl (1989), because at this temperature many phonons travel ballistically between the boundaries, without scattering internally. At 45 K, the ratio $k_{n,eff}/ k_{bulk}$ is overpredicted by the present analysis. This would be consistent with the *agreement* at 10 K if the phonon mean free paths in the layers were the same as in Fig. 5-3 in the low and the intermediate frequency regimes, which are most important at low temperatures, but were less than those given in Fig. 3 in the high frequency regime, which becomes important above about 10 K. But Fig. 5-3 may still be correct for bulk fused silicon dioxide, since this material may have a different microstructure than the PECVD layers. The poor agreement at 45 K may also be due to a failure of the diffuse mismatch model above 30 K. This failure was observed for many interfaces by Swartz and Pohl (1989), who argued that highly-resistive interfacial layers at the interfaces could be responsible.

Figure 5-6 shows that $k_{n,eff}/ k_{bulk}$ is approximately unity at room temperature for layers thicker than a few hundred Angstroms, i.e., phonon-boundary scattering is not important. This is also the case if the calculation is performed using the transmission coefficients from silicon dioxide into aluminum and silicon, which were the bounding materials for the layers whose conductivities are given in Fig. 5-1. But the data in Fig. 5-1 yield ratios $k_{n,eff}/ k_{bulk}$ which are much smaller than unity, indicating that the problem at 45 K in Fig. 5-6 becomes more important at higher temperatures.

The mean free paths used here are probably the largest possible in the layers. This is because microstructural differences between the layer and a bulk material may include a finite porosity, particularly near the boundaries of the layer, or the presence of small crystalline regions, both of which reduce the mean free paths of long-wavelength phonons. Similarly, the mean free paths of long-wavelength phonons are reduced by localized regions of different stoichiometry, which perturb the elastic properties of the material. As a

result, the ratios given in Fig. 5-6 indicate the greatest possible impact of boundary scattering on $k_{n,eff}$.

The SOI wafers employed in this study were fabricated by Ibis Corporation in Danvers, Massachusetts, using the SIMOX process, which is depicted in Fig. 5-7. Oxygen atoms are implanted into a lightly-doped single-crystal silicon substrate, forming a damaged sublayer. After an anneal near 1500 K, a silicon-dioxide layer forms beneath a single-crystal silicon overlayer of thickness 0.22 μm. Devices are usually fabricated from the silicon overlayer. In this work, the silicon overlayers are etched away from SOI wafers, and the bridges of the test structure are deposited onto the exposed silicon-dioxide layers, which have thicknesses near 0.3 μm. Figure 5-8 compares the data for the SIMOX layers with the predictions of the phonon-boundary scattering analysis. *Microscale* analysis considers phonon-boundary scattering, $R_T = d / k_{n,eff}$, while *macroscale* analysis yields the volume resistance of a layer from the bulk conductivity, $R_T = d / k_{bulk}$. The microscale and macroscale predictions are within 3 percent of each other, which is consistent with $k_{n,eff} / k_{bulk} \sim 1$ shown in Fig. 5-6 for room temperature layers. Due to the experimental uncertainty, the data are consistent with the boundary-scattering analysis, but cannot confirm or refute its validity for thinner layers or lower temperatures. Figure 5-6 indicates that a 10 percent reduction in the effective conductivity normal to the layer will be measured at room temperature only in layers thinner than about 420 Å. Since the thermal resistance of such a layer is already quite small, the impact of boundary scattering at room temperature on practical applications is not very important.

The data show that the SIMOX fabrication technique results in layers which are far different than those fabricated using the other techniques summarized in Table 5-1. conductivities $k_{n,eff}$ of SIMOX layers agree very well with $k_{bulk}$, which is a first for amorphous silicon dioxide layers and is in stark contrast with the data shown in Fig. 5-1. Previously reported conductivities vary from between two orders of magnitude smaller (Guenther and McIver, 1988) to about 70 percent of the bulk values. The data provide

**1. OXYGEN-ION IMPLANTATION**

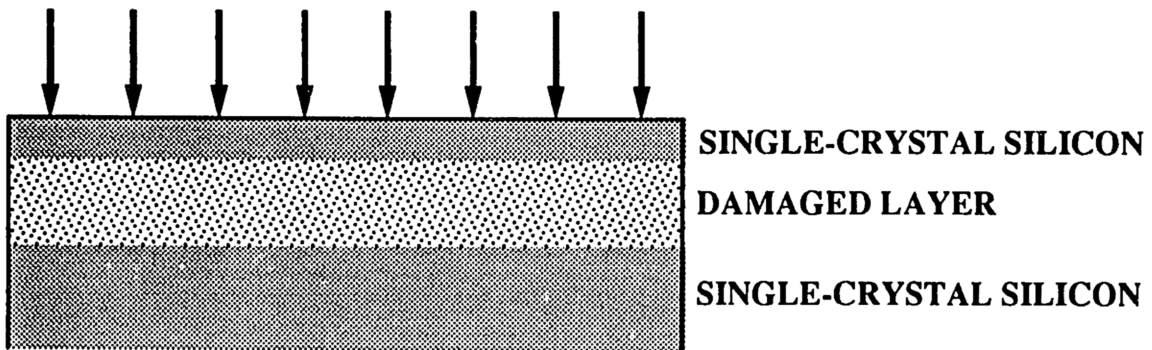


**2. ANNEAL NEAR 1500 K**

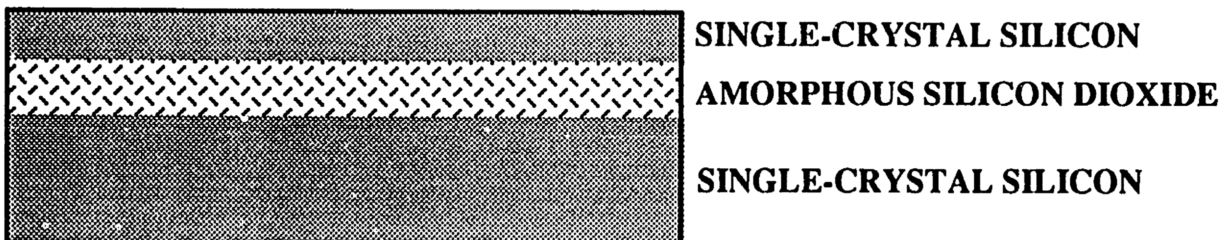


Fig. 5-7 Separation by implantation with oxygen (SIMOX) fabrication process (e.g., Celler and White, 1992).

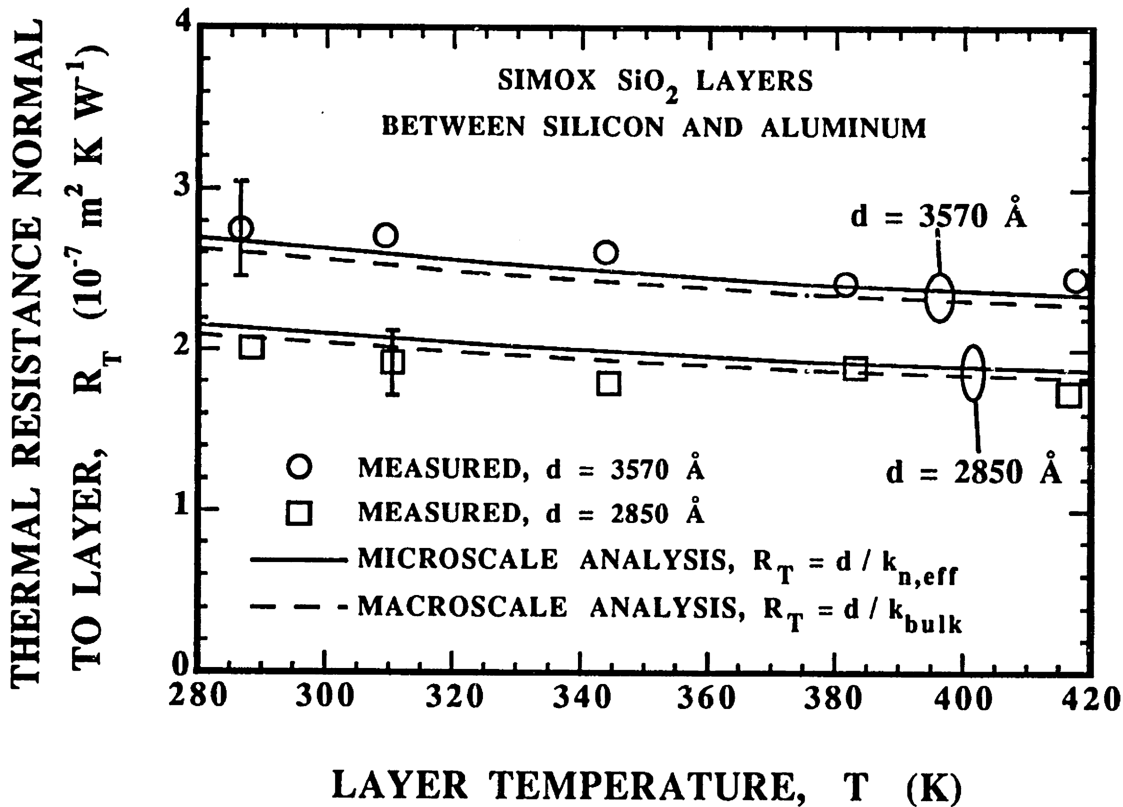


Fig. 5-8 Comparison of boundary-scattering (microscale) analysis with data for SIMOX silicon-dioxide layers.

strong evidence that both the microstructure and stoichiometry of the annealed SOI silicon dioxide layers closely resemble those in bulk samples. The absence of a thickness-dependent conductivity in these layers indicates that neither thermal boundary resistances nor highly-resistive interfacial layers are present. These findings are important for the designers of SOI circuits and for Chapter 6 of the present work, which analyzes conduction in SOI circuits, because they make it appropriate to use $k_{n,eff} = k_{bulk}$ rather than the much smaller values of $k_{n,eff}$ reported previously for silicon-dioxide layers.

### 5.5.2 Effect of Annealing Temperature on $k_{n,eff}$ of LPCVD Layers

The LPCVD layers are deposited at 673 K using a mixture of $SiH_4$ and $O_2$. Sets of test structures are either measured as deposited, or are measured after a 30 minute anneal at 873, 1173, or 1423 K. The temperatures of the layers annealed at 1173 and 1423 K are slowly reduced to 1073 K over periods of 40 and 90 minutes, respectively, after which they are removed from the oven and exposed to room-temperature air. The layers annealed at 873 K are removed from the oven directly after the anneal.

Figure 5-9 shows the values of $k_{n,eff}$ measured here. The data denoted by $T_p$ = 673 K are for unannealed layers. For a given thickness, the values of $k_{n,eff}$ are much larger than those reported by Lambropoulos et al. (1989), Brotzen et al. (1992), and Schafft et al. (1989), but are less than the recommended bulk value and the values measured here for SIMOX layers. The difference between the data measured here and those of Lambropoulos et al. (1989) is not significant considering the experimental uncertainty. The uncertainty in the thermal-comparator technique of Lambropoulos et al. (1989) is governed by that in the radius of the probe-layer contact. The contact radius was estimated to be between 20 μm and 180 μm. The measured conductivity was inversely proportional to this radius, which was assumed to be 100 μm. If the contact radius was 20 μm, all of the data would need to be increased by a factor of 5, which in every case would yield $k_{n,eff}$ larger than $k_{bulk}$. The difference between the data measured here and

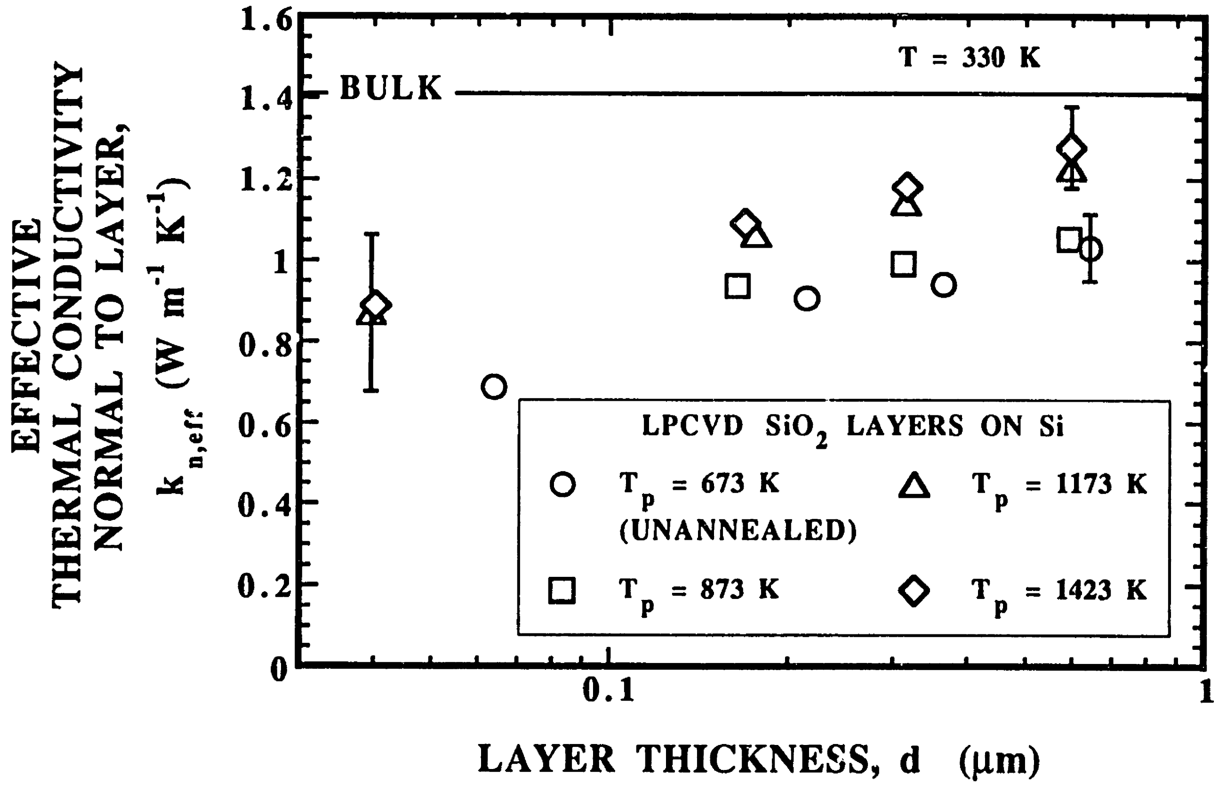


Fig. 5-9 Data of the present work for $k_{n,eff}$ of LPCVD silicon dioxide layers with varying annealing temperatures. The unannealed layers are denoted by $T_p$ = 673 K.

those of Schafft et al. (1989) may be due to the difference in the materials measured. Their data are for silicon-dioxide layers with 4 mass percent of phosphorus. The effect of this impurity on the thermal conductivity needs to be investigated.

Comparison of the data measured here with those of Brotzen et al. (1989) yields a puzzle. The low values of $k_{n,eff}$ reported by Brotzen et al. (1992) may be due to a different microstructure resulting from the PECVD process, which occurs at lower temperatures than LPCVD. The porosity model developed in Section 5.3 is consistent with the data of Brotzen et al. (1992) only if a very large thermal boundary resistance is assumed. Using a lower-bound temperature for PECVD of 473 K (Adams, 1988) in Eq. (5-14) yields $k_{int} / k_{bulk} = 0.78$, which agrees with the reported $k_{n,eff}$ for the 0.1 μm layer only if $R_B \sim 10^{-6}$ m$^2$ K W$^{-1}$ is used in Eq. (5-10). This thermal boundary resistance is larger than all of the *total* thermal resistances $R_T$ measured here, and is nearly two orders of magnitude larger than the $R_T$ measured here in the thinnest layers. The uncertainty in the technique of Brotzen et al. (1992) for the thinnest layers still needs to be assessed. But there appears to be a dramatic difference between the properties of LPCVD and PECVD silicon-dioxide layers near their boundaries with silicon, which must be investigated further.

The values of $k_{n,eff}$ measured here for the highest annealing temperature are somewhat less than those measured in the SIMOX layers. But when Eq. (5-10) is applied to the LPCVD layers of the present study, the value of $k_{int}$ for the highest annealing temperature is only 5 percent less than $k_{bulk}$. Thus, the difference between the values of $k_{n,eff}$ for the SIMOX layers and the LPCVD layers annealed at 1423 K may be due to a larger thermal boundary resistance in the LPCVD layers. The SIMOX fabrication process implants oxygen ions directly into silicon, providing no opportunity for impurities to enter the layer. This is not the case for the LPCVD layers, whose lower values of $k_{n,eff}$ may also be due to the presence of SiOH.

The data of the present work show that $k_{n,eff}$ increases with $T_p$ at a given layer thickness. The low experimental uncertainty of the thickest layers allows the data to

demonstrate this for $T_p$ = 673 and 1423 K. Figure 5-10 shows the dependence of the layer thermal resistance on thickness and $T_p$. The lines in this figure are linear regressions of the data for a given value of $T_p$, and are used in Eq. (5-10) to determine $k_{int}$ and $R_B$. The local conductivity $k(y)$ in Eq. (5-11) may decrease as $y$ approaches zero, i.e., near the layer-substrate interface. This is checked by estimating $k(y)$ far from the substrate-layer interface, which is approximately the inverse of the slope of the line segment connecting the right-most two data points for a given annealing temperature in Fig. 5-10. For each case, this yields a local conductivity which is slightly larger than $k_{int}$, by between 2 and 8 percent. This may be due to a porosity which decreases with increasing $y$. But the difference between the largest local conductivity $k(y)$ estimated in this way and $k_{int}$ is less than the experimental error in $k_{int}$ for each case, making it inappropriate to draw conclusions about local values of $k(y)$.

The values of $k_{int}$ and $R_B$ are given in Table 5-2. An annealing-temperature dependence of $R_B$ cannot be resolved due to the experimental uncertainty, but for each case

Table 5-2 Values of $k_{int}$ and $R_B$ extracted from the data for each value of the highest processing temperature, $T_p$.

| | $k_{int}$ (W m$^{-1}$ K$^{-1}$) | $R_B$ ($10^{-7}$ m$^2$ K W$^{-1}$) |
|---|---|---|
| $T_p$ = 673 K (unannealed) | 1.08 +/- 0.09 | 0.36 +/- 0.12 |
| $T_p$ = 873 K | 1.11 +/- 0.09 | 0.27 +/- 0.10 |
| $T_p$ = 1173 K | 1.28 +/- 0.10 | 0.21 +/- 0.10 |
| $T_p$ = 1423 K | 1.34 +/- 0.10 | 0.25 +/- 0.13 |

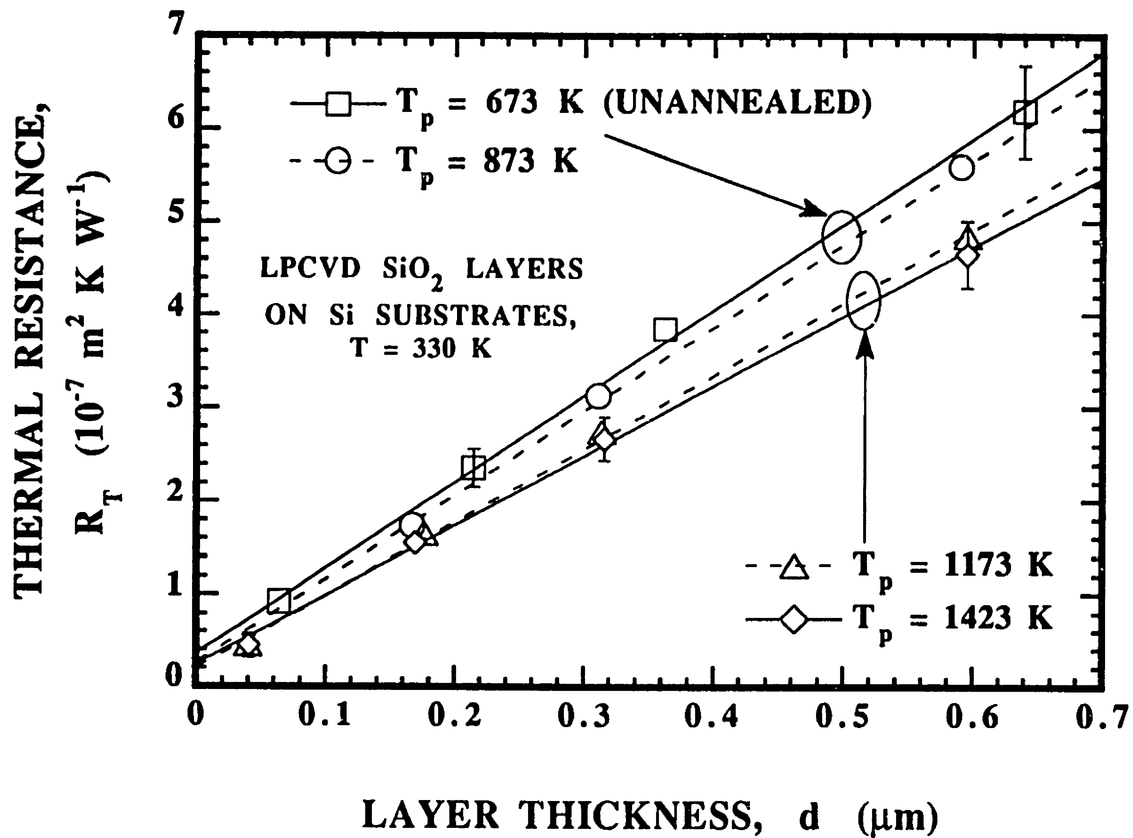


Fig. 5-10 Thermal resistance data for conduction normal to the LPCVD layers. The lines are linear regressions of the data for each value of $T_p$, from which Eq. (5-10) yields $k_{int}$ and $R_B$.

$R_B$ must be less than 5 x $10^{-8}$ $m^2$ K $W^{-1}$. Figure 5-11 compares the predictions of the model developed in Section 5.3 with the measured dependence of $k_{int}$ on $T_p$. The data show that annealing increases $k_{int}$ by up to 23 percent, which agrees very well with the magnitude of the change predicted by the model. The agreement of the data with the model for the maximum value of $T_p$ is good considering that the impurities in the LPCVD layers are neglected. If these impurities reduce $k_d$ by 10 percent compared to $k_{bulk}$, the model agrees within the experimental uncertainty with all of the data. But a model accounting for the impurities should consider the possibility that their concentration changes due to annealing. The difference between the data and the predictions at the lower values of $T_p$ may be due to the layers measured here having densities different from those of the layers of Nagasimi (1972). It is also possible that a mechanism other than porosity accounts for the annealing-temperature dependence of $k_{int}$.

## 5.6 Concluding Remarks

This work shows that phonon-boundary scattering is of little practical importance in silicon dioxide layers above room temperature. The low conductivities in Fig. 5-1 measured elsewhere must be attributed due to one of the remaining two hypotheses discussed in Section 5.1, (b) a thickness-dependent microstructure or stoichiometry, or (c) thermal boundary resistances or distinct, highly-resistive interfacial layers. The interfacial layer hypothesis is questionable. For an interfacial layer to contribute significantly to the total thermal resistance, it would need a thermal conductivity much smaller than the remainder of the amorphous silicon dioxide, which has a thermal conductivity among the lowest of any nonporous solid. A more plausible explanation is an increased porosity near the boundaries of the layer. This porosity would need to be considerably larger than largest value used here for the unannealed LPCVD layers to account for the data in Fig. 5-1. The large or unknown uncertainties of the previous data for $k_{n,eff}$ in Fig. 5-1 show that there is

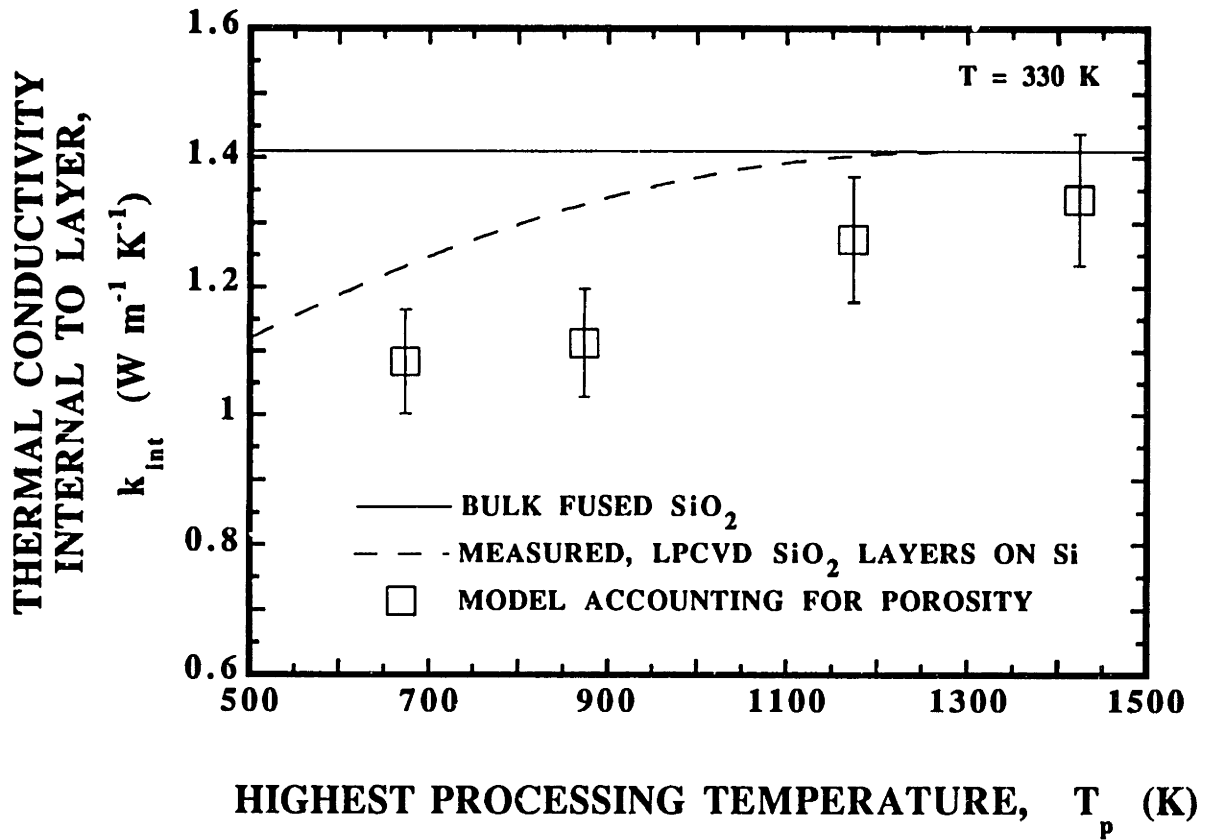


Fig. 5-11 Thermal conductivity internal to the LPCVD layers, $k_{int}$. Each data point is the inverse of the slope of a line in Fig. 5-10.

a need for standardized techniques for this measurement with well-known limitations, such as exist for bulk solids. The technique used here is recommended as a standard.

This work shows the importance of measuring the conductivity of layers fabricated in the same way as those in the circuit for which the effective thermal conductivity is needed. A SOI circuit designer using data from Fig. 5-1 rather than from Fig. 5-8 for $k_{n,eff}$ of the implanted layer would overpredict the temperature of devices and interconnects, which could result in a circuit of lower performance because it was overdesigned for interconnect reliability. Using the PECVD data of Brotzen et al. (1992) to calculate the temperature drop normal to LPCVD layers could result in a similar error.

Deposited silicon dioxide layers with thermal conductivities approaching those of bulk fused silicon dioxide can be achieved by choosing the correct fabrication process. This is very positive information for the designers of integrated circuits. The thermal conductivity can be improved by up to an order of magnitude by the use of the LPCVD rather than the PECVD fabrication process, and an improvement of an additional 23 percent can be obtained by annealing when this is possible. These improvements come at the price of higher processing temperatures, which may not be compatible with the state of the wafer. For example, when the silicon dioxide is deposited after aluminum, $T_p$ must be below about 723 K, where considerable diffusion of silicon into aluminum occurs.

The large difference between the conductivities of the LPCVD and PECVD layers is an unsolved problem. There is an urgent need for direct measurements of microstructural properties, employing electron diffraction, infrared spectroscopy, and transmission- and scanning-electron microscopy, of the layers in thermal-conductivity measurement test structures. Such a research effort may help to resolve the outstanding puzzle presented by the data shown in Figs. 5-1 and 5-9.

# 6. PREDICTION AND MEASUREMENT OF TEMPERATURE FIELDS IN SILICON-ON-INSULATOR ELECTRONIC CIRCUITS

## 6.1 Introduction

As the lateral dimensions of transistors decrease, an increasing fraction of the transistor-to-coolant temperature difference in an electronic system can be governed by thermal conduction within a few micrometers of the transistors. This may be most important in silicon-on-insulator (SOI) electronic circuits. As illustrated in Fig. 1-2, SOI FETs are electrically insulated from the substrate by an implanted silicon-dioxide layer, which improves the electrical performance of the devices but inhibits conduction cooling of the channel by the substrate. The implantation process is depicted in Fig. 5-7. McDaid et al. (1989) indicated that the self-heating of SOI FETs can decrease the drain current for given gate and drain voltages. Higher operating temperatures may also reduce the median time to failure (MTF) of interconnects due to electromigration. The SOI circuit designer needs to know the temperature fields in SOI FETs resulting from self heating.

Chapter 5 determined the thermal conductivity of the implanted silicon dioxide layer in SIMOX wafers. Chapter 6 predicts and measures the channel temperature of SOI FETs by modeling the source, drain, gate, and interconnects as cooling fins. The thermal analysis yields a closed form solution for the temperature field in the FET and interconnects, allowing the influence of design dimensions to be assessed. The available experimental techniques measure an average SOI FET temperature (Lifka and Woerlee, 1990; Bunyan et al., 1991) and have insufficient resolution to confirm this analysis. A

technique is developed here to measure the channel temperature which uses the gate as an electrical-resistance thermometer. The technique is similar to one for bulk FETs (Mautry and Trager, 1990), but requires a new thermal analysis to calculate the channel temperature from the gate electrical resistance. The SOI FET temperature field is shown to depend strongly on circuit design parameters, e.g., the device thickness. This work indicates that FET dimensions can be chosen to improve the MTF of FET-interconnect contacts. At low temperatures, thermal conduction from the channel may be reduced by heat-carrier boundary scattering in the source, gate, drain, and interconnects. The thermal model is adapted to estimate the effect of boundary scattering on the channel-to-substrate thermal conductance using existing theory for the conduction size effect in thin layers.

This chapter helps to determine the impact of the thermal resistance of the implanted layer on the practical potential of SOI technology. The thermal model will help with an optimization of the implanted-layer thickness considering its influence on both the temperature field and the electrical performance of FETs. The channel-temperature measurement technique developed has a resolution in the $X$ direction in Fig. 1-2 which is equal to the channel length. It can be used to measure temperature locally in the transistor with a satisfactory resolution even as the channel length decreases. Previous work has shown that the boundary scattering of heat carriers can influence the heat flux in simple geometries, e.g., normal to a layer. This chapter shows that microscale conduction phenomena can have an impact on circuit design.

Section 6.2 develops the thermal model for SOI FETs, and discusses its application to the experimental test structure used here. Section 6.3 describes the experimental technique, and Section 6.4 compares the predictions of the model with the data, and gives the estimates for the effects of microscale conduction.

### 6.2 Thermal Analysis

#### 6.2.1 Multi-Fin Model

Some of the materials in SOI circuits have thermal conductivities which are much larger than that of the implanted silicon dioxide layer, as shown in Table 6-1. This section uses this disparity to develop a simple model for thermal conduction in SOI FETs. The model is for steady-state FET operation, which is the case in most measurements of FET electrical properties. The time required for steady-state to be achieved is near $(d_o)^2 / \alpha_o$,

Table 6-1 Thermal conductivities of SOI circuit materials. These values were measured in bulk samples, although many of the components in the FETs are thin layers. The basis for the use of these values is given in Section 6.2.2.

| Region or Component | Material | Thermal Conductivity For $T_0$ = 303 K ($W\ m^{-1}\ K^{-1}$) |
|---|---|---|
| Substrate | Single-Crystal Silicon, 3 x $10^{15}$ Boron Atoms $cm^{-3}$ | $k_{sub}$= 148* |
| Channel | Single-Crystal Silicon 6 x $10^{17}$ Boron Atoms $cm^{-3}$ | $k_c$ = 148* |
| Source And Drain | Single-Crystal Silicon, 1 x $10^{20}$ Arsenic Atoms $cm^{-3}$ | $k_d$ = 63* |
| Gate | Polysilicon, 1 x $10^{20}$ Arsenic Atoms $cm^{-3}$ | $k_g$ = 63* |
| Interconnect | Aluminum, 1 Mass-Percent Silicon | $k_m$ = 239* |
| SOI Implanted Layer | Silicon Dioxide, Implanted | $k_o$ = 1.40** |
| Other Insulating Layers | Silicon Dioxide, Thermally Grown or CVD | $k_{th}$ = 1.40** |

*Touloukian et al. (1970a) **Sugawara (1969)

where $\alpha_o$ is the thermal diffusivity of silicon dioxide, yielding about 200 ns at 300 K. For steady-periodic power dissipation, which can occur in clock-driven circuits, the model yields a good estimate of the temperature in the source, drain, gate, and interconnects at points separated from the channel by at least one thermal penetration depth. If $t_c = 5$ ns is the clock period, the thermal penetration depth in the silicon source, drain, and gate is $(t_c \alpha_d)^{1/2} = 0.4$ μm, where $\alpha_d$ is the thermal diffusivity of heavily-doped silicon.

The base-case dimensions used when the thermal model is applied to devices are given in Table 1-1. Many of these dimensions were reported for the ultra-thin SOI FET of Woerlee et al. (1989). A typical value of the device operating power calculated from the current-voltage data in this reference is $P = 0.74$ mW for a gate-to-substrate bias of 3 V. The rate of Joule heating in the source and drain, $2\, I^2 L_d\, \rho_e / (w d_d)$, where $\rho_e$ is the electrical resistivity of the source and drain based on the carrier concentration (Muller and Kamins, 1986), is nearly two orders of magnitude smaller than the device power and is neglected. Joule heating is also negligible in the aluminum interconnects. The channel is modeled as an isothermal heating source. This neglects the complex distribution of heating intensity in a real device, but yields a good estimate of the average channel temperature.

For a circuit packaged in a chip, the tops of the devices and interconnects are covered by a thermally-insulating layer, typically made of silicon dioxide or silicon nitride, which is thicker than the silicon-dioxide layer separating the device components and interconnects from the substrate. The model neglects heat transfer from the tops of devices and interconnects because the resulting thermal resistance is much larger than that for conduction to the chip housing through the implanted silicon dioxide layer and the high-conductivity substrate. Variations in the temperature of the substrate-silicon dioxide interface are small compared to those within the implanted layer due to the high thermal conductivity of the substrate, and this interface is assumed to possess the uniform temperature $T_0$.

The source, drain, gate, and interconnects are modeled as one-dimensional cooling fins for the energy dissipated in the channel. The local thickness of silicon dioxide separating a fin from the substrate is $d_{lo}$. The temperature difference in the $Z$ direction in each fin is negligible compared to that in the silicon dioxide below it because $d_{lo} / k_o$ is nearly two orders of magnitude larger than $d_m / k_m$, $d_d / k_d$ , and $d_g / k_g$ for each case. Each fin is nearly isothermal across its width $w$ because the ratio of the thermal resistance for conduction across its width to that for conduction down through the underlying silicon dioxide, $(w / k\, d)/(d_{lo} / k_o\, w)$, where $k$ and $d$ are the fin conductivity and thickness, is much smaller than unity for each fin. The heat flow in the silicon dioxide in the direction along each fin is negligible compared to that in the fin because the ratios $k_o\, d_{lo} / (k_m\, d_m)$, $k_o\, d_{lo} /(k_d\, d_d)$, and $k_o\, d_{lo} / (k_g\, d_g)$ are all much less than unity.

The local heat flux from the device or interconnect to the substrate through the silicon dioxide is $h\,(T - T_0)$, where $T$ is the local device or interconnect temperature. The heat transfer coefficient is $h = \Psi k_o/d_{lo}$ where $k_o / d_{lo}$ is the inverse volume resistance of the silicon dioxide layer. The dimensionless parameter $\Psi$ is greater than unity and accounts for two-dimensional conduction in the silicon dioxide in the $X$-$Z$ plane for the gate, and in the $Y$-$Z$ plane for the source, drain, channel, and interconnects. It depends on the ratio $w/d_{lo}$, where $w$ is the width of the fin in the $Y$ direction for the source, drain, channel, and interconnects, and is the width in the $X$ direction of the gate fin. In the limit $w/d_{lo} >> 1$, the conduction in the silicon dioxide layer is one dimensional in the $Z$ direction, and $\Psi$ approaches unity. If the fin is assumed to deliver a heat flux to the silicon dioxide which does not vary across the width of the fin, $\Psi$ is well approximated by Eq. (5-21). Because the fins are isothermal across their width, the heat-flux distribution into the silicon dioxide is peaked at the side edges of the fin. This results in a value of $\Psi$ which is larger than that predicted by assuming that the heat flux is uniform over the fin width. The largest possible error due to the use of Eq. (5-21) is 10 percent, determined using separation of variables and a heat flux distribution which peaks at the fin edges. The inverse thermal healing

length in a fin is $m = (h / k\, d)^{1/2}$, where $k$ is the thermal conductivity within the fin and $d$ is the fin thickness. The product of the spatial coordinate in the fin and $m$ is the argument of the exponential functions which solve the heat equation. The distance from a heating source over which the fin temperature recovers to the substrate temperature is of the order of the healing length.

Figure 6-1 is a schematic of the thermal model showing the fin geometry. The devices are assumed to be in an infinite linear array, each connected by an interconnect of length $2L_m$, and each dissipating the same power $P$. This idealization results in an estimate of the worst-case temperature distribution in a real circuit for a given value of the device separation, $2L_m$. It yields the two planes of symmetry shown, which are adiabatic boundaries. The heat-transfer coefficient from the portion of the interconnect over the drain is larger than $h_m$, but the heat transfer from the interconnect is calculated using $h_m$ for all values of $x_m$. This is justified if $L_m$ and the thermal healing length in the interconnect, $1 / m_m = (k_m\, d_m / h_m)^{1/2} = 6.6$ μm, are large compared to the length of the overlap. The additional silicon dioxide in Fig. 1-1 consists of a thermally-grown layer of thickness about 0.25 μm and a deposited layer of thickness 0.35 μm. The gate is sandwiched between these two layers. At $x_g \sim 2$ μm the gate reaches a metal contact. In the present approximate analysis, the gate is treated as a doped polysilicon fin of infinite length separated from the substrate by an oxide of constant thickness ($d_o$ + 0.25 μm), neglecting the contact. The error resulting from this simplification is not large due to the short thermal healing length in the gate, $1 / m_g = (k_g\, d_g / h_g)^{1/2} = 2.1$ μm. The thermal healing length in the drain is $1 / m_d = (k_d\, d_d / h_d)^{1/2} = 1.0$ μm. The temperature and location within the interconnect are given by $T_m$ and the coordinate $x_m$, within the drain by $T_d$ and $x_d$, and within the gate by $T_g$ and $x_g$. The channel temperature is $T_c$. The gate is separated from the channel by a thin silicon dioxide layer, of thickness $d_{go} = 5.5$ nm. The channel temperature is assumed to be equal to the gate temperature at $x_g = 0$. This is justified because the thermal resistance of

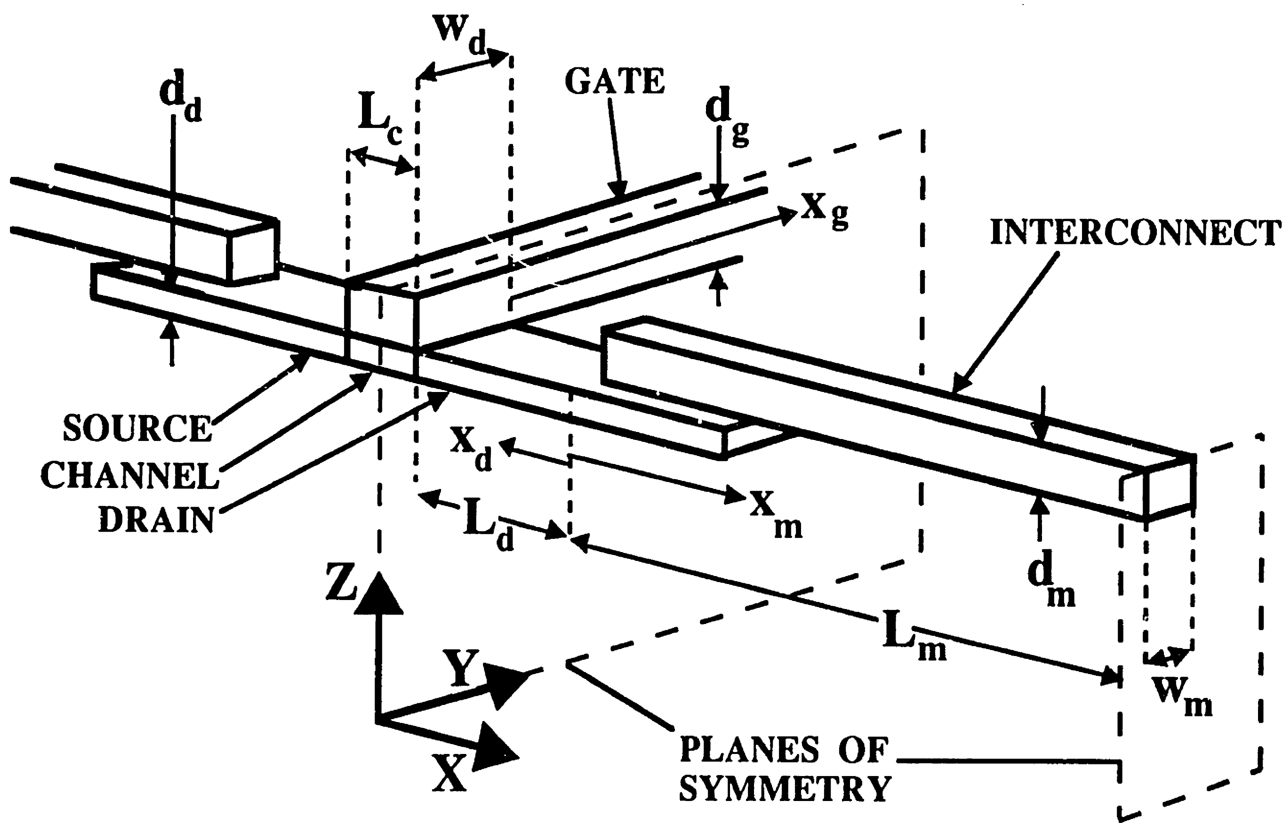


Fig. 6-1 Physical model of a SOI FET.

the thin oxide, $d_{go}/(L_c\, w_d\, k_o) \sim 9.8 \times 10^3$ K W$^{-1}$, is small compared to that for conduction out through the gate and the buried silicon dioxide, which is approximately $1\,/\,(m_g\, L_c\, d_g\, k_d) \sim 2.2 \times 10^5$ K W$^{-1}$.

The one-dimensional energy equations and boundary conditions are

$$\frac{\mathrm{d}^2 T_m}{\mathrm{d}x_m^2} - (m_m)^2 (T_m - T_0) = 0 \tag{6-1}$$

$$\frac{\mathrm{d}^2 T_d}{\mathrm{d}x_d^2} - (m_d)^2 (T_d - T_0) = 0 \tag{6-2}$$

$$\frac{\mathrm{d}^2 T_g}{\mathrm{d}x_g^2} - (m_g)^2 (T_g - T_0) = 0 \tag{6-3}$$

$$T_m (x_m = 0) = T_d (x_d = 0) \tag{6-4}$$

$$T_d (x_d = L_d) = T_g (x_g = 0) = T_c \tag{6-5}$$

$$T_g \left(x_g \to \infty\right) = T_0 \tag{6-6}$$

$$\left(\frac{\mathrm{d}T_m}{\mathrm{d}x_m}\right)_{x_m = L_m} = 0 \tag{6-7}$$

$$- k_m w_m\, d_m \left(\frac{\mathrm{d}T_m}{\mathrm{d}x_m}\right)_{x_m = 0} - k_d w_d\, d_d \left(\frac{\mathrm{d}T_d}{\mathrm{d}x_d}\right)_{x_d = 0} = 0 \tag{6-8}$$

$$k_d w_d\, d_d \left(\frac{\mathrm{d}T_d}{\mathrm{d}x_d}\right)_{x_d = L_d} - \frac{k_g\, L_c\, d_g}{2} \left(\frac{\mathrm{d}T_g}{\mathrm{d}x_g}\right)_{x_g = 0} + \frac{h_d\, w_d\, L_c}{2} (T_c - T_0) = \frac{P}{2} \tag{6-9}$$

The solutions to these equations are

$$T_m - T_0 = Z_1 \cosh\left[m_m (L_m - x_m)\right] \tag{6-10}$$

$$T_d - T_0 = Z_2 \exp\left[m_d x_d\right] + Z_3 \exp\left[-m_d x_d\right] \tag{6-11}$$

$$T_g - T_0 = Z_4 \exp\left[-m_g x_g\right] \tag{6-12}$$

The coefficients $Z_1$, $Z_2$, $Z_3$, and $Z_4$ are determined using the following matrix equation:

$$\begin{bmatrix} -m_m k_m d_m w_m \times \sinh(m_m L_m) & m_d k_d d_d w_d & -m_d k_d d_d w_d & 0 \\ 0 & m_d k_d d_d w_d \times \exp(m_d L_d) & -m_d k_d d_d w_d \times \exp(-m_d L_d) & L_c m_g k_g d_g / 2 + L_g h_g w_d \\ \cosh(m_m L_m) & -1 & -1 & 0 \\ 0 & -\exp(m_d L_d) & -\exp(-m_d L_d) & 1 \end{bmatrix} \times \begin{bmatrix} Z_1 \\ Z_2 \\ Z_3 \\ Z_4 \end{bmatrix} = \begin{bmatrix} 0 \\ P/2 \\ 0 \\ 0 \end{bmatrix} \tag{6-13}$$

The channel temperature is $T_c = T_g(x_g = 0) = Z_4 + T_0$. The temperature of the FET-interconnect contact, i.e., the largest temperature in the interconnect, is $T_m(x_m = 0) = Z_2 + Z_3 + T_0$. The channel-to-substrate thermal conductance is $G = P / (T_c - T_0) = P / Z_4$. The channel-to-substrate thermal *resistance* is $R_c = 1 / G = Z_4 / P$.

This result neglects the temperature dependence of the thermal conductivities in the fins. The error in the channel-to-substrate thermal conductance due to this approximation increases with $T_c - T_0$, which is proportional to the device power. This error is estimated for different substrate temperatures by comparing the conductances calculated using thermal conductivities for the temperature $T_0$ with those calculated using thermal conductivities for

the temperature $T_c$. For $T_c - T_0 = 25$ K, the relative changes in the conductance are 2.5 percent, 11 percent, and 38 percent for $T_0 = 300$ K, 77 K, and 50 K, respectively. While the error is small at room temperature, it can be very important if precise calculations are required at low temperatures.

### 6.2.2 Application to the Experimental Test Structure

This section determines the values of the parameters to be used in the thermal model, i.e., the thermal conductivities and dimensions, when predicting the test-structure channel temperature. It shows that the heat transfer to the ambient air from the test structure is negligible.

**Thermal Conductivities.** The thermal conductivities of layers can differ from those of the same material in bulk form due to (a) the boundary scattering of heat carriers, (b) a process- or thickness-dependent microstructure, and (c) thermal boundary resistance. Chapter 5 measures the thermal conductivity of implanted silicon-dioxide layers in SOI wafers near room temperature. The data agree within the experimental error with values recommended for bulk amorphous silicon dioxide (Sugawara, 1969), so the bulk values are used here. The thermal conductivity of the additional silicon dioxide layers, which are thermally grown or are fabricated using LPCVD, are approximated here by the bulk values because a systematic study of the thermal conductivity of thermally-grown silicon dioxide layers has not been reported. Chapter 5 showed that $k_{n,eff}$ for LPCVD silicon dioxide layers can be somewhat less than $k_{bulk}$, which results in a very small error in the heat flow through the interconnects and in the predicted channel temperature because the test structures have relatively large channel-interconnect separations.

The source and drain of the test structure are single-crystal silicon doped with approximately $1 \times 10^{20}$ arsenic atoms cm$^{-3}$. While the layers possess some dislocations due to the implantation of the silicon dioxide layer (Celler and White, 1992), these are

separated by a distance much larger than the phonon mean free path, and are not expected to reduce the thermal conductivity. Boundary scattering can reduce the conductivity in these layers below 77 K, but this effect is negligible above 300 K. The best available data are for bulk single-crystal silicon doped with 1.7 x $10^{20}$ phosphorus atoms $cm^{-3}$ (Touloukian et al., 1970a). The thermal conductivity of doped silicon is governed by the scattering of phonons on the free carriers, not on the dopant atoms, so that the use of data for phosphorus-doped silicon is appropriate for the arsenic-doped silicon in the test structure. The relative uncertainty in $k_d$ is estimated to be 0.2 due to the uncertainty in the doping concentration in the source, drain, and gate. Transmission electron microscopy of a 0.2 μm doped polysilicon layer indicates that the grain length in the plane of the layer is similar to the layer thickness after annealing (Marcus and Sheng, 1983). Because $d_g$ is much greater than the phonon mean free path in heavily-doped silicon above 300 K, the grains are assumed not to affect the thermal conductivity. The gate has the same doping level as the source and drain, yielding $k_g = k_d$. The thermal conductivity above 300 K of silicon with less than $10^{18}$ dopant-atoms $cm^{-3}$ differs little from that recommended for intrinsic silicon (Touloukian et al., 1970a), which is used here for the channel conductivity $k_c$ and the substrate conductivity $k_{sub}$.

The thermal conductivity of aluminum layers containing 1 mass percent of silicon has not been measured directly. The thermal conductivity calculated using the Wiedemann-Franz law (Kittel, 1986) and the electrical resistivity of these layers is within 4 percent of the thermal conductivity recommended for bulk aluminum (Touloukian et al., 1970a), so the bulk value is used here. Boundary scattering in the aluminum interconnects is negligible above room temperature.

The substrate temperature during the measurements is $T_0 = 303$ K, and the largest channel temperature is $T_c = 433$ K. The thermal model developed in Section 6.2.1 neglects the temperature dependence of the thermal conductivities of the SOI FET materials. This is a good approximation between 303 and 433 K for silicon dioxide and aluminum, whose

bulk thermal conductivities vary by less than 13 and 2 percent in this range, respectively. But the thermal conductivity of the heavily-doped silicon source and drain varies more significantly in this temperature range. To help overcome this difficulty, the temperature $(T_0 + T_c) / 2$ is used when interpolating $k_d$ from reported data. So that a single value of $k_d$ may be used, $(T_0 + T_c) / 2$ is averaged for all of the data, yielding 349 K.

**Dimensions.** Figure 6-2 compares the experimental test structure with a FET device. The dimensions of the test structures are given in Table 6-2. Some of these are different from those of a device in an integrated circuit, given in Table 1-1. The interconnect lengths are very long compared to $1/m_m$, so that $L_m = \infty$ is used. The gate of the FET in the test structure extends out from both sides of the channel to interconnect

Table 6-2 Test-structure dimensions. The dimensions given in ranges varied among the test structures.

| Dimension | Symbol | Value or Range (μm) |
|---|---|---|
| Implanted-$SiO_2$ Thickness | $d_o$ | 0.293 - 0.503 |
| Additional-$SiO_2$ Thickness | $d_e$ | 0.6 |
| Interconnect Thickness | $d_m$ | 1 |
| Device Thickness | $d_d$ | 0.041 - 0.177 |
| Gate Thickness | $d_g$ | 0.29 |
| Gate-Channel Separation | $d_{go}$ | 0.0055 |
| Channel-Interconnect Separation | $L_d$ | 0.8 - 3.8 |
| Channel Length | $L_c$ | 0.32 |
| Device Width in $Y$ direction | $w_d$ | 10 |
| Channel-Gate Contact Separation | $w_e$ | 2 |

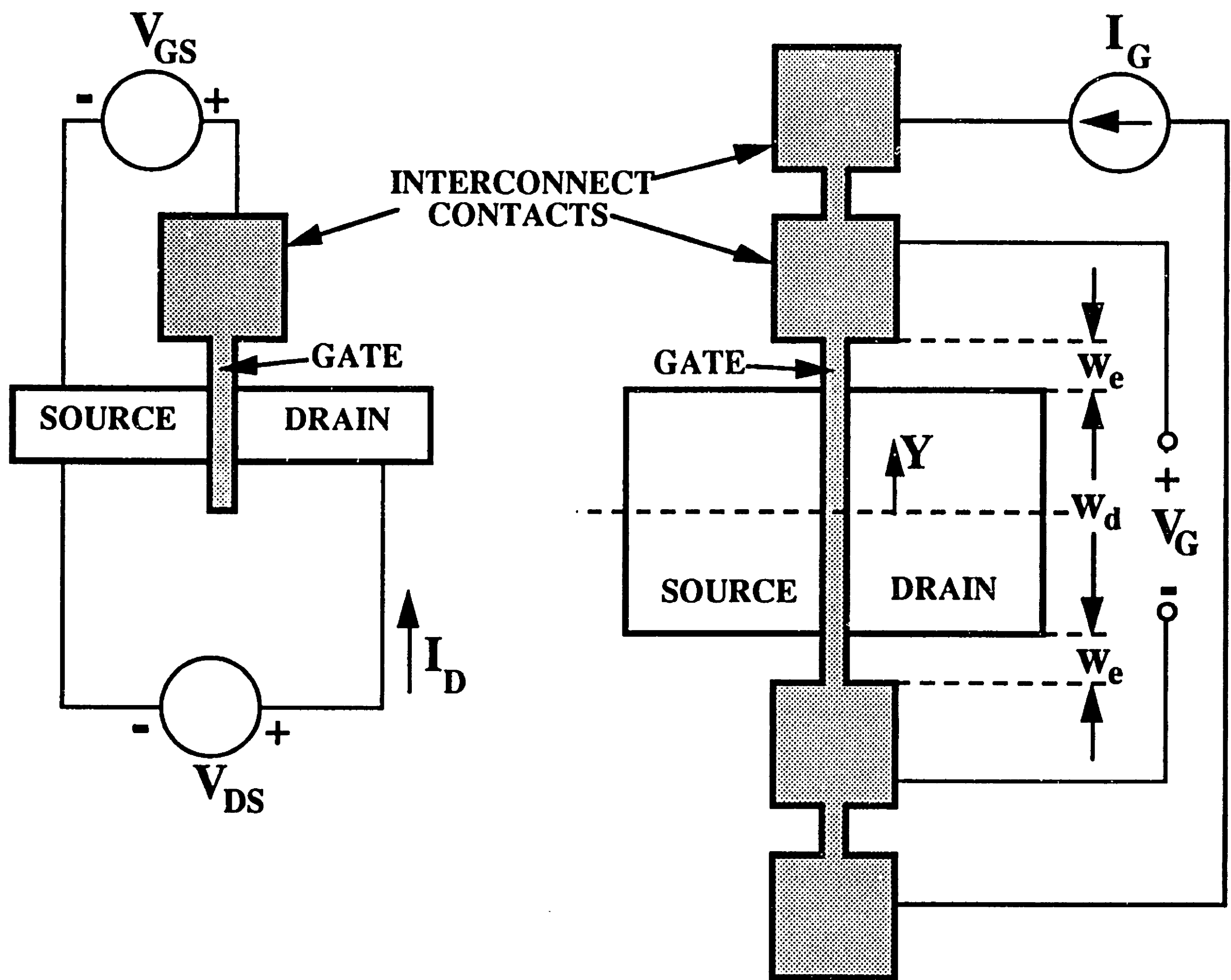


Fig. 6-2 Top views of: a) FET device. b) Test structure.

contacts in the $Y$ direction. This results in a plane of symmetry in the $X$ direction. The temperature field in *each half* of the test structure is predicted by the thermal model. The thermal analysis is applied using $w_d = (w_d)_{\text{test structure}} / 2, w_m = (w_m)_{\text{test structure}} / 2$, and $P = (P)_{\text{test structure}} / 2$.

**Parameter Uncertainties.** An error in the predictions of the thermal analysis results from the use of parameters, e.g., thermal conductivities and dimensions, which are different from those in the test structure. This error is investigated using the sum-of-squares technique (Holman, 1984) and the analytical model. The largest expected error is +/- 10 percent. The uncertainties in $k_d$ and $d_d$ are the largest contributors.

**Heat Transfer to Ambient Air.** The test structure is exposed to ambient air, but heat transfer to the air is neglected. This is justified by the small value of the channel-to-air thermal conductance compared to the channel-to-substrate thermal conductance, which is predicted in this work to be $G \sim 0.5 - 2 \times 10^{-4}$ W K$^{-1}$. The channel-to-air thermal conductance is of the order of that from an isothermal disc of radius $b$ on the boundary of a semi-infinite medium of conductivity $k$, $G = 4b\,k$ (Carslaw and Jaeger, 1959). Using $b = w_d/2$ and the room-temperature conductivity of air yields $G = 5.2 \times 10^{-7}$ W K$^{-1}$. An order-of-magnitude analysis of the momentum equation estimates the air velocity near the device due to buoyancy forces (Rohsenow and Choi, 1961). The air velocity is of the order of $v_a = \rho g b^2 \beta (T_c - T_0)/\mu$, where $g$ is the acceleration due to gravity, and $\rho$ is the density, $\mu$ is the viscosity, and $\beta \sim 1/T_0$ is the approximate coefficient of thermal expansion of the air. Using room-temperature properties and $T_c - T_0 = 130$ K yields $v_a = 6.6$ μm s$^{-1}$. The thermal conductance contributed by the air motion is of the order of $G = v_a\ \pi b^2 \rho\, c_p = 6.2 \times 10^{-13}$ W K$^{-1}$, where $c_p$ is the specific heat per unit mass at constant pressure of air, which is much smaller than $G$ for conduction. The thermal conductance due to radiation is of the order of $G = 4\,\varepsilon\,\sigma T_0^3\,A$, where $\varepsilon$ is the emissivity

of the surface, $\sigma$ is the Stefan-Boltzmann constant, and $A$ is the area of the emitting surface. Using $\varepsilon = 1$ and $A = \pi b^2$ yields $G = 5.0 \times 10^{-10}$ W K$^{-1}$ at room temperature. The channel-to-air thermal conductances are very small compared to those for conduction to the substrate, showing that heat transfer to the air may be neglected.

### 6.2.3 Influence of Heat-Carrier Boundary Scattering

Boundary scattering reduces thermal conduction in a medium when the mean free path of the carriers of heat is of the order of or larger than the smallest medium dimension. Thermal conduction processes for which this significantly changes the heat flux are called *microscale* in Chapter 2. This section determines the temperature-dependent mean free path of heat carriers in each SOI circuit material, and compares it with the dimensions of the circuit components made from that material. Theory for the thin-layer conduction size effect yields the reduced effective conductivities of these circuit components, which in the following section are used to calculate temperature distributions in the device and interconnects.

Electrons are the dominant carriers of heat in the aluminum interconnects. Phonons are the dominant carriers of heat in silicon and silicon dioxide. For each medium, Eq. (2-1) relates the mean free path $\Lambda$ of the dominant heat carrier to the specific heat due to that carrier per unit volume $C$, the thermal conductivity $k$, and the speed of the carrier $v$. When applying Eq. (2-1) to aluminum, $C = C_e = (135 \text{ J m}^{-3} \text{ K}^{-2})\, T$ is the electron specific heat per unit volume, where $T$ is the temperature, $v = v_e = 2.0 \times 10^6$ m s$^{-1}$ is the electron Fermi velocity (Kittel, 1986), and $k = k_m$ is the temperature-dependent thermal conductivity (Touloukian et al., 1970a).

When applying Eq. (2-1) to the doped-silicon source, drain, and gate, $k$ is the phonon conductivity, $v = v_s$ is the phonon velocity, well approximated by the speed of sound in silicon, and $C = C_s$ is the phonon specific heat per unit volume. The source and drain of the FET are doped single-crystal silicon. The thermal conductivity of the gate

differs from that of single-crystal doped silicon only when the conduction is also reduced by scattering on the boundaries of the gate. To simplify the present analysis, the scattering of phonons on the gate boundaries is assumed to dominate over the scattering on grain boundaries within the gate. The phonon thermal conductivity and mean free path decrease with increasing carrier concentration in doped semiconductors. In order to estimate the largest effect of boundary scattering on cooling of the FET, thermal conductivity data for silicon with a concentration of dopant atoms of 2.0 x $10^{19}$ phosphorus atoms $cm^{-3}$ are employed (Touloukian et al., 1970a). This is a lower doping concentration than is used for the test structure in Section 6.2.2, resulting in a larger thermal conductivity and longer phonon mean free paths. The experimental specific heat, which varies little with doping concentration, is given by Touloukian and Buyco (1970a), and the speed of sound is $v_s = 6400$ m $s^{-1}$.

The mean free path of phonons in silicon dioxide calculated using Eq. (2-1) is less than 1 nm. But Section 5.2 shows how the strong frequency dependence of phonon free paths in amorphous materials makes possible a conduction size effect in a layer even when the *mean* free path is much smaller than the layer thickness. Section 5.2 determined the effect of phonon-boundary scattering on thermal conduction normal to amorphous silicon dioxide layers. For 0.4 μm layers, the thermal conductivity normal to the layer is reduced by less than 3 percent at 300 K, 9 percent at 77 K, and 29 percent at 45 K. These size effects are overwhelmed by those in the source and drain, and are neglected here for simplicity.

Values of the thermal conductivity used in the boundary-scattering analysis are given in Table 6-3. The mean free paths of electrons in aluminum and phonons in doped silicon are shown in Fig. 6-3. Since a SOI FET may eventually be as thin as 0.03 μm and interconnects can be as thin as 0.5 μm, boundary scattering must be considered, particularly in the source and drain and at low temperatures. Carrier-boundary scattering has the greatest impact on thermal conduction in the source and drain of the device.

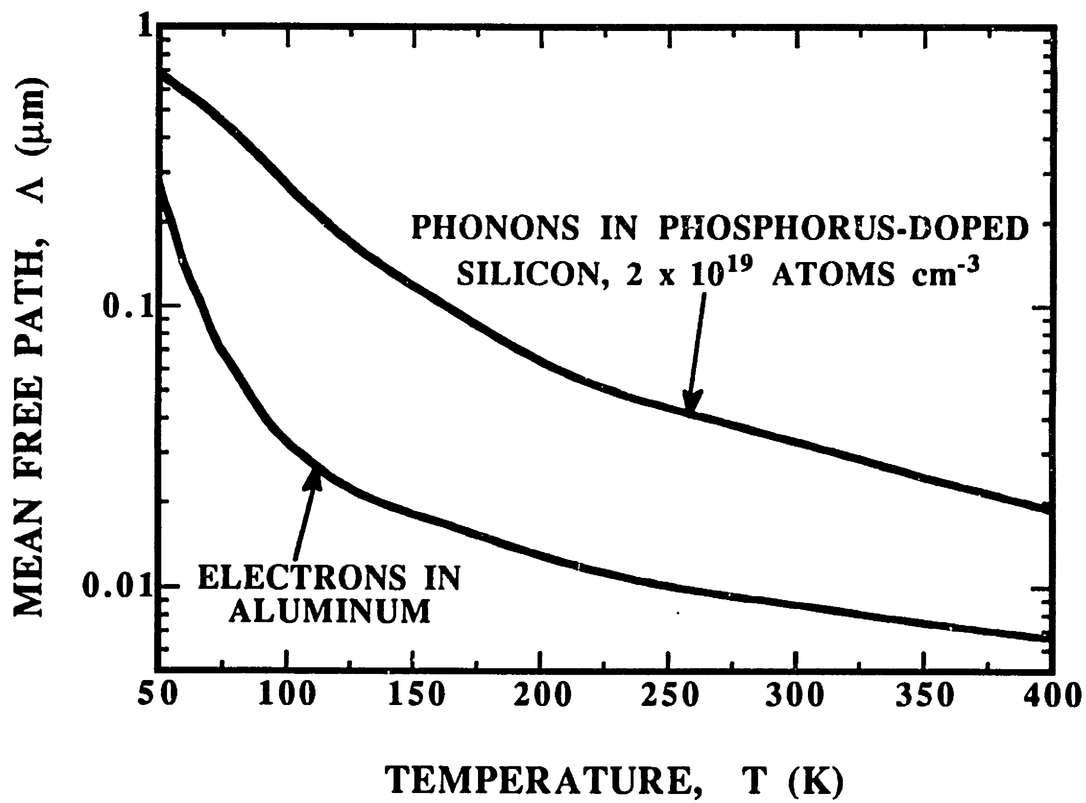


Fig. 6-3 Mean free paths of heat carriers in SOI circuits.

Table 6-3 Thermal conductivities used to determine the effect of boundary scattering. These were recommended by Touloukian et al. (1970a; 1970b).

| Temperature | $k_d = k_g$ ($W\,m^{-1}\,K^{-1}$) | $k_m$ ($W\,m^{-1}\,K^{-1}$) | $k_o$ ($W\,m^{-1}\,K^{-1}$) |
|---|---|---|---|
| 50 K | 256 | 1230 | 0.34 |
| 77 K | 373 | 449 | 0.53 |
| 300 K | 120 | 237 | 1.40 |

Flik and Tien (1990) developed an approximate theory for the reduction of the thermal conductivity along a layer as a function of the ratio of the layer thickness to the carrier mean free path, $\delta = d/\Lambda$. For $\delta > 1$,

$$\frac{k_{a,eff}}{k_{bulk}} = 1 - \frac{2}{3\pi\delta} \tag{6-14}$$

where $k_{a,eff}$ is the effective conductivity along the thin layer and $k_{bulk}$ is the bulk conductivity. For $\delta < 1$,

$$\frac{k_{a,eff}}{k_{bulk}} = 1 - \frac{2\left(1-S^3\right)}{3\pi\delta} + \frac{2\delta}{\pi}\ln\left[\frac{1+\delta+S}{1+\delta-S}\right] - \frac{2}{\pi}\arccos(\delta) \tag{6-15}$$

where $S = (1-\delta^2)^{1/2}$. Equation (6-14) is used to determine the *microscale* thermal-conduction regime for conduction along layers in Chapter 2. The thermal model of Section 6.2.1 is adapted to account for boundary scattering by calculating $k_{a,eff}$ at each temperature using Eqs. (6-14) and (6-15) for the source, drain, gate, and interconnect fins. The mean free paths are given in Fig. 6-3 and $k_{bulk}$ is given in Table 6-3. Equations (6-10) - (6-13)

are then assumed to yield the temperature distribution in the FET and interconnects when the reduced conductivities are used for each fin.

Equations (6-14) and (6-15) were derived by assuming that carrier scattering on the top and bottom boundaries of the film is diffuse, and by neglecting the transmission of carriers through the boundaries. The use of Eqs. (6-14) and (6-15) also neglects carrier scattering on the side boundaries of a bridge, i.e., on those boundaries parallel to the $Z$ direction in Fig. 1-2. This is important if the ratio of the carrier mean free path and the microbridge width is of the order of or greater than unity. The doped silicon source and drain and aluminum interconnect widths are 0.8 μm, and the doped polysilicon gate width is 0.5 μm. This condition is satisfied in the interconnects above about 70 K, in the source and drain above about 180 K, and in the gate above about 230 K. Below these temperatures, Eqs. (6-14) and (6-15) overpredict the effective conductivity of the bridge and result in an underestimate of the effect of boundary scattering.

## 6.3 Channel-Temperature Measurement Technique

This section develops the technique for measuring the channel temperature of SOI FETs. Section 6.3.1 describes the apparatus and the general procedure, and Section 6.3.2 calculates the channel temperature from the measured gate electrical resistance. Section 6.3.3 determines the experimental uncertainty.

### 6.3.1 Apparatus and Procedure

Fig. 6-2 shows the experimental test structure. The electrical resistance of the gate depends strongly on temperature. It serves as an electrical-resistance thermometer. The calibration consists of measuring the gate electrical resistance, $R_G$, as a function of temperature when there is no drain current, i.e., when the gate is isothermal, yielding $[R_G(T)]_{calibration}$. The substrate temperature is controlled using a Temptronic Model TP38B chuck, a copper disk with a diameter of 88.9 mm and a thickness of 19.1 mm, to which a

wafer is secured by suction. A thermocouple with one junction soldered to the chuck surface measures the chuck temperature. The chuck is maintained at the temperature $T_0$ and the gate resistance is measured for varying values of the drain-source voltage drop, $V_{DS}$, and the gate-source voltage drop, $V_{GS}$, i.e., for several different device powers, $P = I_D V_{DS}$.

The *average gate temperature* is defined here as that of the gate segment whose resistance is measured, i.e., the segment between the voltage contacts. The average temperature in the channel is $T_c$, which is shown in Section 6.2.1 to be very well approximated by the average temperature of the gate segment over the channel. The average gate temperature is influenced by the gate segments not over the channel heater, and is less than $T_c$.

Mautry et al. (1990) applied a technique similar to the one developed here to bulk FETs, which do not have an implanted silicon-dioxide layer. The channel temperature was obtained from $R_G$ by inverting the calibration function, $[R_G(T)]_{\text{calibration}}$. This approach ssumed that the average gate and average channel temperatures were equal. This underestimated $T_c$, but the error was not assessed. The FET gate-temperature variation is more important in a SOI wafer, where most of the temperature drop occurs within a few micrometers of the channel due to the implanted layer, than in a normal substrate, where the temperature-drop lengthscale is the thickness of the substrate, i.e., a few hundred micrometers. This temperature variation must be considered when calculating $T_c$ from $R_G$.

### 6.3.2 Temperature Distribution in the Gate

This section calculates $T_c$ from the data for $R_G$. Temperature variations in the $X$ and $Z$ directions in the gate are neglected. The gate temperature is

$$T_G(Y) = \Delta T_G \, F_G(Y) \tag{6-16}$$

where $\Delta T_G$ is the average gate-temperature rise from $T_0$, and $F_G(Y)$ is a shape function defined for $|Y| < w_e + w_d/2$ whose average value is unity. For each measured $R_G$, $\Delta T_G$ is determined iteratively using the shape function and

$$R_G = \int_{-w_e - w_d/2}^{w_e + w_d/2} \left[ R_G\left( T_0 + \Delta T_G \, F_G(Y) \right) \right]_{\text{calibration}} \frac{\mathrm{d}Y}{2w_e + w_d} \tag{6-17}$$

The thermal resistance of the silicon-dioxide layer between the channel and gate, $d_{go}/(L_c w_d k_o) = 1.2 \times 10^3$ K W$^{-1}$, is small compared to the thermal resistance for conduction along the gate to the contact in the $Y$ direction, $w_e/(L_c d_g k_g) = 3.3 \times 10^5$ K W$^{-1}$. This means that the channel- and gate-temperature distributions are almost identical for $|Y| < w_d / 2$. The average channel temperature is

$$T_c = T_0 + \int_{-w_d/2}^{w_d/2} \Delta T_G \, F_G(Y) \frac{\mathrm{d}Y}{w_d} \tag{6-18}$$

The channel-to-substrate thermal resistance is $R_c = (T_c - T_0) / P = (T_c - T_0) / (I_D V_{DS})$.

This section now develops two shape functions, from which Eqs. (6-17) and (6-18) yield upper and lower bounds for $T_c$ for a given $R_G$. Each shape function is even, due to the symmetry of the test structure about $Y = 0$, and continuous. Because of the large width in the $X$ direction of the gate-interconnect contacts, 4 μm, compared to the gate width, $L_c = 0.32$ μm, the contacts are very nearly isothermal at the substrate temperature, $T_0$. This yields the boundary conditions $F_G(Y) = 0$ at $Y = +/- (w_e + w_d / 2)$. The shape function has an average value of unity between these boundaries. For a given $R_G$, $T_c$ calculated using Eqs. (6-17) and (6-18) increases with the difference between unity and the average of $F_G(Y)$ for $-w_d / 2 < Y < w_d / 2$, i.e., with the assumed difference between the average gate and channel temperatures.

Shape LB in Fig. 6-4 assumes a linear temperature profile in the gate segments not over the channel, which neglects conduction down through the buried-silicon-dioxide layer, and an isothermal channel. Both of these assumptions underestimate the difference between the average channel and average gate temperatures, yielding a lower bound for $T_c$. Shape LB is

$$F_G(Y) = \frac{w_d + 2w_e}{w_d + w_e} \quad , \quad |Y| < \frac{w_d}{2} \tag{6-19}$$

$$F_G(Y) = \left[\frac{w_d + 2w_e}{w_d + w_e}\right] \frac{[(w_e + w_d/2) - |Y|]}{w_e} \quad , \quad \frac{w_d}{2} < |Y| < w_e + \frac{w_d}{2} \tag{6-20}$$

An overestimate of the difference between the average gate and channel temperatures requires an overestimate of the temperature drop from the center to the edge of the channel in the $Y$ direction. This is calculated by isolating the channel and gate from the source and drain, whose wide cross sections in the $X$-$Z$ plane reduce the channel-temperature variation in the $Y$ direction. The gate and channel are grouped together as a composite fin which meets a fin of different cross section and heat transfer coefficient at $Y = w_d/2$. Solving the heat equation in the two fins yields shape UB in Fig. 6-4 for typical dimensions in the test structure. Shape UB has a larger average in the channel region than shape LB. Values of $T_c - T_0$ calculated using shapes UB and LB differ by less than 8 percent, and the simpler shape LB is used here, Eqs. (6-19) and (6-20). This function does not describe the temperature distribution in the channel. Rather, it is a shape function which, when used in Eqs. (6-17) and (6-18), yields a value for $T_c$ close to the actual average channel temperature. The difference between the upper and lower bounds is used in the experimental-uncertainty analysis.

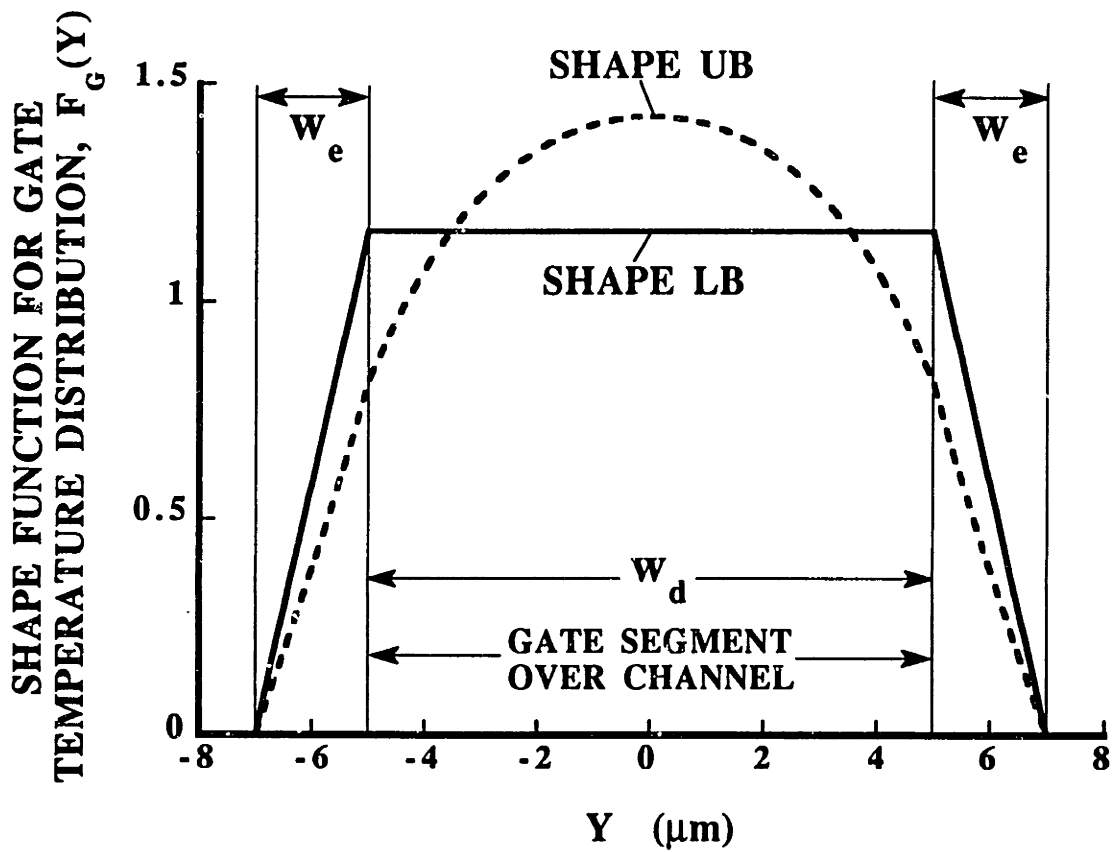


Fig. 6-4 Shape functions for the gate-resistor temperature distribution. Shape LB, given by Eqs. (6-19) and (6-20), yields a lower bound for $T_c$. Shape UB is calculated by isolating the gate and channel from the source and drain, as discussed on p. 153, which yields an upper bound for $T_c$.

### 6.3.3 Experimental Uncertainty

The uncertainty in $R_c = (T_c - T_0) / P$ has three independent components. (a) There is a relative uncertainty of 0.04 in $T_c - T_0$ due to the error in the substrate-temperature change measured by the chuck thermocouple. (b) A relative uncertainty of 0.066 in $T_c - T_0$ is due to the measurement of $R_G$. (c) A relative uncertainty of 0.08 in $T_c - T_0$ is due to the approximate shape function for the temperature profile in the gate, as shown in Section 6.3.2. The total relative uncertainty in $R_c$ is +/- 0.11, determined using the sum-of-squares technique (Holman, 1984).

## 6.4 Results and Discussion

### 6.4.1 Comparison of Measurements and Analysis

Channel-temperature measurements are performed on SOI test structures with varying values of $L_d$, $d_d$, and $d_o$. Test structures fabricated from conventional (not SOI) wafers are measured for comparison. The device voltages satisfy 0 V < $V_{DS}$ < 3 V and $V_{GS}$ = 2 V and 2.5 V, which are typical operating conditions. The device powers vary between 3 and 14 mW, and the values of $T_c - T_0$ vary between 5 and 130 K.

The channel-to-substrate thermal resistance, $R_c$, varies by less than the experimental uncertainty for varying powers from a single device, as is shown in Fig. 6-5 for three SOI devices and one conventional device. The data for each device for varying powers fall near a line originating at $P = 0$ and $T_0 = 303$ K, whose slope is $R_c$. The conventional device, which is in close thermal contact with the silicon substrate, has the lowest value of $R_c$. Values of $R_c$ for the SOI devices are as much as 10 times larger than $R_c$ for the conventional device, due to the thermal resistance of the implanted silicon dioxide layer. The value of $R_c$ decreases with the thickness of the SOI devices, because this increases the heat flow into the source and drain fins. In what follows, each data point is the average of the values of $R_c$ measured in a single test structure.

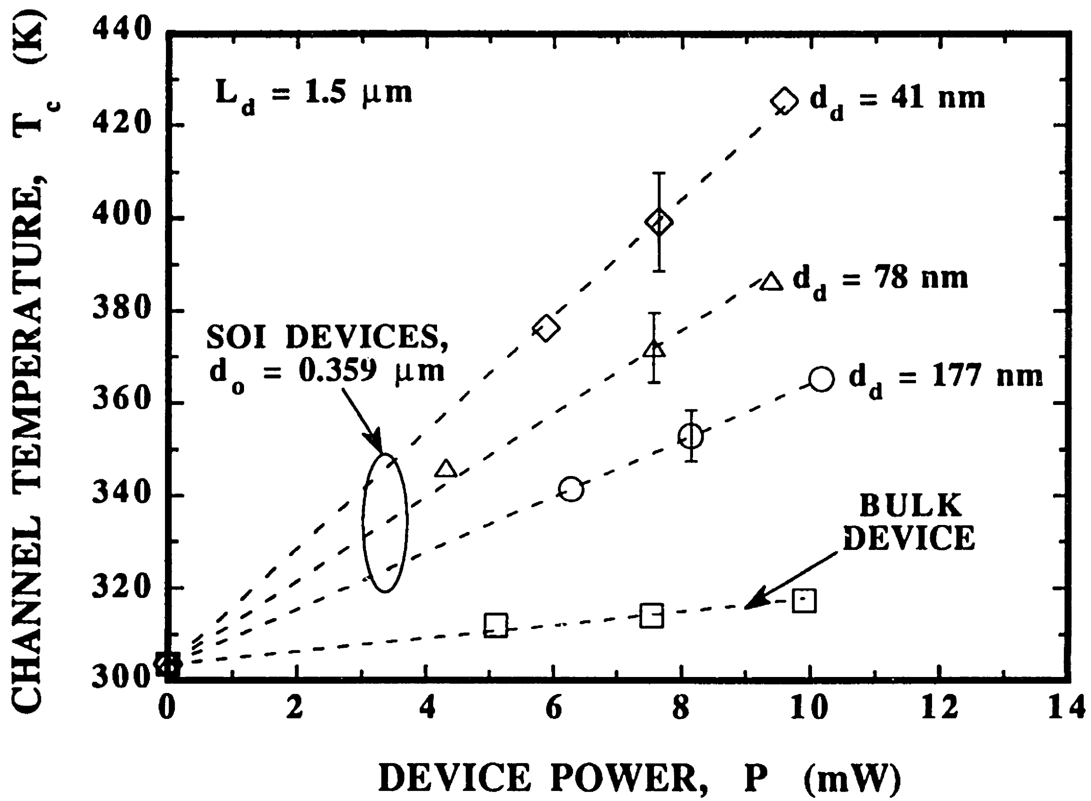


Fig. 6-5 Channel-temperature data for SOI FETs with varying device thicknesses, compared with data for a bulk (non SOI) FET.

Figure 6-6 shows that the sensitivity of $R_c$ to the device thickness is predicted by the thermal model from Section 6.2.1. The predictions agree well with the data, considering the +/- 10 percent theoretical error due parameter uncertainties, and show that increasing $d_d$ reduces the channel temperature for a given power. Examination of Eq. (6-13) shows that $k_d$ and $d_d$ are not independent, but always appear as a product in the solution for the temperature distribution. Thus, the channel temperature is also sensitive to $k_d$, which depends on the doping level in the source and drain. Decreasing the dopant concentration in silicon from $1.7 \times 10^{20}$ to $2.0 \times 10^{19}$ $cm^{-3}$ increases the thermal conductivity at 300 K by 60 percent (Rowe and Bhandari, 1986). This results in a substantial decrease in $R_c$, particularly for thin devices, i.e., $d_d < 50$ nm. But the electrical conductivity *decreases* as the dopant-atom concentration is decreased, which increases the voltage drop and the Joule heating in the source and drain. The benefits of increasing $k_d$ could be offset by the additional power dissipated in the source and drain. The thermal design of SOI FETs should optimize the concentration of dopant atoms considering heat conduction in the source and drain.

Figure 6-7 shows the dependence of $R_c$ on the implanted-silicon-dioxide layer thickness. The data support the predictions of the model, and indicate that $R_c$ is as sensitive to $d_d$ as it is to $d_o$. This is in contrast to the predictions of McDaid et al. (1989), whose model assumed that $R_c$ is independent of $d_d$. By modeling one-dimensional conduction in the implanted-silicon-dioxide layer, these researchers predicted that $R_c = d_o / (A\ k_o)$, where $A$ is the device area in the $X$-$Y$ plane. This neglects the spreading of the temperature profile into the source and drain fins with increasing $d_o$, and is not consistent with the data. This can be remedied by a simple scaling analysis. The area in the source and drain with significant temperature rise is of the order of $A = 2w_d / m_d$, where the thermal healing length $1/m_d$ is approximately $(k_d\, d_d\, d_o / k_o)^{1/2}$. Using $R_c = d_o / (Ak_o)$ with this expression for $A$ yields

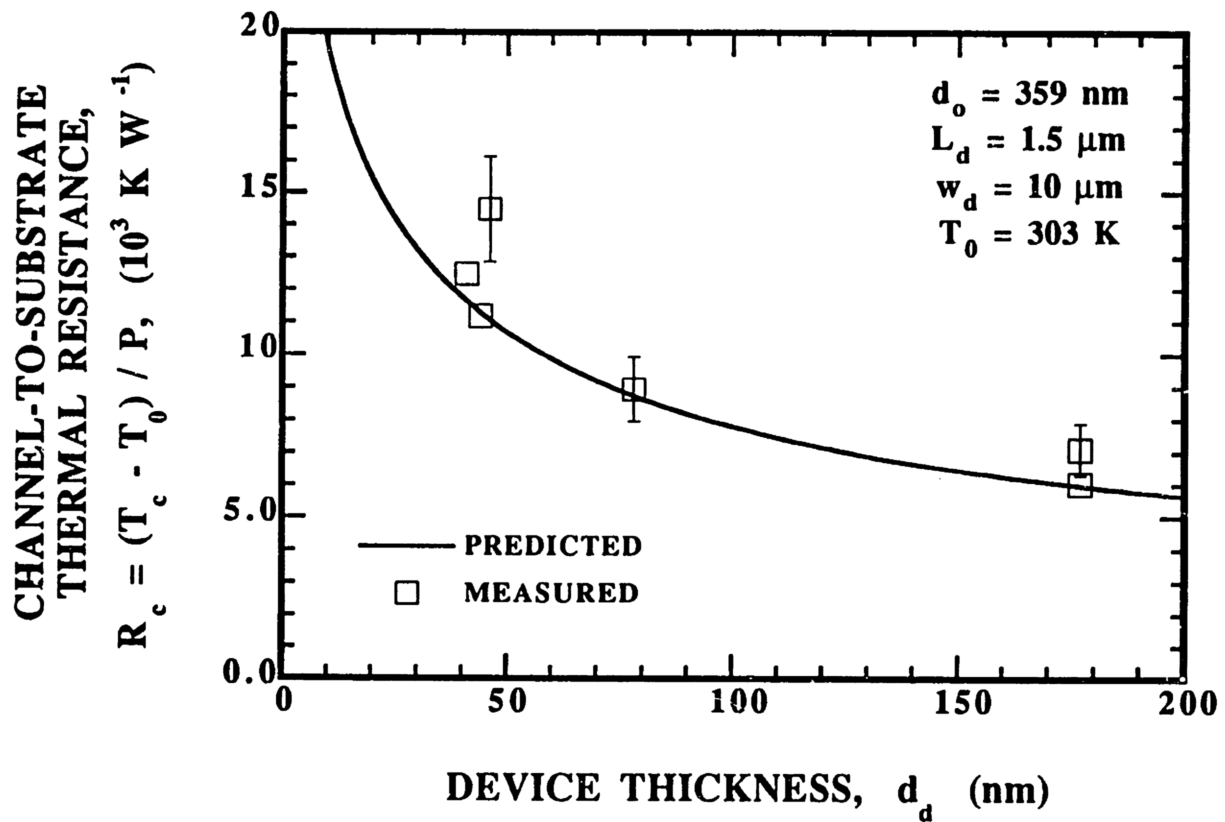


Fig. 6-6 The channel-to-substrate thermal resistance, $R_c$, as a function of the device thickness.

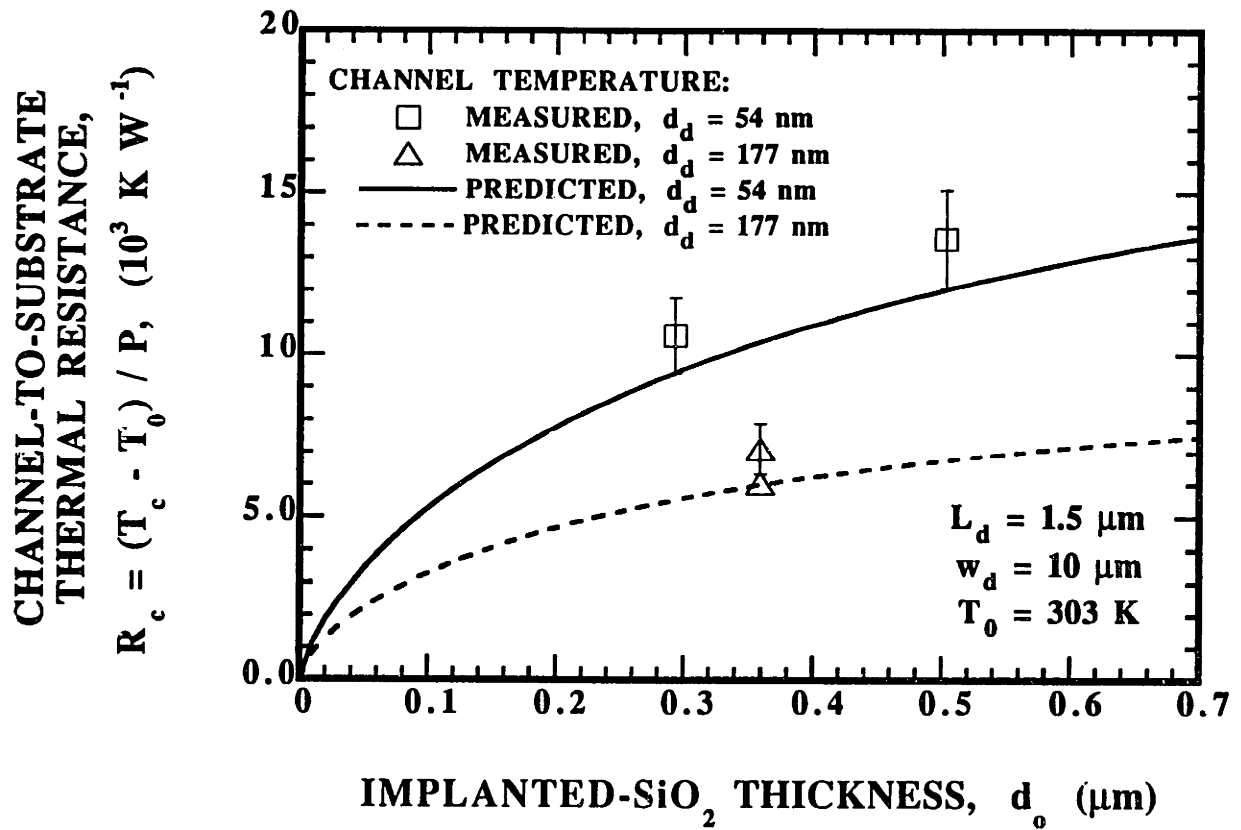


Fig. 6-7 The channel-to-substrate thermal resistance as a function of the implanted silicon-dioxide layer thickness.

$$R_c \approx \frac{1}{2\,w_d}\left(\frac{d_o}{k_o\,k_d\,d_d}\right)^{1/2} \tag{6-21}$$

which is in qualitative agreement with the data in Fig. 6-7. This shows that $R_c$ is roughly proportional to $d_o^{1/2}$, and that the sensitivity of $R_c$ to $d_o$ and $d_d$ is similar, i.e, halving $d_o$ and doubling $d_d$ have the same impact, if all other parameters are held constant. Equation (6-21) assumes the thermal healing length in the source and drain is smaller than the channel-interconnect separation, i.e., $1/m_d < L_d$. Otherwise, there is significant heat conduction into the interconnects, which are more effective fins than the source and drain because of their large thickness and high thermal conductivity.

This is demonstrated in Fig. 6-8, which shows the dependence of $R_c$ on $L_d$. As $L_d$ is decreased, conduction cooling of the channel through the interconnects becomes more important, reducing $R_c$. This approach to reducing the channel temperature becomes less effective if the devices are densely packed, i.e., $L_m$ is of the order of or smaller than $1/m_m$. In contrast to the behavior of the channel temperature, the FET-interconnect contact temperature *increases* as $L_d$ is reduced, because this brings the contact nearer to the channel heat source. This reduces the reliability of a SOI circuit, whose electromigration-limited mean time to failure (MTF) decreases with increasing temperature. It may be possible to improve the reliability of a circuit by increasing $L_d$, but this must be weighed against the need for small devices.

Electromigration limits the median time to failure (MTF) of FET-interconnect contacts. Momentum transfer from electrons to atoms in the interconnect causes the metal atoms to flow in the direction of the electron flow. This can cause voids to grow in the interconnect and can result in open-circuit failure. This is an important problem at FET-interconnect contacts, where the flux of aluminum atoms diverges because of the change of conducting materials. Black (1967) developed an approximate formula for the MTF,

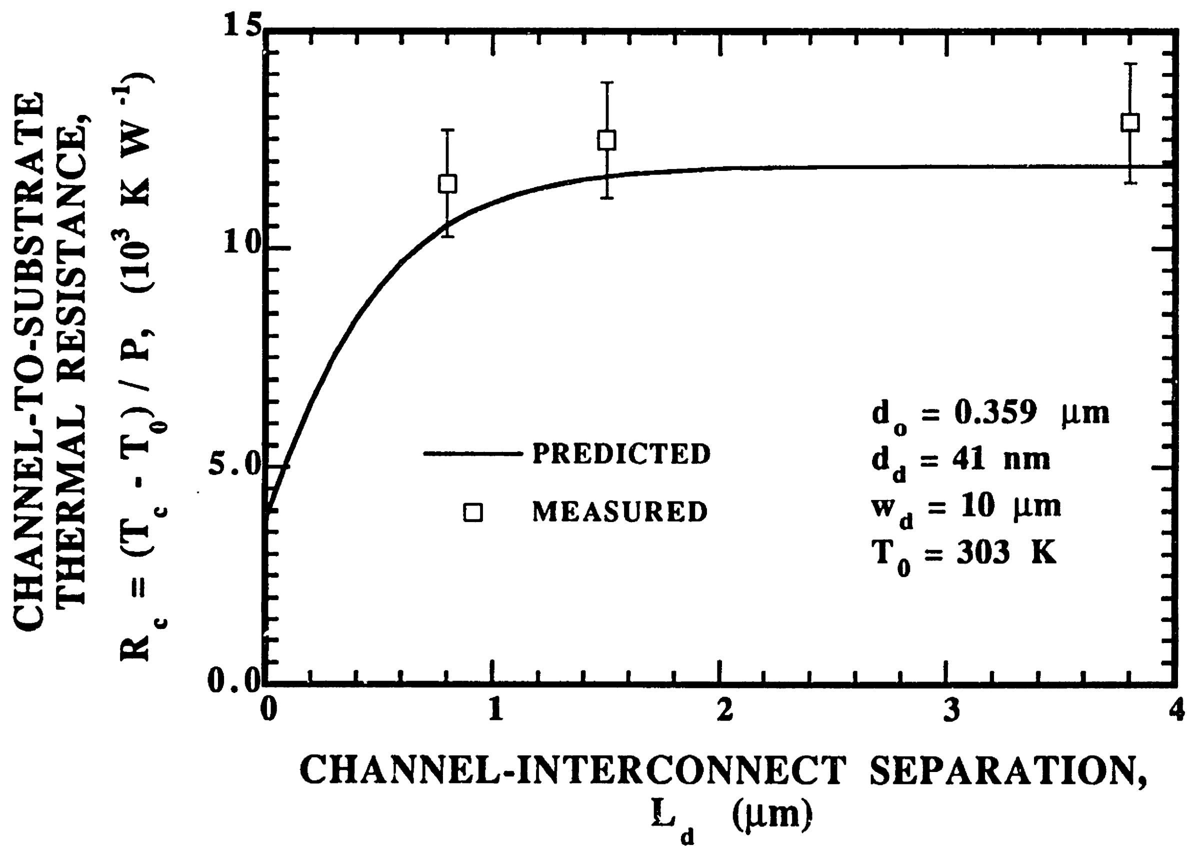


Fig. 6-8 The channel-to-substrate thermal resistance as a function of the channel-interconnect separation.

$$\mathrm{MTF} = K_e\, J^{-2} \exp\left(\frac{E_e}{k_B T}\right) \tag{6-22}$$

where $E_e$ is the activation energy for atomic diffusion, $k_B = 1.38 \times 10^{-23}$ J K$^{-1}$ is the Boltzmann constant, $T$ is the metal temperature, $J$ is the current density, and $K_e$ is a constant. Chern et al. (1986) studied the failure of contacts of heavily-doped silicon with aluminum, and fitted MTF data within a few percent using Eq. (6-22). The variables $K_e$ and $E_e$, and the exponent of the current density were fitting parameters. The present work requires the temperature dependence of the MTF, which is governed by the exponential factor in Eq. (6-22), and uses $E_e = 0.5$ eV $= 8 \times 10^{-20}$ J given by Chern et al. (1986).

The following uses Eq. (6-22) to show how the dimensions of FETs can be chosen to improve the electromigration-limited reliability of a SOI integrated circuit. The FET dimensions in Table 1-1 are used, with an interconnect length between devices of $2L_m = 4$ μm. During steady power dissipation, SOI FETs with these dimensions may dissipate as much as 1.61 W (Woerlee et al., 1989). The FETs are assumed to experience steady-periodic heating and operate for one tenth of each clock cycle. The steady-state thermal model provides a good estimate of the nearly-steady-state FET-interconnect contact if the time-averaged power is used, $P_{ave} = 0.161$ W. The interconnect temperature rise is less than 8 K, but depends strongly on $d_o$ and $L_d$. Figure 6-9 shows the ratio of the MTF for FET interconnect contacts in a SOI circuit to that for contacts in a bulk circuit. These predictions assume that the substrate temperature in the SOI case is equal to that in the bulk case. The difference between the two contact temperatures is due to the thermal resistance of the implanted silicon dioxide layer. The MTF increases as $L_d$ is increased, because the interconnect moves away from the channel heater. Reducing $d_o$ also increases the MTF, because this reduces the contact temperature. Although the temperature rise in the interconnects is only a few degrees Kelvin, the MTF may be increased significantly by the proper choice of device dimensions. Because Eq. (6-22) has only been experimentally verified using accelerated testing, i.e., the use of electrical current densities and

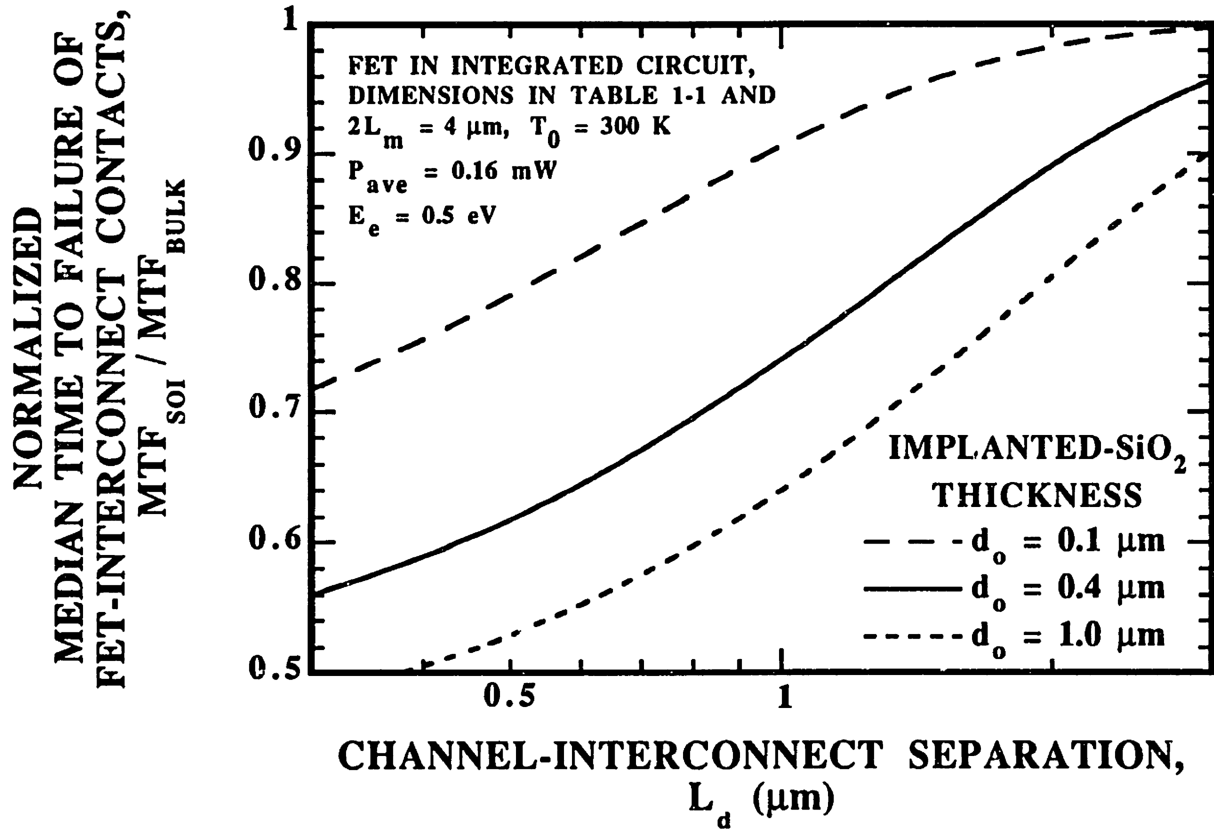


Fig. 6-9 Predicted dependence of the median time to failure (MTF) of FET-interconnect contacts on the channel-interconnect separation.

temperatures which are higher than those in an operating circuit, the predictions in Fig. 6-9 should be taken as very approximate, and are given only to show the expected trends.

### 6.4.2 Influence of Heat-Carrier Boundary Scattering

This section provides an estimate of the impact of heat-carrier-boundary scattering on the channel-to-substrate thermal conductance. The *base case* dimensions for these calculations are those for a FET device given in Table 1-1. The approximate microscale analysis described in Section 6.2.3 yields the results in the figures that follow, i.e., they are calculated using the reduced thermal conductivities given by Eqs. (6-14) and (6-15), unless they are labeled "macroscale," in which case the bulk, unreduced values of the thermal conductivities are used. For the base case with a substrate temperature of $T_0 = 300$ K and a long interconnect length, $L_m m_m >> 1$, the relative importances of the cooling paths for the heat dissipated in the channel are as follows: 19 percent of the heat flows directly from the device through the silicon dioxide layer into the substrate, 25 percent flows out through the gate, and 56 percent flows out through the metal interconnects. The relative importance of the heat flow through the gate decreases if the device width $w_d$ is increased.

Microscale and macroscale predictions of the thermal conductance $G$ are shown in Fig. 6-10. The calculations are for long interconnects, $m_m L_m >> 1$. Macroscale analysis overpredicts the values of the effective thermal conductivity in the fins and therefore overpredicts the thermal conductance. The error of the macroscale prediction is small at room temperature, but increases with decreasing temperature due to the increasing mean free paths of both phonons and electrons. The relative error of the macroscale prediction increases with decreasing device thickness.

The effect of boundary scattering on the packing limit is estimated. Due to the importance of lateral heat conduction, decreasing the separation between devices, $2L_m$, has

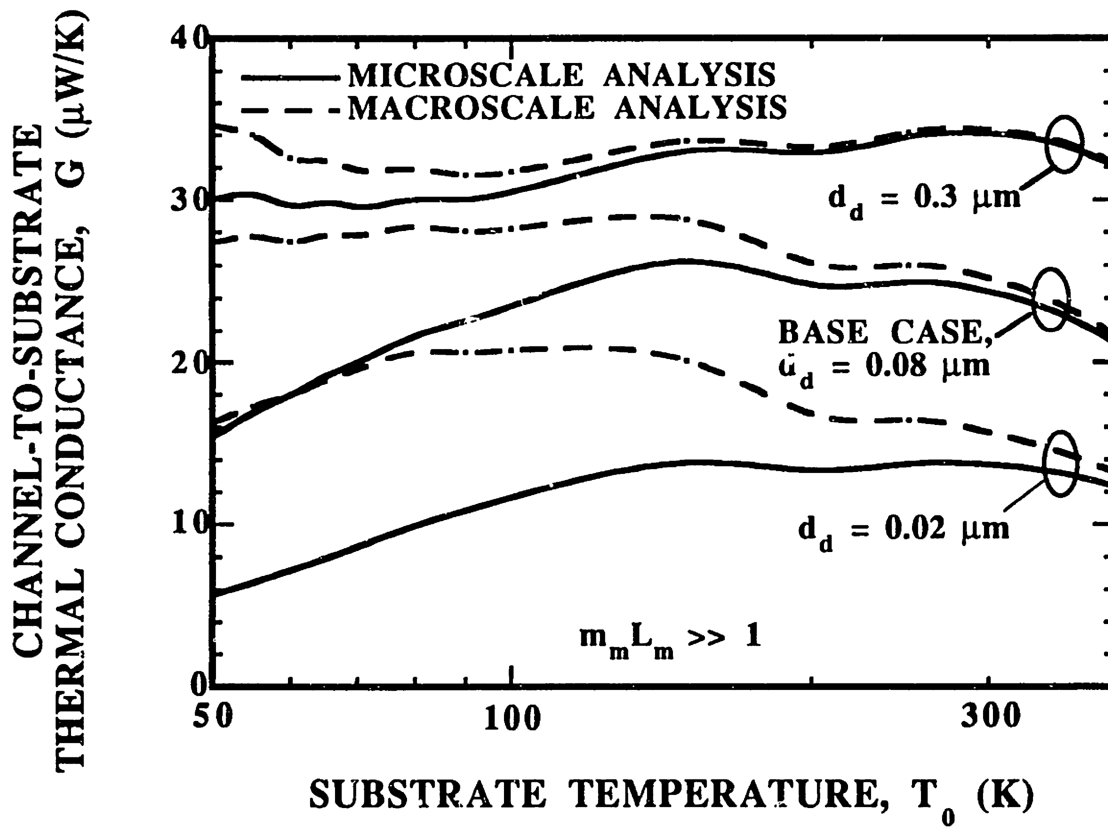


Fig. 6-10 Microscale and macroscale predictions of the channel-to-substrate thermal conductance.

a strong effect on the FET temperature field for a given power. This is illustrated in Fig. 6-11 for varying implanted-layer thicknesses. The channel and FET-interconnect contact temperatures both increase as the device separation is decreased or the implanted layer thickness is reduced. This figure shows clearly the advantages of thinner silicon dioxide layers for reducing the operating temperature of SOI devices and interconnects.

If a designer must achieve a targeted value of the channel-to-substrate thermal conductance, a minimum allowable separation between devices can result. Figure 6-12 shows that microscale and macroscale predictions of the required separation between connected devices vary as a function of the targeted value of $G$. The large slope of the curves for large values of the device separation shows that beyond a certain separation, of the order of the thermal healing length in the metal, $1/m_m$, additional separation does not enhance the heat transfer from the device. This figure indicates that for a given operating temperature and set of FET parameters, there is a limited range of values of $G$ which can be achieved by variation of the device separation alone. It may be impossible to keep the channel temperature below a targeted value without decreasing the device power. The error in the required device separation due to neglecting microscale effects is small at 300 K but increases with decreasing temperature until it is of great importance at 50 and 77 K. The predictions of microscale and macroscale analyses which considered the temperature variation of material thermal properties would differ by less than those of the present analysis because the importance of microscale effects in a given component is reduced as its temperature increases from $T_0$. The present analysis provides an upper bound for the impact of boundary scattering on $G$.

If the separation between devices in the $X$ direction is $2L_m$, taken from Fig. 6-12, and in the $Y$ direction is $W_0 = 10\ \mu\text{m}$, the packing limit $D$ can be estimated using

$$D = \frac{1}{[(2L_m + 2L_d + L_c)(w_d + W_0)]} \tag{6-23}$$

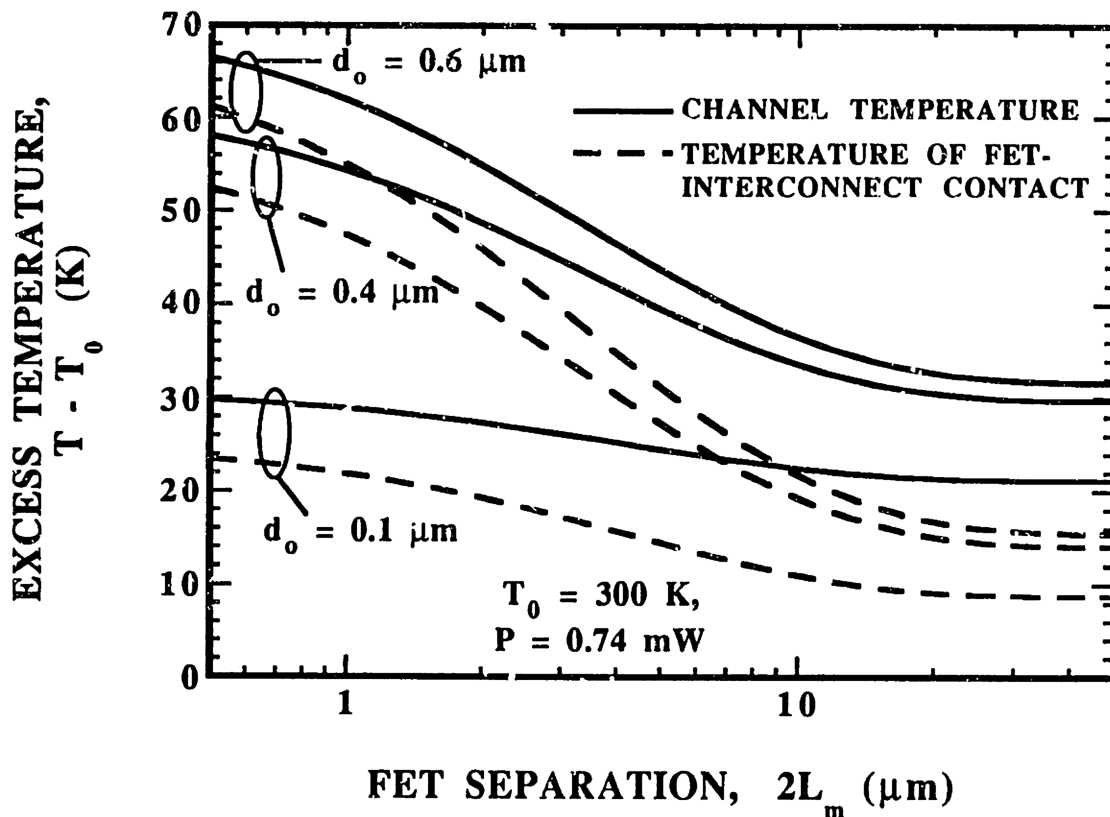


Fig. 6-11 Dependence of the channel temperature and the FET-interconnect contact temperature on the separation between FETs in the *X* direction.

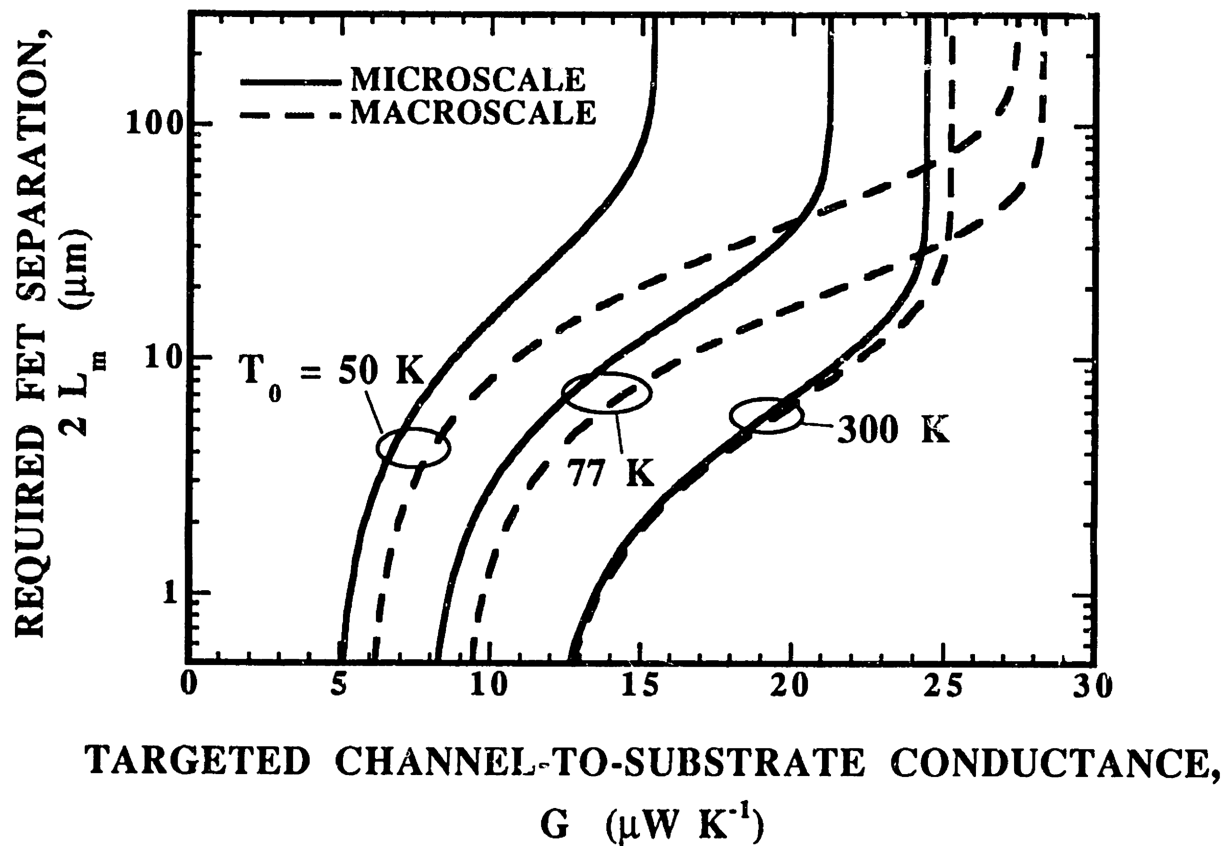


Fig. 6-12 Microscale and macroscale predictions of the FET separation required to achieve a targeted channel-to-substrate thermal conductance.

The error of macroscale predictions of the packing limit is given in Table 6-4. The values of the channel-to-substrate conductance $G$ are chosen such that the packing limit is the same for all three substrate temperatures. Macroscale analysis neglects the reduction of thermal conduction cooling due to heat-carrier boundary scattering and overpredicts the packing limit. The error in the macroscale prediction increases with decreasing temperature due to the increasing importance of boundary scattering at low temperatures. The table shows that to achieve the same packing density at cryogenic temperatures in SOI circuits a lower thermal conductance must be targeted.

## 6.5 Concluding Remarks

The mean time to failure of FET-interconnect contacts and the FET channel mobility are important design parameters for SOI circuits. They are affected by the channel and interconnect temperatures, which are shown here to depend strongly on the dimensions

Table 6-4 Effect of boundary scattering on the FET packing limit

| | FET Packing Limit, $10^6$ devices $cm^{-2}$ | | |
|---|---|---|---|
| Temperature, Conductance | Microscale Analysis | Macroscale Analysis | Macroscale Error |
| $T_0 = 300$ K, $G = 18.5$ μW $K^{-1}$ | 1.42 | 1.52 | 6.6 % |
| $T_0 = 77$ K, $G = 11.4$ μW $K^{-1}$ | 1.42 | 2.06 | 44 % |
| $T_0 = 50$ K, $G = 7.08$ μW $K^{-1}$ | 1.42 | 2.50 | 76 % |

and thermal conductivities of SOI FETs, e.g., $k_d$, $d_d$, $d_o$, and $L_d$. Some of these parameters also affect the electrical performance of the device directly. In order to achieve circuits of optimal performance and reliability, design for electrical performance should be accompanied by *device-level thermal design*, i.e., the choice of dimensions, materials, and processing techniques which enhance heat conduction within a few micrometers of the device. This chapter provides a basis for the thermal design of SOI FETs.

More work is needed to determine the transient temperature fields near the channels of FETs in integrated SOI circuits. While this steady-state analysis provides a good estimate of the FET-interconnect contact temperature when the time-averaged power of a device is used, the channel temperature will experience fluctuations due to periodic heating. To accurately determine the transient channel temperature, a more detailed model for the rate of heat dissipation within the channel is required. Channel-temperature fluctuations in time will render electrical-property measurements performed on SOI devices in the steady state inappropriate for devices in an integrated circuit.

Finite-element heat-conduction analysis packages are expected to become standard elements of computer-aided design tools for the development of integrated circuits. For the design of integrated circuits operating at 77 K, it is recommended to incorporate in these packages the ability to account for size effects on the thermal conductivity. This is imperative for SOI technology, due to the increased thermal resistance between the channel and the substrate.

# 7. CONCLUSIONS AND RECOMMENDATIONS

This work makes progress towards solving the problems posed in Chapter 1, i.e., the lack of knowledge of layer thermal conductivities and the need for techniques which determine temperature fields in small electronic devices. But more work is needed before device-level thermal design can be conducted with the needed precision. This will require a multi-disciplinary research effort, as shown in Fig. 7-1, where research in heat transfer determines *circuit-material thermal properties* and *device-level temperature fields.* This helps researchers in materials science to measure the temperature-field dependence of the behavior of materials, such as electromigration in interconnects. Similarly, researchers in electrical engineering can experimentally relate device characteristics, such as the drain current of a transistor for a given voltage bias, to temperature fields in devices. The knowledge gained from these efforts allows the temperature fields to be used for device-level thermal design.

Fig. 7-1 shows that this research will be important for hybrid superconductor-semiconductor circuits, which combine superconducting Josephson junctions and transmission lines with semiconducting transistors and may soon be able to process information with unprecedented speed (e.g., Ono, 1992). One of the challenges for the thermal design of hybrid circuits is to prevent the semiconducting components, which dissipate energy, from significantly heating the superconducting components, whose critical-current densities diminish with increasing temperature (Flik and Hijikata, 1990). This thermal design requires the knowledge of the thermal conductivities of

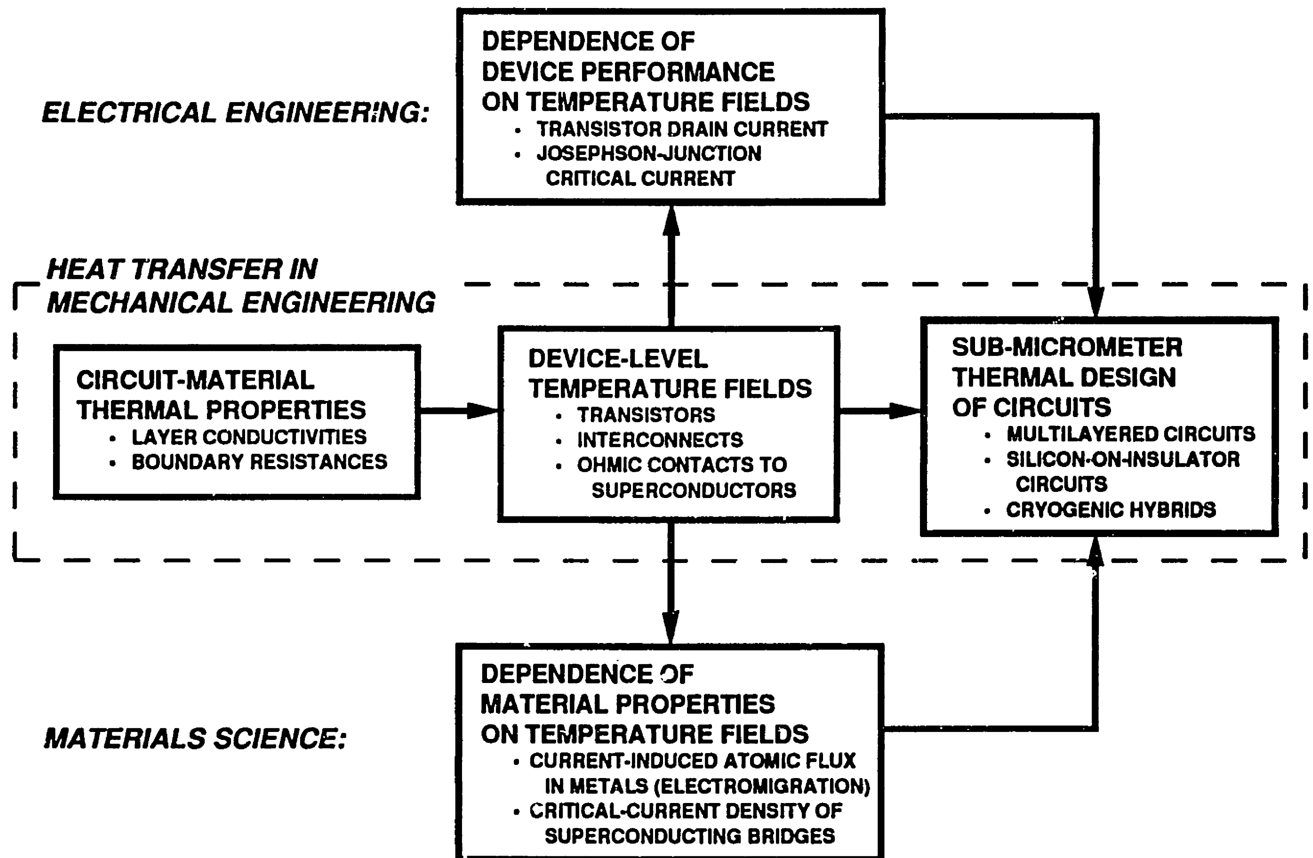


Fig. 7-1 Research goals leading to the sub-micrometer thermal design of electronic circuits.

superconducting layers, which are not known, and are influenced by heat-carrier boundary scattering due to the small dimensions and low operating temperatures of hybrid circuits.

## 7.1 Circuit-Material Thermal Properties

Many of the thermal conductivities of layers and the thermal boundary resistances of interfaces needed to calculate temperature fields in circuits either are not known or need to be measured more accurately. These thermal properties depend on the thickness, temperature, and fabrication processes of the layers. Advances in microfabrication technology should be exploited to improve the accuracy of layer thermal-conductivity measurements. These advances include etching techniques which can yield thin sample membranes suspended above a single-crystal substrate, such as in the test structure of Graebner et al. (1992c) in Fig. 3-3. Microfabrication technology should be used to make test structures which resemble as closely as possible the layers in the electronic structures to be analyzed.

The data should be compared with predictions of microscopic transport analysis. In layers where boundary scattering is important, the mean free paths of heat carriers should be related to quantities characterizing the microstructure, e.g., the grain size and the impurity concentration. Layer thermal conductivities can be predicted considering the fabrication process if parallel research in materials science determines the microstructure resulting from the values of the processing parameters. When the mean free paths of heat carriers are comparable to layer dimensions, the Boltzmann equation should be used to predict the effect of boundary scattering on layer conductivities. For ultra-thin layers, where the heat-carrier *wavelength* can be comparable to the layer thickness, it may prove necessary to solve the Schrödinger equation or to resort to molecular dynamics computations.

## 7.2 Device-Level Temperature Fields

Techniques for local temperature measurements with sub-micrometer resolution are urgently needed, such as that developed in Section 6.3. The need for transient measurements is a major challenge, because transistor switching times can be much less than 1 ns. One promising nondestructive technique employs an atomic-force microscope (AFM) to hold a thermocouple junction at a fixed distance from the surface of circuit components, and may provide the needed spatial resolution (Majumdar et al., 1992). Another possibility is to measure local temperatures using microfabricated thermocouple junctions fabricated within a test circuit, which would yield a resolution governed by the dimension of the junction. Special effort should be given to interconnect temperature measurements, since these are needed to determine the dependence of electromigration on temperature fields.

Previous solutions to the Boltzmann equation, such as Eqs. (5-2) - (5-4), apply to simple geometries, e.g., conduction normal to or along a layer. But the equation must be solved for other practical geometries, such as conduction in the channel of a transistor at low temperatures, where the complex distribution of heating intensity necessitates a two-dimensional treatment. It will be useful to determine the boundary conditions which couple numerical solutions to the Boltzmann equation in regions where heat-carrier-boundary scattering is important, to finite-element techniques for solving the heat-conduction equation in the bounding regions. For ultra-fast processes in circuits, the heat-conduction equation can fail due to the finite velocity of heat carriers, as is discussed in reference to the hyperbolic heat equation in Section 4.3.2. The transient Boltzmann equation needs to be solved for these processes considering the energy dependence of the carrier mean free paths.

## 7.3 Sub-Micrometer Thermal Design of Circuits

This research must provide the information gathered in the left four boxes of Fig. 7-1 in a form that is accessible to the circuit designer, e.g., in a thermal-design package which can be used on a computer. This package must account for the process- and thickness-dependent thermal conductivities of thin layers. Given a circuit geometry and the processing parameters of its layers, the thermal-design package should predict the median time to failure (MTF) of interconnects and the switching time of logic gates considering the temperature fields in the circuit. This will allow the designer to explore sub-micrometer thermal design with unprecedented precision. The potential benefits of this type of thermal design are indicated in Chapter 6, which shows that the channel temperature of a silicon-on-insulator (SOI) field-effect transistor (FET) can be significantly reduced by increasing the device thickness, and that the temperature of the FET-interconnect contact can be reduced by increasing the channel-interconnect separation. These dimensions also influence the electrical behavior and the packing density of devices. With the proper sub-micrometer thermal-design package, competing effects can be balanced to determine the optimal set of dimensions. When the thermal conductivity of a layer depends on the fabrication technique, the thermal design package will indicate which technique is most desirable for a given application. If thermal isolation is required of a chemical-vapor deposited (CVD) silicon-dioxide layer, for example, the recommended processing parameters for the layer, such as the annealing temperature, would be those yielding significant porosity.

# REFERENCES


Adams, A. C., 1988, "Dielectric and Polysilicon Film Deposition," in *VLSI Technology*, S. M. Sze, ed., McGraw-Hill, New York, pp. 233-271.

Anthony, T. R., Banholzer, W. F., Fleischer, J. F., Wei, L., Kuo, P. K., Thomas, R. L., Pryor, R. W., 1990, "Thermal Diffusivity of Isotopically Enriched $^{12}C$ Diamond," *Phys. Rev. B*, Vol. 42, pp. 1104-1111.

Antoniadis, D. A., 1987, "MOS Transistor Fabrication," in *Operation and Modeling of the MOS Transistor*, by Y. P. Tsividis, McGraw-Hill, New York, pp. 433-440.

Aung, W., ed., 1991, *Cooling Techniques for Computers*, Hemisphere, New York.

Bar-Cohen, A., and Kraus, A. D., eds., 1988, *Advances in Thermal Modeling of Electronic Components and Systems*, Hemisphere, New York, Vol. 1.

Bar-Cohen, A., and Kraus, A. D., eds., 1990, *Advances in Thermal Modeling of Electronic Components and Systems*, ASME Press, New York, Vol. 2.

Bartenev, G. M., 1970, *The Structure and Mechanical Properties of Inorganic Glasses*, Wolters-Noordhoof, Groningen, The Netherlands, pp. 35-36, p. 41.

Beck, H., 1975, "Second Sound and Related Thermal Conduction Phenomena," in *Dynamical Properties of Solids*, G. K. Horton and A. A. Maradudin, eds., Vol. 2, pp. 205-279.

Berman, R., 1976, *Thermal Conduction in Solids*, Oxford University Press, Oxford, United Kingdom, Ch. 9, p. 23.

Berman, R., Foster, E. L., and Ziman, J. M., 1956, "The Thermal Conductivity of Dielectric Crystals: The Effect of Isotopes," *Proc. R. Soc. London, Ser. A*, Vol. 237, pp. 344-354.

Black, J. R., 1967, "Mass Transport of Aluminum by Momentum Exchange with Conducting Electrons," *Proc. IEEE Reliability Physics Symposium*, pp. 148-159.

Bohren, C. F., and Huffman, D. R., 1983, *Absorption and Scattering of Light by Small Particles*, Wiley, New York, pp. 130 - 136, 259-265.

Boiko, B. T., Pugachev, A. T., and Bratsychin, V. M., 1973, "Method for the Determination of the Thermophysical Properties of Evaporated Thin Films," *Thin Solid Films*, Vol. 17, pp. 157-161.

Boltzmann, L., 1964, *Lectures on Gas Theory*, University of California Press, Berkeley, translated by S. G. Brush, pp. 110-141.

Bonnet, J. P., 1991, "On the Thermally Activated Structural Relaxation in Glasses," *J. Non-Cryst. Solids*, Vol. 127, pp. 227-231.

Brewster, M. Q., 1992, *Thermal Radiative Transfer and Properties*, Wiley, New York, p. 371.

Brotzen, F. R., Loos, P. J., and Brady, D. P., 1992, "Thermal Conductivity of Thin $SiO_2$ Films," *Thin Solid Films*, Vol. 207, pp. 197-201.

Bunyan, R. J. T., and Uren, M. J., 1991, "Absolute Measurement of Island Temperature in a SOI-MOSFET by Noise Thermometry," *Proc. IEEE International SOI Conference*, M. T. Duffy et al., eds., Vail Valley, Colorado, October 1-3, pp. 26-27.

Cahill, D. G., Fischer, H. E., Klitsner, T., Swartz, E. T., and Pohl, R. O., 1989, "Thermal Conductivity of Thin Films: Measurements and Understanding," *J. Vac. Sci. Technol.*, Vol. A7, pp. 1259-1266.

Cahill, D. G., and Pohl, R. O., 1987, "Thermal Conductivity of Amorphous Solids above the Plateau," *Phys. Rev. B*, Vol. 35, pp. 4067-4073.

Callaway, J., 1959, "Model for Lattice Thermal Conductivity at Low Temperatures," *Phys. Rev.*, Vol. 113, pp. 1046-1051.

Carslaw, H. S., and Jaeger, J. C., 1959, *Conduction of Heat in Solids*, Oxford University Press, New York, p. 263, pp. 214-216.

Celler, G. K., and White, A. E., 1992, "Buried Oxide and Silicide Formation by High-Dose Implantation in Silicon," *MRS Bulletin*, Vol. 17, June, pp. 40-46.

Chen, G., and Tien, C. L., 1992, "Thermal Conductivity of Quantum Well Structures," *AIAA 30th Aerospace Science Meeting*, Reno, NV, January 6-9, Paper No. 92-0707, to appear in *AIAA J. Thermophysics and Heat Transfer*.

Chern, J. G. J., Oldham, W. G., Cheung, N., 1986, "Electromigration in Al/Si Contacts - Induced Open-Circuit Failure," *IEEE Trans. Electron Devices*, Vol. ED-33, pp. 1256-1262.

Claro, F., and Mahan, G. D., 1989, "Transient Heat Transport in Solids," *J. Appl. Phys.*, Vol. 66, pp. 4213-4217.

Colinge, J. P., 1991, *Silicon-on-Insulator Technology: Materials to VLSI*, Kluwer Academic Publishers, Boston, pp. 1-5, 107-108.

Dua, A. K., and Agarwala, R. P., 1972, "Thermal Conductivity of Thin Films of Alkali Metals," *Thin Solid Films*, Vol. 10, pp. 137-139.

Flik, M. I., and Hijikata, K, 1990, "Approximate Thermal Packaging Limit for Hybrid Superconductor-Semiconductor Electronic Circuits," *Heat Transfer 1990*, G. Hetsroni, ed., Hemisphere, New York, Vol. 2, pp. 319-324.

Flik, M. I., and Tien, C. L., 1990, "Size Effect on the Thermal Conductivity of High-$T_c$ Thin-Film Superconductors," *J. Heat Transfer*, Vol. 112, pp. 872-881.

Freeman, J. J., and Anderson, A. C., 1986a, "Normalized Thermal Conductivity of Amorphous Solids," in *Phonon Scattering in Condensed Matter*, A. C. Anderson and J. P. Wolfe, eds., Vol. 5., pp. 32 -34.

Freeman, J. J., and Anderson, A. C., 1986b, "Thermal Conductivity of Amorphous Solids," *Phys. Rev. B*, Vol. 34, pp. 5684-5690.

Fuchs, K., 1938, "The Conductivity of Thin Metallic Films According to the Electron Theory of Metals," *Proc. Cambridge Phil. Soc.*, Vol. 34, pp. 100-108.

Gilroy, K. S., and Phillips, W. A., 1981, "An Asymmetric Double-Well Potential Model for Structural Relaxation Processes in Amorphous Materials," *Philos. Mag.*, Vol. B42, pp. 735-746.

Goldsmid, H. J., Kaila, M. M., and Paul, G. L., 1983, "Thermal Conductivity of Amorphous Silicon," *Phys. Stat. Sol.*, Vol. 76, pp. K31-K33.

Goodson, K.E., and Flik, M.I., 1992, "Electron and Phonon Thermal Conduction in Epitaxial High-$T_c$ Superconducting Films," *J. Heat Transfer*, in press.

Graebner, J. E., Jin, S., Kammlott, G. W., Herb, J. A., and Gardinier, C. F., 1992a, "Unusually High Thermal Conductivity in Diamond Films," *Appl. Phys. Lett.*, Vol. 60, pp. 1576-1578.

Graebner, J. E., Jin, S., Kammlott, G. W., Bacon, B., Seibles, L., Banholzer, W., 1992b, "Anisotropic Thermal Conductivity in Chemical Vapor Deposition Diamond," *J. Appl. Phys.*, Vol. 71, pp. 5353-5356.

Graebner, J. E., Mucha, J. A., Seibles, L., and Kammlott, G. W., 1992c, "The Thermal Conductivity of Chemical-Vapor-Deposited Diamond Films on Silicon," *J. Appl. Phys.*, Vol. 71, pp. 3143-3146.

Guenther, A. H., and McIver, J. K., 1988, "The Role of Thermal Conductivity in the Pulsed Laser Damage Sensitivity of Optical Thin Films," *Thin Solid Films*, Vol. 163, pp. 203-214.

Guyer, R. L., and Koshland, D. E., Jr., 1990, "Diamond: Glittering Prize for Materials Science," *Science*, Vol. 250, pp. 1640-1643.

Gyftopoulos, E. P., and Beretta, G. P., 1991, *Thermodynamics: Foundations and Applications*, Macmillan, New York, Chapter 13.

Hatta, I., 1985, "Thermal Diffusivity Measurement of Thin Films by Means of an AC Calorimetric Method," *Rev. Sci. Instrum.*, Vol. 56, pp. 1643-1646.

Hatta, I., Kato, R., and Maesono, A., 1986, "Development of AC Calorimetric Method for Thermal Diffusivity Measurement. I. Contribution of Thermocouple Attachment in a Thin Sample," *Jpn. J. Appl. Phys.*, Vol. 25, pp. L493-L495.

Hatta, I., Kato, R., and Maesono, A., 1987, "Development of AC Calorimetric Method for Thermal Diffusivity Measurement. II. Sample Dimension Required for the Measurement," *Jpn. J. Appl. Phys.*, Vol. 26, pp. 475-478.

Holland, M. G., 1963, "Analysis of Lattice Thermal Conductivity," *Phys. Rev.*, Vol. 132, pp. 2461-2471.

Holman, J. P., 1984, *Experimental Methods for Engineers*, McGraw-Hill, New York, pp. 50-57.

Hunklinger, S., and Arnold, W., 1976, "Ultrasonic Measurements in Amorphous Solids," in *Physical Acoustics*, W. P. Mason and R. N. Thurston, eds., Vol. 12, pp. 155 - 209.

Joseph, D. D., and Preziosi, L., 1989, "Heat Waves," *Rev. Mod. Phys.*, Vol. 61, pp. 41-73.

Joseph, D. D., and Preziosi, L., 1990, "Addendum to the Paper Heat Waves," *Rev. Mod. Phys.*, Vol. 62, pp. 375-391.

Kaviany, M., 1991, *Principles of Heat Transfer in Porous Media*, Springer-Verlag, New York, pp. 115-151.

Kittel, C., 1949, "Interpretation of the Thermal Conductivity of Glasses," *Phys. Rev.*, Vol. 75, pp. 972-974.

Kittel, C., 1986, *Introduction to Solid State Physics*, Wiley, New York, chs. 4, 5, 6, and 17.

Kittel, C., and Kroemer, H., 1980, *Thermal Physics*, W. H. Freeman and Co., San Francisco, pp. 395-396.

Klemens, P. G., 1951, "The Thermal Conductivity of Dielectric Solids at Low Temperatures," *Proc. R. Soc. London, Ser. A*, Vol. 208, pp. 108-133.

Kumar, S., and Vradis, G. C., 1991, "Thermal Conduction by Electrons Along Thin Films: Effects of Thickness According to Boltzmann Transport Theory," in *Micromechanical Sensors, Actuators, and Systems*, D. Cho et al., eds., ASME DSC-Vol. 32, pp. 89-101.

Lambropoulos, J. C., Jacobs, S. D., Burns, S. J., Shaw-Klein, L., and Hwang, S. S., 1991, "Thermal Conductivity of Thin Films: Measurement and Microstructural Effects," in *Thin Film Heat Transfer - Properties and Processing*, ASME HTD-Vol. 184, M. K. Alam et al., eds., pp. 21 -32.

Lambropoulos, J. C., Jolly, M. R., Amsden, C. A., Gilman, S. E., Sinicropi, M. J., Diakomihalis, D., and Jacobs, S. D., 1989, "Thermal Conductivity of Dielectric Thin Films," *J. Appl. Phys.*, Vol. 66, pp. 4230-4242.

Lee, Y. H., Biswas, R., Soukoulis, C. M., Wang, C. Z., Chan, C. T., and Ho, K. M., 1991, "Molecular-Dynamics Simulation of Thermal Conductivity in Amorphous Silicon," *Phys. Rev. B*, Vol. 43, pp. 6573-6580.

Lifka, H., and Woerlee, P. H., 1990, "Thin Simox SOI Material for Half-Micron CMOS," *Proc. European Solid State Device Research Conference*, W. Eccleston and P. J. Rosser, eds., Nottingham, U.K., September 10-13, pp. 453-456.

Little, W. A., 1959, "The Transport of Heat between Dissimilar Solids at Low Temperatures," *Can. J. Phys.*, Vol. 37, pp. 334-349.

Majumdar, A., 1991, "Microscale Heat Conduction in Dielectric Thin Films," *Thin-Film Heat Transfer - Properties and Processing*, M.K. Alam et al., eds., ASME HTD-Vol. 184, pp. 33-42.

Majumdar, A., Carrejo, J. P., and Lai, J., 1992, "Thermal Imaging Using the Atomic Force Microscope," Submitted to *Appl. Phys. Lett.*

Marcus, R. B., and Sheng, T. T., 1983, *Transmission Electron Microscopy of Silicon VLSI Circuits and Structures*, Wiley, New York, pp. 80-82.

Mastrangelo, C. H., and Muller, R. S., 1988, "Thermal Diffusivity of Heavily Doped Low Pressure Chemical Vapor Deposited Polycrystalline Silicon Films," *Sensors and Materials*, Vol. 3, pp. 133-141.

Matsumoto, D. S., Reynolds, C. L., and Anderson, A. C., 1977, "Thermal Boundary Resistance at Metal-Epoxy Interfaces," *Phys. Rev. B*, Vol. 16, pp. 3303-3307.

Mautry, P. G., and Trager, J., 1990, "Self-Heating and Temperature Measurement in Sub-µm-MOSFETs," *Proc. IEEE International Conferencc on Microelectronic Test Structures*, Vol. 3, pp. 221-226.

McDaid, L. J., Hall, S., Mellor, P. H., Eccleston, W., Alderman, J. C., 1989, "Physical Origin of the Negative Differential Resistance in SOI Transistors," *Electronics Lett.*, Vol. 25, pp. 827-828.

McSkimin, H. J., 1953, "Measurement of Elastic Constants at Low Temperatures by Means of Ultrasonic Waves - Data for Silicon and Germanium Single Crystals, and for Fused Silica," *J. Appl. Phys.*, Vol. 24, pp. 988-997.

McSkimin, H. J., and Andreatch, P. J., 1972, "Elastic Moduli of Diamond as a Function of Pressure and Temperature," *J. Appl. Phys.*, Vol. 43, pp. 2944-2948.

Morelli, D. T., Beetz, C. P., and Perry, T. A., 1988, "Thermal Conductivity of Synthetic Diamond Films," *J. Appl. Phys.*, Vol. 64, pp. 3063-3066.

Muller, R. S., and Kamins, T. I., 1986, *Device Electronics for Integrated Circuits*, Wiley, New York, p. 31.

Murarka, S. P., 1988, "Metallization," *in VLSI Technology*, S. M. Sze, ed., McGraw-Hill, New York, pp. 375-421.

Nagasima, N., 1972, "Structure Analysis of Silicon Dioxide Films Formed by Oxidation of Silane," *J. Appl. Phys.*, Vol. 43, pp. 3378-3386.

Nath, P., and Chopra, K. L., 1973, "Experimental Determination of the Thermal Conductivity of Thin Films," *Thin Solid Films*, Vol. 18, pp. 29-37.

Ono, R. H., 1992, "Thin-Film Processing of Complex Multilayer Structures of High-Temperature Superconductors," *Materials Research Society Bulletin*, Vol. 17, August, pp. 34-38.

Peierls, R. E., 1929, "Zur kinetischen Theorie der Wärmeleitung in Kristallen," *Ann. Phys.*, Vol. 3, pp. 1055- 1101.

Peierls, R. E., 1955, *Quantum Theory of Solids*, Oxford University Press, New York, chs. 1 and 2.

Pompe, G., and Schmidt, K., 1975, "Vapour-Deposited Lead Films and Their Transport Characteristics at Low Temperatures," *Phys. Stat. Sol.*, Vol. A31, pp. 37-46.

Powell, R. W., 1957, "Experiments Using a Simple Thermal Comparator for Measurement of Thermal Conductivity, Surface Roughness and Thickness of Foils or of Surface Deposits," *J. Sci. Instrum.*, Vol. 34, pp. 485-492.

Powell, R. L., Rogers, W. M., Coffin, D. O., 1957, "An Apparatus for Measurement of Thermal Conductivity of Solids at Low Temperatures," *J. Res. N. Bur. Stand.*, Vol. 59, pp. 349-355.

Rohsenow, W. M., and Choi, H. Y., 1961, *Heat, Mass, and Momentum Transfer*, Prentice-Hall, Englewood Cliffs, New Jersey, p. 155.

Rosenberg, H. M., 1954, "The Thermal Conductivity of Germanium and Silicon at Low Temperatures," *Proc. Phys. Soc., London, Sect. A*, Vol. 67, pp. 837-840.

Rowe, D. M., and Bhandari, C., M., 1986, "Preparation and Thermal Conductivity of Doped Semiconductors," *Progress in Crystal Growth and Characterization*, Vol. 13, pp. 233-289.

Savvides, N., and Goldsmid, H. J., 1972, "Boundary Scattering of Phonons in Silicon Crystals at Room Temperature," *Phys. Lett.*, Vol. 41A, pp. 193-194.

Schafft, H. A., Suehle, J. S., and Mirel, P. G. A., 1989, "Thermal Conductivity Measurements of Thin-Film Silicon Dioxide," *Proc. IEEE International Conference on Microelectronic Test Structures*, A. J. Walton et al., eds., Edinburgh, Scotland, March 13-14, Vol. 2, pp. 121-124.

Schroder, D. K., 1987, *Advanced MOS Devices*, Addison-Wesley, Reading, Massachusetts, pp. 204-206.

Schwarzenberger, A. P., Ross, C. A., Evetts, C. A., and Greer, A. L., 1988, "Electromigration in the Presence of a Temperature Gradient: Experimental Study and Modelling," *J. Electronic Materials*, Vol. 17, pp. 473-478.

Shibata, H., Ohta, H., Waseda, Y., 1991, "New Laser Flash Method for Measuring Thermal Diffusivity of Isotropic and Anisotropic Thin Films," *JIM Mat. Trans.*, Vol. 32, pp. 837-844.

Siegel, R., and Howell, J. R., 1981, *Thermal Radiation Heat Transfer*, Hemisphere, New York, pp. 111-117, pp. 476-481.

Slack, G. A., 1964, "Thermal Conductivity of Pure and Impure Silicon, Silicon Carbide, and Diamond," *J. Appl. Phys.*, Vol. 35, pp. 3460-3466.

Smolinsky, G., and Wendling, T. P. H. F., 1985, "Measurements of Temperature Dependent Stress of Silicon Dioxide Films Prepared by a Variety of CVD Methods," *J. Electrochemical Society*, Vol. 132, pp. 950-954.

Sondheimer, E. H., 1952, "The Mean Free Path of Electrons in Metals," *Adv. Phys.*, Vol. 1, pp. 1-42.

Stephens, R. B., 1973, "Low-Temperature Specific Heat and Thermal Conductivity of Noncrystalline Solids," *Phys. Rev. B*, Vol. 8, pp. 2896-2905.

Sugawara, A., 1969, "Precise Determination of Thermal Conductivity of High Purity Fused Quartz from 0° to 650°C," *Physica*, Vol. 41, pp. 515-520.

Swartz, E. T., and Pohl, R. O., 1987, "Thermal Resistance at Interfaces," *Appl. Phys. Lett.*, Vol. 51, pp. 2200-2202.

Swartz, E. T., and Pohl, R. O., 1989, "Thermal Boundary Resistance," *Rev. Mod. Phys.*, Vol. 61, pp. 605-668.

Sze, S. M., 1988, "Introduction: Growth of the Industry," in *VLSI Technology*, S. M. Sze, ed., McGraw-Hill, New York, pp. 1-8.

Tai, Y. C., Mastrangelo, C. H., and Muller, R. S., 1988, "Thermal Conductivity of Heavily Doped Low-Pressure Chemical Vapor Deposited Polycrystalline Silicon Films," *J. Appl. Phys.*, Vol. 63, pp. 1442-1447.

Tavernier, J., 1962, "Sur l'Equation de Conduction de la Chaleur," *Comptes Rendus Acad. Sci.*, Vol. 254, pp. 69-71.

Tien, C. L., 1988, "Thermal Radiation in Packed and Fluidized Beds," *J. Heat Transfer*, Vol. 110, pp. 1230-1242.

Tien, C. L., Armaly, B. F., and Jagannathan, P. S., 1969, "Thermal Conductivity of Thin Metallic Films and Wires at Cryogenic Temperatures," *Proc. Eighth Conference on Thermal Conductivity*, C. Y. Ho and R. E. Taylor, eds., Plenum Press, New York, pp. 13-19.

Tien, C. L., and Chen, G., 1992, "Challenges in Microscale Radiative and Conductive Heat Transfer," presented at the ASME Winter Annual Meeting, Anaheim, CA, November 8-13, in *Fundamental Issues in Small Scale Heat Transfer*, Y. Bayazitoglu and G. P. Peterson, eds., ASME HTD-Vol. 227, pp. 1-12.

Tien, C. L., and Lienhard, J. H., 1979, *Statistical Thermodynamics*, Hemisphere, New York, pp. 334-346.

Touloukian, Y. S., and Buyco, E. H., 1970a, "Specific Heat: Metallic Elements and Alloys," from *Thermophysical Properties of Matter*, Vol. 4, IFI/Plenum, New York, pp. 204-206.

Touloukian, Y. S., and Buyco, E. H., 1970b, "Specific Heat: Nonmetallic Solids," from *Thermophysical Properties of Matter*, Vol. 5, IFI/Plenum, New York, pp. 202-205.

Touloukian, Y. S., Powell, R. W., Ho, C. Y., and Klemens, P. G., 1970a, "Thermal Conductivity: Metallic Elements and Alloys," from *Thermophysical Properties of Matter*, Vol. 1, New York: IFI/Plenum, pp. 9, 326, 330, and 335.

Touloukian, Y. S., Powell, R. W., Ho, C. Y., and Klemens, P. G., 1970b, "Thermal Conductivity: Nonmetallic Solids," from *Thermophysical Properties of Matter*, Vol. 2, New York: IFI/Plenum, p. 193.

Tsien, H. S., 1946, "Superaerodynamics," *J. Aero. Sc.*, Vol. 13, pp. 653-664.

Tsividis, Y. P., 1987, *Operation and Modeling of the MOS Transistor*, McGraw-Hill, New York, pp. 102-167, pp. 148-150, pp. 168-216.

Tsutsumi, N., and Kiyotsukuri, T., 1988, "Measurement of Thermal Diffusivity for Polymer Film by Flash Radiometry," *Appl. Phys. Lett.*, Vol. 52, pp. 442-444.

Udell, K. S., Pisano, A. P., Howe, R. T., Muller, R. S., and White, R. M., 1990, "Microsensors for Heat Transfer and Fluid Flow Measurements," *Experimental Thermal and Fluid Science*, Vol. 3, pp. 52-59.

Vacher, R., Pelous, J., Plicque, F., and Zarembowitch, A., 1981, "Ultrasonic and Brillouin Scattering Study of the Elastic Properties of Vitreous Silica Between 10 and 300 K," *J. Non-Cryst. Solids*, Vol. 45, pp. 397-410.

Vedavarz, A., Kumar, S., and Moallemi, M. K., 1991, "Significance of Non-Fourier Heat Waves in Microscale Conduction," *Micromechanical Sensors, Actuators, and Systems*, D. Cho et al., eds., ASME DSC-VOL. 32, pp. 109-122.

Verghese, S., Richards, P. L., Char, K., Fork, D. K., and Geballe, T. H., 1992, "Feasibility of Imaging Arrays Using High-$T_c$ Superconducting Bolometers," *J. Appl. Phys.*, Vol. 71, pp. 2491-2496.

Visser, E. P., Versteegen, E. H., Enckevort, J. P., 1992, "Measurement of Thermal Diffusion in Thin Films Using a Modulated Laser Technique: Application to Chemical-Vapor-Deposited Diamond Films," *J. Appl. Phys.*, Vol. 71, pp. 3238-3248.

Völklein, F., and Kessler, E., 1984, "A Method for the Measurement of Thermal Conductivity, Thermal Diffusivity, and Other Transport Coefficients of Thin Films," *Phys. Stat. Sol.*, Vol. A81, pp. 585-596.

Walton, D., 1974, "Random-Network Model, Density Fluctuation, and Thermal Conductivity of Glasses," *Solid State Comm.*, Vol. 14, pp. 335-339.

White, G. K., and Tainsh, R. J., 1960, "Lorenz Number for High-Purity Copper," *Phys. Rev.*, Vol. 119, pp. 1869-1871.

White, G. K., and Woods, S. B., 1954, "The Lattice Conductivity of Dilute Copper Alloys at Low Temperatures," *Philos. Mag.*, Vol. 45, pp. 1343-1345.

Wilson, A. H., 1953, *The Theory of Metals*, Cambridge University Press, New York, pp. 286-296.

Woerlee, P. H., van Ommen, A. H., Lifka, H., Juffermans, C. A. H., Plaja, L., and Klaassen, F. M., 1989, "Half-Micron CMOS on Ultra-Thin Silicon on Insulator," *Proc. IEEE International Electron Devices Meeting*, C. Sodini et al., eds., Washington, D.C., December 3-6, pp. 821-824.

Yang, E. S., 1988, *Microelectronic Devices*, McGraw-Hill, New York, pp. 287-290.

Zachariasen, W. H., 1932, "The Atomic Arrangement in Glass," *J. American Chemical Society*, Vol. 54, pp. 3841-3851.

Zaitlin, M. P., and Anderson, A. C., 1975, "Phonon Thermal Transport in Noncrystalline Materials," *Phys. Rev. B*, Vol. 12, pp. 4475-4486.

Zaitlin, M. P., Scherr, L. M., and Anderson, A. C., 1975, "Boundary Scattering of Phonons in Noncrystalline Materials," *Phys. Rev. B*, Vol. 12, pp. 4487-4492.

Zeller, R. C., and Pohl, R. O., 1971, "Thermal Conductivity and Specific Heat of Noncrystalline Solids," *Phys. Rev. B*, Vol. 4, pp. 2029-2041.

Ziman, J. M., 1960, *Electrons and Phonons*, Oxford University Press, Oxford, United Kingdom, pp. 221-223, 259, 307, 357-370, and 456-460.

Ziman, J. M., 1979, *Models of Disorder*, Oxford University Press, Oxford, United Kingdom, pp. 64-77.